Simulating Exciton Dynamics in Organic Semiconductors

by

Chee Kong Lee

Submitted to the Department of Chemistry
in partial fulfillment of the requirements for the degree of

Doctor of Philosophy in Chemistry

at the

MASSACHUSETTS INSTITUTE OF TECHNOLOGY

February 2019

© Massachusetts Institute of Technology 2019. All rights reserved.

Signature redacted

Author . . . .
Department of Chemistry
October 25, 2018

Signature redacted

Certified by . . . .
Adam P. Willard
Associate Professor of Chemistry
Thesis Supervisor

Signature redacted

Accepted by . . . .
Robert W. Field
Haslam and Dewey Professor of Chemistry
Chairman, Departmental Committee on Graduate Students

MASSACHUSETTS INSTITUTE OF TECHNOLOGY
MAR 21 2019
LIBRARIES
ARCHIVES

This doctoral thesis has been examined by a Committee of the
Department of Chemistry as follows:

Signature redacted

Professor Keith A. Nelson ....
Chairman, Thesis Committee
Haslam and Dewey Professor of Chemistry

Signature redacted

Professor Adam P. Willard..................
Thesis Supervisor
Associate Professor of Chemistry

Signature redacted

Professor Marc A. Baldo........ ...
Member, Thesis Committee
Professor of Electrical Engineering and Computer Science

Simulating Exciton Dynamics in Organic Semiconductors

by

Chee Kong Lee

Submitted to the Department of Chemistry
on October 25, 2018, in partial fulfillment of the
requirements for the degree of
Doctor of Philosophy in Chemistry

Abstract

Organic semiconductors are carbon-based semiconductors with number of unique benefits over traditional semiconductors such as low production costs, versatile synthesis processes, and high portability. Unlike traditional crystalline semiconductors that exhibit high level of homogeneity, organic semiconductors are spatially and temporally heterogeneous due to the weak van der Waals intermolecular forces. In this thesis we utilize computational and theoretical methods to investigate how this heterogeneity affects the electronic properties in organic semiconductors. In particular, we focus on two microscopic processes fundamental to the performance of organic semiconductors: the transport of Frenkel exciton and dissociation of charge-transfer (CT) exciton.

Frenkel excitons are tightly bound electron-hole pairs created upon photo-excitation of molecules and they carry the excess energy imparted by photons. We employ theoretical approach that combines molecular dynamics and semi-empirical electronic structure calculations to reveal the effects of molecular disorder on Frenkel exciton transport in oligothiophene-based molecular semiconductors. Using this approach, we find that the magnitude and details of molecular disorder (i.e. spatial and temporal correlations) could have huge impact on exciton transport in this class of materials.

CT excitons are electron-hole pairs partially separated across the donor-acceptor interface. To generate free charges, the oppositely charged electron and hole must overcome an electrostatic binding energy before they undergo ground state recombination. We explore the CT exciton dissociate mechanism and magnetic field effects through a model of quantum spin dynamics combined with a stochastic coarse-grained model of charge transport. We demonstrate that simulations carried out on our model are capable of reproducing experimental results as well as generating theoretical predictions related to the efficiency of organic electronic materials. Next, we consider the effect of disorder in electronic energy levels on dissociation yield and demonstrate that it is maximized with a finite amount of disorder as a result of non-equilibrium effect.

Thesis Supervisor: Adam P. Willard
Title: Associate Professor of Chemistry

Acknowledgments

I would like thank my advisor Adam P. Willard for his guidance and mentorship. I am fortunate to have an advisor who respects my career goal and understands work-life balance. I also would like thank my thesis committee members Marc Baldo and Keith Nelson for their valuable inputs.

I thank Brandt Pein, Tristan JiaoJian Shi, Parag Deotare, Wendi Chang, Eric Hontz and Dan Congreve for successfully collaborations. Many of the works here are inspired by their great experiments. I also enjoy the fruitful theory-theory collaborations with Chern Chuang and Jeremy Moix.

I thank my group members Sucheol Shin, Liza Lee, Eric Alt, Thomas Avila, John Kattirtzi, Liang Shi, Paul Teichen, Amr Dodin, Kaitlyn Dwelle, Kyaw Myint and Yizhi Shen, for creating a friendly and welcoming group environment. In particular, I thank Liang for being a great friend, colleague and collaborator. He has the gift of explaining chemistry concepts to a physicist, the stimulating daily discussions with him had been a highlight of my PhD journey.

My higher education would not be possible without the sacrifice and hard work of my mum, this thesis is dedicated to her.

Finally, I thank my wife Pui San Ng for her love and support, I look forward to start a new chapter in life with her.

Contents

1 Introduction **21**

1.1 Organic Semiconductors 21

1.2 Organic Photovoltaics 22

1.3 Organization of Thesis 24

2 Effects of Disorder on Frenkel Exciton Dynamics **27**

2.1 Introduction 27

2.2 Theory 29

2.2.1 Frenkel Exciton Model 29

2.2.2 Modelling of Sexithiophene Films 30

2.2.3 Molecular Dynamics Simulation 32

2.3 Results and Discussions 33

2.3.1 Mean Squared Displacement 37

2.3.2 Inverse Participation Ratio 40

2.4 Conclusions 42

3 Coarse-Grained Modeling of Frenkel Exciton Dynamics **45**

3.1 Introduction 45

3.2 Theory 46

3.3 Results and Discussions 50

3.4 Temperature Dependence 54

3.5 Conclusions 56

4 A Model of Charge Transfer Exciton: Diffusion, Spin Dynamics and Magnetic Field Effects 59
4.1 Introduction 59
4.2 Model 62
  4.2.1 Open Quantum System Approach to Spin Dynamics 65
  4.2.2 Parametrization of the Model 66
4.3 Results and Discussions 68
  4.3.1 Comparison with Experiments 68
  4.3.2 Singlet-Triplet Population Transfer Analysis 71
  4.3.3 Effect of Exchange Coupling 75
4.4 Conclusions 76

5 The Non-equilibrium Effect of Interfacial Charge Transfer Exciton Dissociation 77
5.1 Introduction 77
5.2 A Coarse-Grained Model of Charge-Transfer Exciton Dynamics . . . 80
5.3 Dependence of Dissociation Yield on Disorder 84
5.4 A Sample Kinetic Monte Carlo Trajectory 86
5.5 The Effect of Disorder on the Thermodynamics of Exciton Dissociation 86
5.6 Nonequilibrium Dissociation Dynamics 90
5.7 A Kinetic Model for Nonequilibrium CT State Dissociation 94
5.8 Implications for modern organic electronics 99

6 Conclusions 103

List of Figures

1-1 A schematic illustration of organic photovoltaics with different architectures. (a) Bilayer OPVs contains two types of semiconducting materials: electron donor and electron acceptor. (b) Bulk heterojunctions have an absorption layer consisting of a nanoscale blend of donor and acceptor materials. The domain sizes of this blend are on the order of nanometers, allowing for excitons with short lifetimes to reach an interface and dissociate due to the large donor-acceptor interfacial area. Image reproduced from Ref. [4]. 22

1-2 Photocurrent generation processes in OPVs. Photon absorption by a molecule in the donor layer promotes an electron to an excited state, resulting in a localized and tightly bound electron-hole pair (a so-called Frenkel exciton). Frenkel exciton migrates to the interface between the (electron) donor and acceptor molecules, resulting in the transient formation of a charge-transfer state whereby the electron and hole resides on different molecules. The dissociation of the charge-transfer exciton is then followed by charge transport where electrons and holes can hop between adjacent electron acceptor and donor molecules respectively. 23

2-1 Configurations of simulated T6 system in this chapter. (a) An isolated T6 monomer. (b) A T6 monolayer film. (c) A disordered bulk phase of T6 molecules. 30

2-2 Comparison between the calculated properties from the model in this chapter and the more accurate TDDFT: (a) excitation energy in eV for the lowest singlet exciton (the red line indicates the linear fitting after adjusting for systematic error); (b) three Cartesian components of the transition dipole in Debye associated with the lowest singlet exciton; (c) excitonic coupling between the two localized singlet exciton states. Two methods of extracting excitonic couplings from TDDFT calculations are adopted: an energy-gap-based method [32](black circles), and the method described in Ref. [33] (red squares). All the dashed blue lines in this figure indicate the diagonals. Figure reproduced from Ref. [21] 31

2-3 (a) A snapshot of molecular configuration of the T6 monolayer film studied in this chapter. (b) The corresponding individual molecule centre-of-mass positions in the T6 monolayer film. The site energies (in eV) of the molecules are represented by the color gradient. (c) Distributions of site energies sampled from 100 MD configurations for T6 monolayer (blue) and disordered film (red). d) The spatial correlation (normalized) of the site energies as a function of center-of-mass distance for T6 monolayer (blue) and disordered film (red). 34

2-4 a) The average time correlation functions (normalized) of the site energies in T6 monolayer (solid blue) and disordered films (dashed red). b) The average time correlation function (normalized) of the excitonic couplings in T6 monolayer (solid blue) and disordered films (dashed red). 36

2-5 Average mean-squared-displacement (MSD) of an initially localized exciton in (a) monolayer and (b) disorder films under different conditions: full molecular calculations generated at the level of QM/MM (solid blue), calculations with no time-dependent fluctuations (solid red), calculations with no spatial correlation in the static disorder (solid orange) and calculations with no time correlation in the time-dependent fluctuations (dashed magenta). 37

2-6 Distributions of MSDs at t = 100fs from 100 initial configurations in (a) monolayer and (b) disorder films under two different scenarios: full molecular calculations generated at the level of QM/MM (blue), calculations with no time correlation in the time-dependent fluctuations (red). 38

2-7 Average mean-squared-displacement (MSD) of an initially localized exciton in disordered film generated from full molecular calculations (blue lines) and calculations with no spacial correlations in disorder (red lines). The magnitude of static disorder is artificially increased by (a) no increase, (b) 100% and (c) 200% to demonstrate that the effect of spatial correlation is dependent on the magnitude of static disorder. . 39

2-8 Average IPR of an initially localized exciton in (a) monolayer and (b) disorder films under different scenarios: full molecular calculations generated at the level of QM/MM (solid blue), calculations with no time-dependent fluctuations (solid red), calculations with no spatial correlation in the static disorder (solid orange) and calculations with no time correlation in the time-dependent fluctuations (dashed magenta). . . 40

2-9 Distributions of IPRs at t = 100fs from 100 initial configurations in (a) monolayer and (b) disorder films under two different conditions: full molecular calculations generated at the level of QM/MM (blue) and calculations with no time correlation in the time-dependent fluctuations (red). 41

2-10 Average IPR of an initially localized exciton in disordered film generated from full molecular calculations, but with the magnitude of static disorder is artificially increased by (a) no increase, (b) 2 times and (c) 3 times to demonstrate that the effect of spatial correlation is dependent on the magnitude of static disorder. 42

3-1 (a) (i) Molecular configuration of a monolayer of T6 molecules studied in this chpater. (ii) A snapshot of the individual molecule centre-of-mass positions in the T6 monolayer film. The site energies of the molecules are represented by the color gradient (in eV). (iii) Coarse-grained lattice model that intends to mimic the exciton dynamics of monolayer T6 film. (b) Distributions of exciton site energies sampled from 100 MD configurations of the T6 monolayer film. (c) The average excitonic coupling as a function of center-of-mass separation (solid line). The scaling relation of dipole-diploe coupling (dahsed line) is included for comparison. 47

3-2 Comparisons between atomistic model (solid lines) and coarse-grained lattice model (dashed lines). (a) Average mean-squared-displacement (MSD) of an initially localized exciton. (b) Average time-dependent inverse participation ration (IPR) of an initially localized exciton. (Bottom) Distributions of individual trajectory (c) MSD and (d) IPR at $t = 100$fs sampled from 100 initial configurations. 50

3-3 (a) Average mean-squared-displacement (MSD) and (b) inverse participation ration (IPR) of an initially localized exciton from a 50 by 50 coarse-grained lattice model (dashed lines). The corresponding MSD and IPR from atomistic simulation of 150 molecules (solid lines) are included to demonstrate the significant finite size effect. 52

3-4 Single realizations of random exciton energy landscape in a 50 by 50 lattice at increasing correlation lengths, r_c (in unit of lattice constant). 53

3-5 Simulation results from a 50 by 50 coarse-grained model. (a) Exciton diffusion constant as a function of r_c at different values of disorder. (b) Exciton diffusion constant as a function of temperature at $r_c = 4.8$Å(one lattice constant) and $\sigma = 260 meV$. 55

4-1 (a) The relative energy of the three, otherwise degenerate, triplet levels are split (Zeeman splitting) by a magnetic field. Consequently, as indicated with red arrows, the timescale for spin mixing dynamics can be varied with an external magnetic field. (b) A schematic depiction of the model system in which donor and acceptor molecules (represented as blue- and red-shaded circles respectively) reside on opposite halves of an ordered lattice. The electron (-) and hole (+) occupy individual molecules whose orbital energies vary as indicated by shading. The relative energy of singlet and triplet states is determined by the exchange splitting, which decays rapidly with electron-hole separation. When the electron and hole occupy neighboring sites (top) this exchange splitting is typically larger than thermal energies. When the electron and hole are separated by one or more molecules (bottom) the exchange splitting is negligible resulting in degenerate singlet and triplet energy levels. 61

4-2 Energy diagram and chemical structures of the donor-acceptor material system. The energy levels and the HOMO and LUMO are in eV and are referenced to the vacuum. The energies in eV of the lowest singlet (S_1) and triplet (T_1) excitons of m-MTDATA and 3TPYMB are also indicated. Figure reproduced from Ref. [83] 67

4-3 (a) The simulated (blue) and experimental (red) transient decay of photoluminescence (normalized). (b) The centroid of the experimental data (red) is compared to the spectral shift predicted by the kinetic Monte Carlo simulation (blue). The transient redshift of the CT exciton emission wavelength indicates the CT excitons travel to lower energy sides. (c) The simulated mean squared displacement of CT excitons (blue). The red circles show the experimental values of the standard deviation of spatial broadening Gaussian function of PL. The error bars indicate the standard error between four independent diffusing imaging measurements [83]. (d) The magnetic field dependence of photoluminescence (PL) and photocurrent as determined experimentally (solid lines) and simulated with our model (unfilled circles). The quantity plotted against the y-axis is the percentage change, measured relative to the case where $B = 0$. Filled circles correspond to simulated results in the absence of system-bath coupling for spin dynamics. . . 71

4-4 (a) The time-dependence of the singlet population for two typical trajectories, selected to exhibit similar spatial dynamics, carried out under different values of $B = |\vec{B}^{\mathrm{app}}|$. The inset illustrates the hopping behavior of these trajectories, which each ends abruptly with a radiative recombination event. (b) The distribution of the values of singlet population, ρ_{S}, at the recombination time for trajectories generated at different values of applied magnetic field. The red- and green-dashed vertical lines represent the equilibrium values for the bound ($\langle \rho_{\mathrm{S}} \rangle = 0.05$) and unbound ($\langle \rho_{\mathrm{S}} \rangle = 0.25$) CT states respectively. The blue-dashed line represents the value of ρ_{S} for the bound CT state in two-state quasi-equilibrium. 73

4-5 The dependence of photovoltaic IQE on the magnitude of the interfacial exchange splitting as predicted from simulations carried out on our model system. 75

5-1 (a) A schematic of our model for simulating the dynamics of interfacial CT excitons. The color shadings of the blue and red circles represent the varying HOMO energies of donor molecules and LUMO energies of acceptor molecules, respectively. The circles with h^+ and e^- are the hole and electron in the CT exciton, respectively. A representative trajectory is shown as grey arrows, where the electron and hole break apart gradually from the bound CT state (B), to the partially dissociated intermediate state (PDI), and finally to the fully dissociated state (CS). The definitions of the B, PDI, and CS states are given in the main text. (b) The dependence of the CT exciton dissociation yield, f, on the energetic disorder, σ. 81

5-2 (a) A schematic of a representative trajectory from KMC simulations. Red and blues circles are the donor and acceptor molecules on the square lattice, respectively. The color gradient represents the distributions of the HOMO energy of the donors and the LUMO energy of the acceptors, as illustrated in the color scale. The labels (a-d) indicate some instants in the trajectory. (b) The time evolution of the CT exciton energy (top, magenta line) and the electron-hole separation (bottom, dark green line). The labels correspond to the same instants in panel (a). 85

5-3 The internal energy (top), entropy (middle), and Helmholtz free energy (bottom) profiles as functions of electron-hole separation, d, as evaluated using Eq. (5.2) - (5.6). All the thermodynamic quantities are plotted in units of the thermal energy, $k_{\mathrm{B}}T = 1/\beta$. Four different values of energetic disorder σ are considered: $\sigma = 0$ (black), 30 meV (red), 60 meV (blue), and 120 meV (magenta). 88

5-4 The probability distribution of the average value of the vertical energy gap relative to that computed within a perfectly ordered system, $\Delta\bar{E}^{(\mathrm{vert})}$, evaluated from Eq. (5.8) and (5.9): (a) the distributions for $d = 150$ at $\sigma = 30$ meV, 60 meV, and 120 meV; (b) the distributions for three different values of d at fixed $\sigma = 60$ meV. 90

5-5 (a) A plot of the mean squared electron-hole separation, $\bar{d^2}$, as a function of time expressed in units of the intrinsic hopping rate, ν for trajectories under differing levels of energetic disorder. (b) A plot of the average exciton vertical energetic disorder, denoted as $\langle\Delta E^{(\mathrm{vert})}\rangle_{\mathrm{CS}}$ for charge-separated trajectories under differing levels of energetic disorder. 91

5-6 (a)-(c): the 2D Helmholtz free energy profiles as a function of electron-hole separation, d in , and relative vertical energy gap, $\Delta E^{(\mathrm{vert})}$ in eV defined by Eq. (5.8) for $\sigma = 30$ meV (panel (a)), 60 meV (panel (b)), and 120 meV (panel (c)); The contour scale is in the unit of k_BT, the magenta crosses and the white dots are from selected KMC trajectories with random initial conditions (see the main text for details). (d) The equilibrium internal energy profiles (lines) and its nonequilibrium analogs (circles), defined by Eq. (5.10), as functions of d, for varying amounts of energetic disorder. 94

5-7 Average residence time of the electron and hole in the bound (black line) or partially dissociated (red line) states plotted as a function of σ. Residence times are expressed in units of the intrinsic charge hopping time, $1/\nu$. The bound state (black line) is also shown in the inset for a better view. 96

5-8 (a) The representative rates for the transitions in the kinetic model in Eq. 5.11, as a function of σ, computed from Eq. 5.12. The three solid lines are for the transition rates assuming that the initial states are fully thermalized ($B = 1$), and the black dashed line is for k_{12} assuming that the bound CT states are not thermalized ($B = 0$); (b) The dissociate yield, f, as a function of σ, computed from Eq. 5.16 with the k_{12} rates using varying values of B, a measure of the thermalization level of the bound CT states. 100

Chapter 1

Introduction

1.1 Organic Semiconductors

Organic semiconductors are a class of materials whose constituents are mostly made up of carbon and hydrogen atoms with, at times, some hetero-atoms such as sulfur, oxygen and nitrogen. Additionally, they exhibit properties typically associated with semiconducting materials, i.e. they absorb and emit light in the visible spectral range, and are sufficiently conductive for the operations of typical semiconductors such as light-emitting devices, photovoltaics and field-effect-transistors. [1–3]

Organic semiconductors combines the electronic advantages of traditional semiconductors with the chemical and mechanical benefits of organic compounds. Their optical activity and electronic conductivity are united with a material structure that can easily be modified by chemical synthesis to achieve desired emission/absorption wavelength, to render it soluble, or to allow for mechanically robust, lightweight, and flexible thin films. These properties imply that organic electronics are suitable for many traditional semiconductor applications such as displays, lighting panels, or solar cells, and can be produced with a variety of scalable solution-processing techniques or vacuum deposition methods. For example, organic light-emitting diode (OLED)-based displays are already employed by major smartphone makers, including Samsung and Apple. OLED screens are thinner, produce better color contrast and consumes less energy than traditional LEDs/LCDs, making OLED a technology of choice for many display applications.

1.2 Organic Photovoltaics

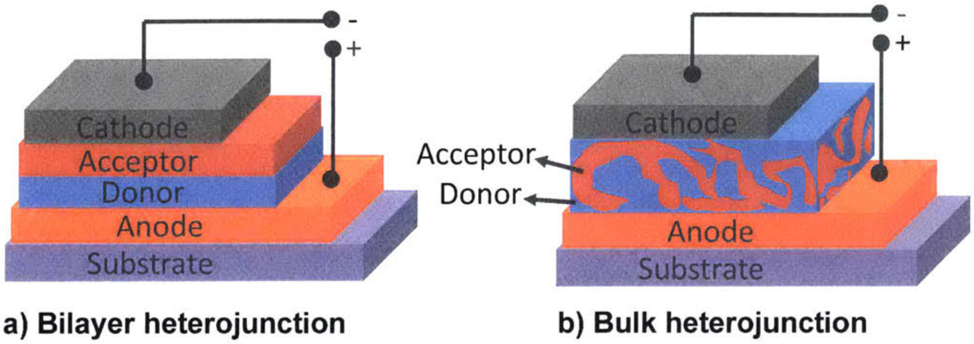

Figure 1-1: A schematic illustration of organic photovoltaics with different architectures. (a) Bilayer OPVs contains two types of semiconducting materials: electron donor and electron acceptor. (b) Bulk heterojunctions have an absorption layer consisting of a nanoscale blend of donor and acceptor materials. The domain sizes of this blend are on the order of nanometers, allowing for excitons with short lifetimes to reach an interface and dissociate due to the large donor-acceptor interfacial area. Image reproduced from Ref. [4].

In this thesis we will mostly focus on organic photovoltaics (OPVs), however many of the theoretical and computational techniques developed here are applicable to other organic/molecular semiconducting systems. OPV are good light absorbers and can be fabricated using scalable processing methods such as roll-to-roll printing. The power conversion efficiencies (PCEs) of OPVs has increased substantially in the past few decades, and a value of 17.3% has recently been reported for tandem-junction devices [5]. These promising advances suggest that OPVs can potentially emerge as a practical renewable energy option via the production of large-scale, cheap and easy-to-process solar cells.

A OPV typically has a layered structure involving a substrate, photoactive layer and electrode (FIG. 1-1). Light is converted to electrical current in the photoactive layer, which has a typical thickness of about 100 nm. In efficient OPVs, this layer is a composite of two or more semiconductors (electron donors and acceptors) mixed

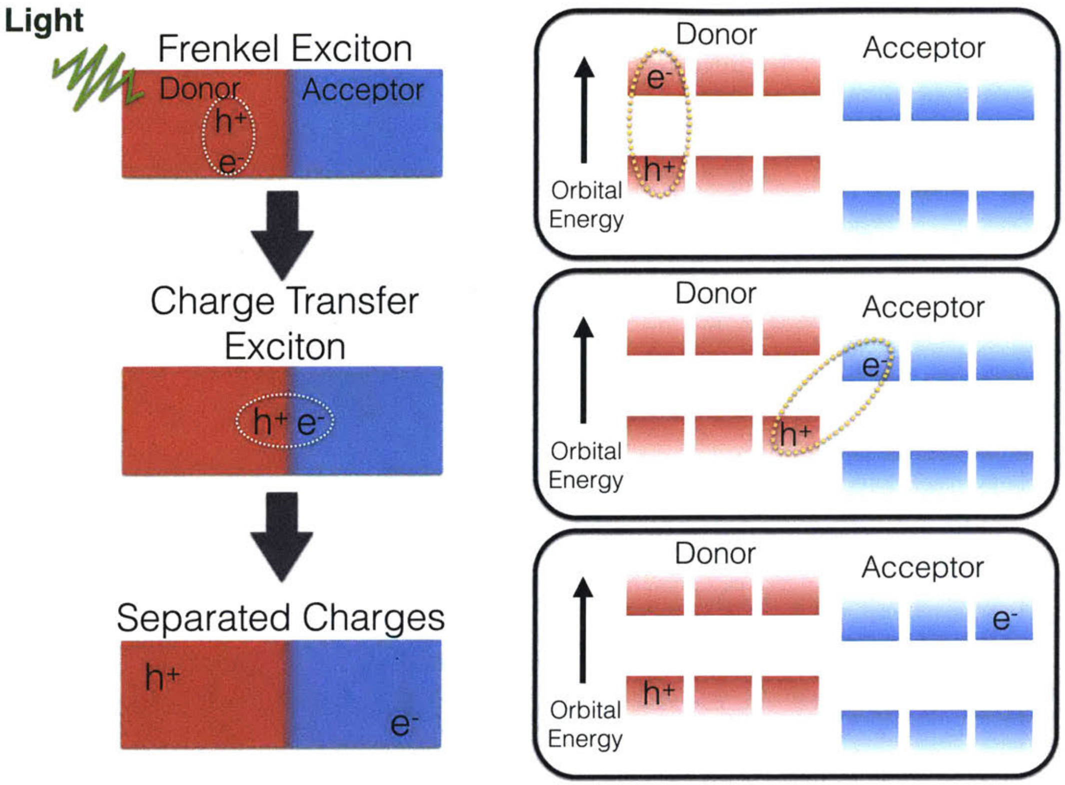
Light
Frenkel Exciton
Donor
Acceptor
h+
e-
Charge Transfer Exciton
h+ e-
Separated Charges
h+
e-
Donor
Acceptor
e-
h+
Orbital Energy
Donor
Acceptor
e-
h+
Orbital Energy
Donor
Acceptor
e-
h+
Orbital Energy

Figure 1-2: Photocurrent generation processes in OPVs. Photon absorption by a molecule in the donor layer promotes an electron to an excited state, resulting in a localized and tightly bound electron-hole pair (a so-called Frenkel exciton). Frenkel exciton migrates to the interface between the (electron) donor and acceptor molecules, resulting in the transient formation of a charge-transfer state whereby the electron and hole resides on different molecules. The dissociation of the charge-transfer exciton is then followed by charge transport where electrons and holes can hop between adjacent electron acceptor and donor molecules respectively.

together to form a nanostructured hetero-junction for charge generation. Photocurrent generation in OPVs is a multistep process that can be summarized in Fig. 1-2. Initially, photon absorption by a molecule in the active layer (typically in the donor materials) promotes an electron to an excited state, resulting in a localized and tightly bound electron-hole pair (a so-called Frenkel exciton). Frenkel exciton can then travel to the donor-acceptor interface where exciton dissociation starts to occur due to the lower LUMO energy in the acceptor materials, resulting in the transient formation of a charge-transfer exciton in which the electron and hole reside on different molecules. At this point, electron and hole are still bound by strong Coulomb attraction despite being spatially separated. The dissociation of the charge-transfer exciton is then followed by charge transport where electrons and holes move between adjacent acceptor and donor molecules respectively. The exact mechanism in which charge-transfer exciton dissociates is still debatable in the community since the Coulombic attraction is an order of magnitude larger than thermal energy at room temperature.

1.3 Organization of Thesis

In this thesis we focus on two processes of particular importance to the performance of OPVs: transport of Frenkel exciton and dissociation of charge-transfer exciton. In Chapter 2, we model the dependence of transport properties Frenkel exciton on excited energy disorder in extended sexithiophene systems by performing extensive classical molecular dynamics simulations and classical electronic structure calculations. We show that the disorder in the excited energy can be temporally and spatially correlated, and these correlations could significantly affect the exciton mobility. In Chapter 3, we propose to incorporate the statistics of energy disorder from atomistic calculations into a coarse-grained tight-binding model and show that it is capable of reproducing results from atomistic simulations albeit at a much lower computational costs. This allows us to study system size of experimental relevance (up to 10,000s of molecules) and the model demonstrates good agreement with many available experimental measurements.

In the second half of the thesis (Chapters 4 and 5) we focus on the dynamics of charge-transfer exciton. In Chapter 4, we introduce a 2-dimensional stochastic hopping model to describe the electron and hole dynamics in a CT exciton. In contrast to the atomistic approach in the Frenkel exciton simulations, the CT exciton model is parametrized using experimental data for a particular donor-acceptor pair. We demonstrate that simulations carried out on our model are capable of reproducing many sets of experimental results as well as generating theoretical predictions related to the efficiency of organic electronic materials. In Chapter 5, we consider the effect of spatial variations in electronic energy levels, such as those that arise in disordered molecular systems, on dissociation yield and demonstrate that it is maximized with a finite amount of disorder. We demonstrate that this is a nonequilibrium effect that is mediated by the dissipation driven formation of partially dissociated intermediate states that are long-lived because they cannot easily recombine.

Chapter 2

Effects of Disorder on Frenkel Exciton Dynamics

2.1 Introduction

Organic semiconductors offer the electronic advantages of traditional semiconductors with the chemical and mechanical benefits of organic compounds, providing an inexpensive, mechanically flexible and electronically tunable alternative to traditional silicon based semiconductors [3, 6–15]. Unlike its inorganic crystalline counterparts whose constituents are bound by strong covalent bonds, weak van der Waals interactions dominate the intermolecular interactions in organic semiconductors, leading to disordered structures with strong electron-phonon couplings. The transport properties of excitons in molecular systems, such as organic semiconductors and quantum dots, are highly sensitive to this nanoscale variations of morphology [16, 17]. Thus accurate modeling of this dependence is crucial for making reliable predictions of device performance. However, the presence of disorder in organic materials renders band theory commonly used in solid state physics inapplicable due to the lack of symmetry. Atomistic electronic structure methods are limited to time and length scales much smaller than required to characterize the exciton transport properties in this class of materials. We often have to rely on site-based phenomenological models to extract the essential exciton transport properties. The parameters in these coarse-grained models can be inferred from experiments or tuned to fit experimental results. Due to their simplicity and computational efficiency, phenomenological models can simulate systems of experimentally relevant sizes and provide deep physical insights into exciton properties. However most phenomenological models do not contain the chemical details of molecules, hence they often fail to capture the subtle but important effects of spatial and temporal correlations in the nanoscale disorder arising from the packing and thermal motions of molecules. These models usually invoke approximations regarding the nature of static and dynamic disorder. For example, static disorder is described by uncorrelated Gaussian variables, whereas dynamic disorder is frequently incorporated in the models as simple white/colored noise or interactions with a bath of quantum harmonic oscillators [18–20]. Since exciton dynamics is highly dependent on the nature of disorder, these assumptions could have huge impact on the theoretical predictions of exciton mobility.

Here we provide a critical assessment of these assumptions and investigate their impacts on exciton transport computations. We used a recently developed hybrid quantum/classical method that compute the site energies and excitonic couplings using quantum chemistry methods on molecular configurations generated by molecular dynamics (MD) simulations [21]. It has been shown that this atomistic method is capable of simulating exciton dynamics across hundreds of small organic molecules with sufficient accuracy. By analyzing the Frenkel exciton Hamiltonian generated by the electronic structure calculations, we characterize the statistical properties of the static and dynamic disorder in conjugated organic films. We show that the disorder in this organic semiconducting material is both spatially and temporally correlated. We further demonstrate that temporal correlation has little impact on exciton transport, while spatial correlation could enhance exciton mobility in highly disordered systems.

2.2 Theory

2.2.1 Frenkel Exciton Model

We adopt a computational framework newly developed in Ref. [21] and express the electronic excitation in a multi-chromophoric system in a basis of localized excitations, and the resulting Hamiltonian is called the Frenkel exciton Hamiltonian [22, 23]. The Frenkel exciton Hamiltonian describes a system of of N excitable subunits (sometimes referred to as sites or chromophores) that can each host a localized exciton. The ground electronic state of the system is denoted as $|0\rangle$, the wavefunction for the localized exciton is $|m\rangle = e_m^\dagger|0\rangle$, where the creation operator $e_m^\dagger$ generates a Frenkel (singlet) exciton localized on the m-th site. The form of the creation operator depends on the selected excited-state electronic-structure method. In the basis of these wavefunctions, the Frenkel excitonic Hamiltonian can be written as

$$H(t) = \sum_i \epsilon_i(t)|i\rangle\langle i| + \sum_{ij} V_{ij}(t)|i\rangle\langle j|, \tag{2.1}$$

where $|i\rangle$ represents a Frenkel (singlet) exciton localized on i-th molecule with excitation energy ϵ_i, and V_{ij} is the excitonic coupling between $|i\rangle$ and $|j\rangle$. Both the energies and couplings are time-dependent due to the thermal fluctuations of nuclei. For notational convenience, we separate the time-dependent and time-independent components in the Hamiltonian such that $\epsilon_i(t) = \epsilon_i + \delta\epsilon_i(t)$ and $V_{ij}(t) = V_{ij} + \delta V_{ij}(t)$ where the time average of the time-dependent components is zero, i.e. $\overline{\delta\epsilon_i(t)} = 0$ and $\overline{\delta V_{ij}(t)} = 0$.

Frenkel exciton Hamiltonian has been used extensively to study exciton transport in various systems, i.e. quantum dots, light harvesting complexes, organic semiconductors, and conjugated polymers [24–28]. The parameters in the Frenkel exciton Hamltonian can in principle be determined by computing the excited state electronic structure of the entire system. However for large systems, this type of computation requires excessive computation power. Hence in many studies, the static components are often modeled phenomenologically as a set of independent Gaussian random vari-

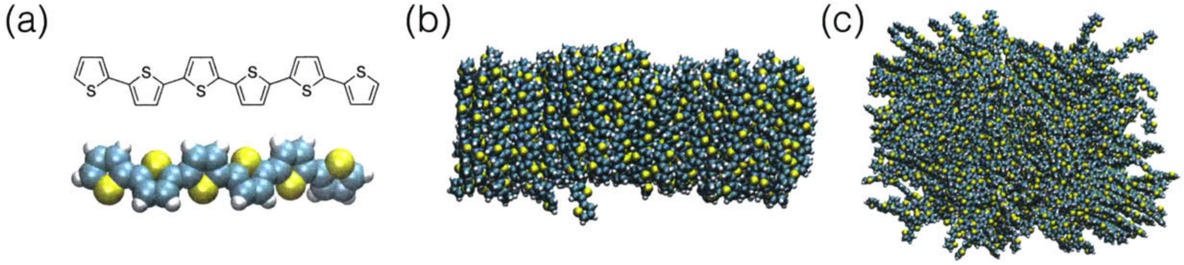

Figure 2-1: Configurations of simulated T6 system in this chapter. (a) An isolated T6 monomer. (b) A T6 monolayer film. (c) A disordered bulk phase of T6 molecules.

ables, whereas the time-dependent components are described as white noise or a bath of quantum oscillators without strong justifications from atomistic simulations. Here we will examine these assumptions by analyzing the properties of static and dynamic disorder in organic thin films generated from atomistic quantum-classical simulations and evaluate their impacts on exciton transport. We adopt a recently redeveloped computational protocol by performing extensive semi-empirical electronic structure calculations on the fly over MD trajectories for conjugated organic films. Instead of performing the electronic structure calculations of the entire system, the calculations are restricted to include only one site at a time while describing all other sites in terms of an effective medium, such as a dielectric continuum.

2.2.2 Modelling of Sexithiophene Films

In this chapter and the next, we focus on organic molecular semiconductors comprised of sexithiophene (T6) molecules. The structural and molecular representation of T6 are given in Figure 2-1(a). The reasons for choosing T6 semiconductors as our model system are three-fold: (1) T6 molecules exhibit high thermal stability and low relative mobility [29] which enable the preparation of high purity materials with controllable morphology [30]. (2) The properties of T6 are very close to those of polythiophene (PT), making it a minimal model system for studying thiophene-based polymeric semiconductors (e.g., P3HT) (3) T6 itself also has broad applications in field-effect transistor, organic light-emitting diode, etc. [31] Hence, there are a large body of experimental and theoretical studies on T6 in the literature, against which we

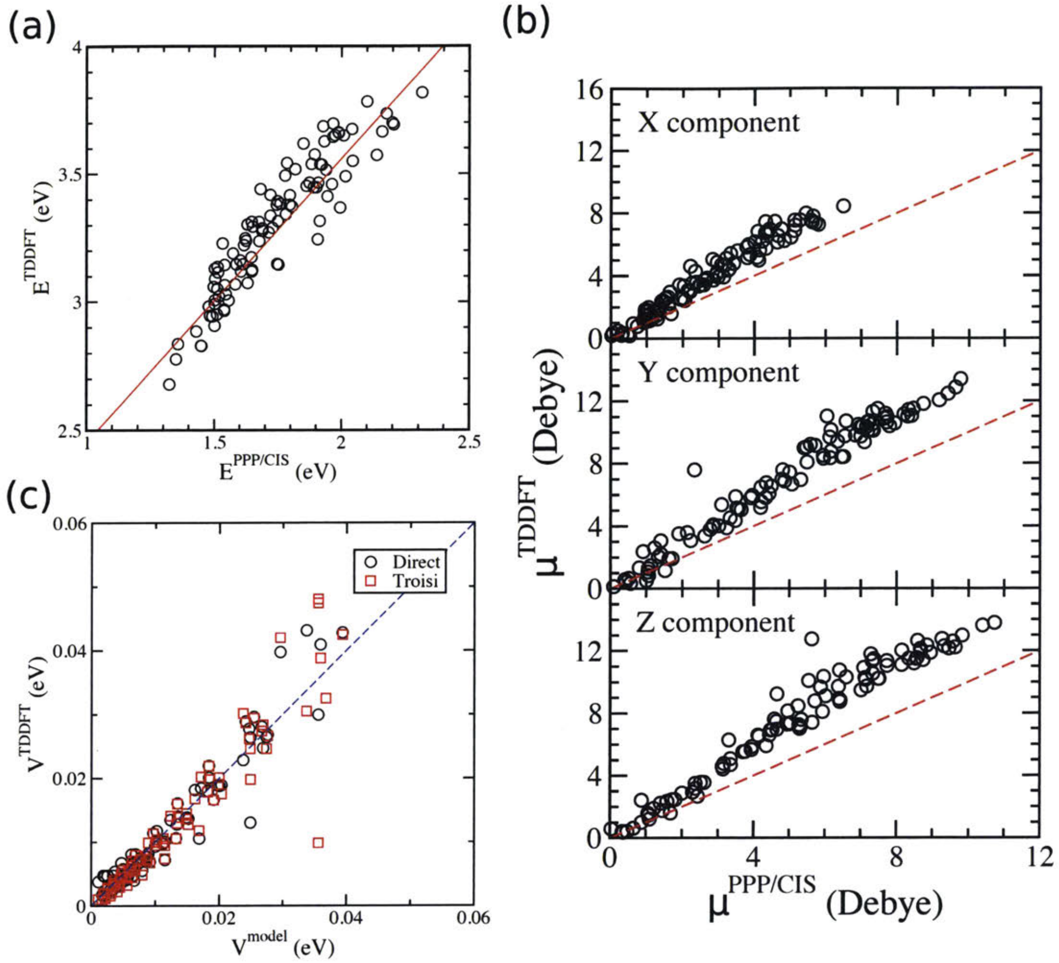

Figure 2-2: Comparison between the calculated properties from the model in this chapter and the more accurate TDDFT: (a) excitation energy in eV for the lowest singlet exciton (the red line indicates the linear fitting after adjusting for systematic error); (b) three Cartesian components of the transition dipole in Debye associated with the lowest singlet exciton; (c) excitonic coupling between the two localized singlet exciton states. Two methods of extracting excitonic couplings from TDDFT calculations are adopted: an energy-gap-based method [32](black circles), and the method described in Ref. [33] (red squares). All the dashed blue lines in this figure indicate the diagonals. Figure reproduced from Ref. [21]

can benchmark and validate our model. More importantly, a variety of T6 film morphologies have been realized and well-characterized in experiments, providing a basis for theoretical studies on the effects of morphology on exciton dynamics.

In the Frenkel exciton model, each T6 molecule is considered as a site, and the Frenkel excitonic Hamiltonian (Eq. 3.1) is represented in the basis of localized exciton on each individual T6 molecule. The site energies and excitonic couplings between sites are computed at an semi-empirical level for configurations harvested from all-atom molecular dynamics (MD) simulations. Specifically, the Pariser-Parr-Pople (PPP) method [34–36] is employed for the SCF calculations, and the detail of and the parameters in the PPP methods can be found in Ref. [21]. The excited- state properties (e.g., exciton site energy ϵ_i) are computed at the level of configuration-interaction singles (CIS). [37]. Due to the zero-differential overlap (ZDO) approximation in the PPP method, the wavefunctions of localized excitons (i.e., the basis functions for the Frenkel exciton Hamiltonian) $|m\rangle$ are orthogonal in our model, so the excitonic coupling is simply given by $V_{mn}(t) = \langle m|H(t)|n\rangle$. The PPP/CIS-based Frenkel exciton model is highly efficient for computing the excited state properties of organic conjugated molecules. The accuracy of the PPP/CIS-based Frenkel exciton model has been benchmarked against higher-level electronic-structure methods and experimental absorption spectra in Ref. [21]. For example,the results of the semi-empirical electronic structure calculations have been compared to that of time-dependent density function theory (TDDFT), which is method of choice for medium-size systems (i.e. hundreds of basis functions), and satisfactory agreement is observed after adjusting for a systematic error (Figure 2-2).

2.2.3 Molecular Dynamics Simulation

The static properties of a Frenkel exciton, such as its energy, depend sensitively on the atomic configurations, and its transport is greatly affected by nuclear motion via the exciton-phonon interaction. In order to properly sample and propagate the atomic configurations, we employed classical molecular dynamics (MD) simulations, using the OPLS/2005 force field. [38] All the all-atom MD simulations were performed with Desmond package 3.6. [39]. In this study, we focus on two T6 films of different morphologies, shown in Figure 2-1(b) and (c). The monolayer film of 150 T6 molecules (Figure 2-1(b)) is intended to mimic the monolayer film grown on the silicon dioxide substrate using the vapor deposition method, and all the T6 molecules in it stand up roughly in parallel to each other. [29, 40–42] The initial configuration of the monolayer film is a regular 2D lattice with a moderate spacing (i.e., 7 Å) between the molecules, and this choice of spacing allows some spatial (in-plane) disorder within the film. The configuration then was equilibrated in the NPT ensemble at 300 K and 1 atm using the Martyna-Tobias-Klein scheme with a coupling constant of 2.0 ps for both temperature and pressure. The simulation box scaled independently along all Cartesian axes, and the box length along the normal to the monolayer film (i.e., Z direction) was kept much larger than the film thickness throughout the simulation, making it an effective 2D NPT simulation. After equilibration, NVT simulation was performed using the Nose-Hoover thermostat with a coupling constant of 2.0 ps. The second film of 343 T6 molecules (Figure 2-1(c)) is highly disordered, and may be considered as a representation of the film grown from solution-based methods (e.g., spin-coating). The initial configuration for the disordered film was a 3D regular lattice with a spacing of 100 Å. This large spacing allows T6 molecules to rotate and relax freely before interacting with each other during the equilibration in the (isotropic) NPT ensemble, rendering the eventual configuration highly disordered in three dimensions. It is worthwhile to note that the film configurations we generated are metastable amorphous structures, which may be encountered in experiment as well. By propagating the nuclei on the ground state potential energy surface we neglect the effects of excited state forces and non-adiabatic derivative couplings on nuclear dynamics. Including these effects in our model is straightforward, however, computing them is computationally expensive. Here, for the sake of efficiency, we omit these effects. For the results presented below we expect that the qualitative consequences of this omission are small and that the primary conclusions would not be altered by the inclusion of excited state forces and/or derivative couplings.

2.3 Results and Discussions

The disordered nature of these two organic films is demonstrated in Figure 2-3(a) which displays a snapshot of molecular configuration of the T6 monolayer film. Figure 2-3(b) shows the corresponding centre-of-mass positions of the molecules in the

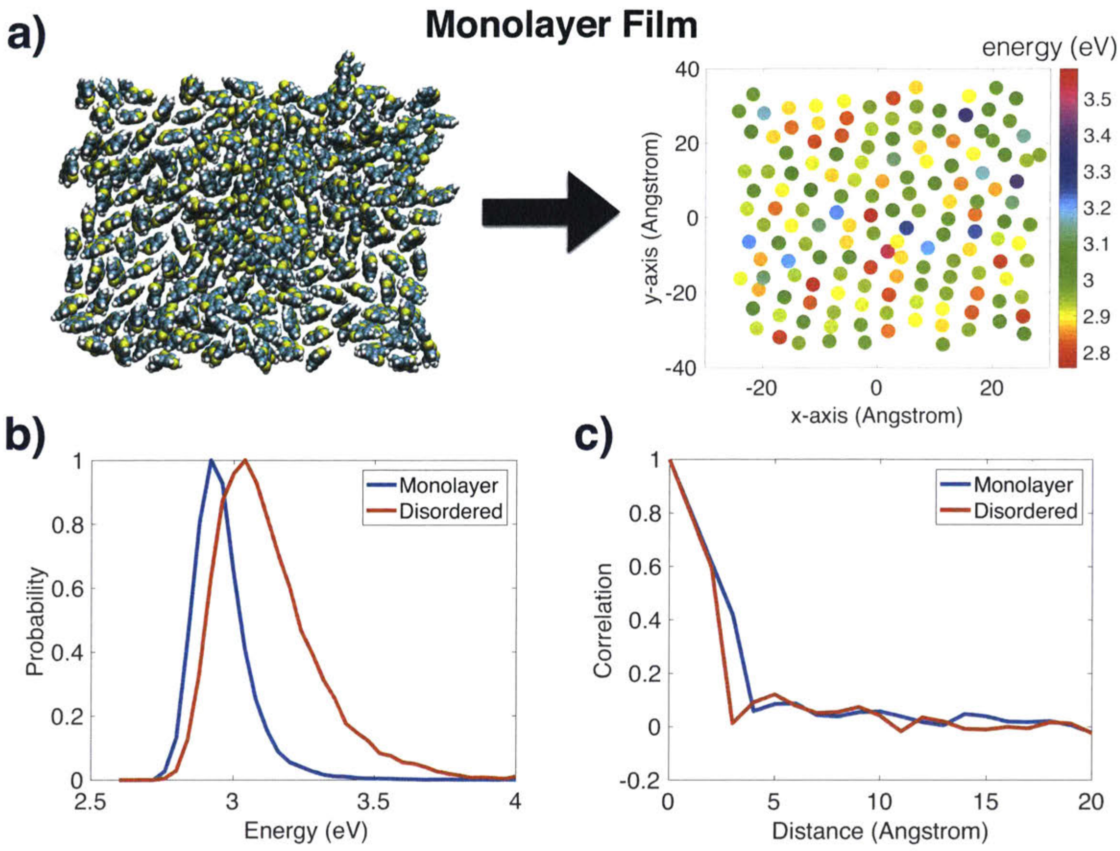

Figure 2-3: (a) A snapshot of molecular configuration of the T6 monolayer film studied in this chapter. (b) The corresponding individual molecule centre-of-mass positions in the T6 monolayer film. The site energies (in eV) of the molecules are represented by the color gradient. (c) Distributions of site energies sampled from 100 MD configurations for T6 monolayer (blue) and disordered film (red). d) The spatial correlation (normalized) of the site energies as a function of center-of-mass distance for T6 monolayer (blue) and disordered film (red).

monolayer film, the excitation energies are represented by the color gradient. The energy map illustrates the randomness in molecule positions (structural disorder) and the uneven energetic landscape commonly found in molecular systems with van der Waals intermolecular interactions. The exciton energy distributions of the monolayer and disordered films sampled from 100 configurations are plotted in Figure 2-3(c), reproducing the results found in Ref. [21]. Both systems exhibit broad distributions of exciton energies, with standard deviations of 0.1eV and 0.18eV for monolayer and disordered films, respectively. The energy distribution in monolayer film is narrower because of its relative structural homogeneity, it is also further red shifted due to its planar geometry (more energetically favorable $\pi - \pi$ interactions). Additionally, both distributions exhibit a non-Gaussian and non-symmetric profile, arising from the non-linear relation between molecular geometry and exciton energy, and the dense packing of molecules which limits the number of accessible low energy states. However we found no significant difference in exciton dynamics if the exciton energies are replaced by Gaussian variables with the same variance and correlations. The compact packing of molecules gives rise to exciton energies that are locally correlated, a statistical property frequently overlooked in coarse-grained models. Here we examine this local correlation by computing the exciton energy spatial correlation function, defined as

$$C(r) = \langle \delta(r - r_{ij}) \, (\epsilon_i - \bar{\epsilon})(\epsilon_j - \bar{\epsilon}) \rangle \tag{2.2}$$

where $\langle \cdots \rangle$ denotes an average over all available configurations of a given system, $\bar{\epsilon}$ is the average site energy for molecules in the system, r_{ij} is the center of mass separation between the molecules associated with sites i and j, and $\delta(x)$ is the Dirac Delta Function. The energy spatial correlations for both monolayer and disordered films are plotted in Figure 2-3(d), showing that the exciton energies of neighboring molecules can be highly correlated but such correlation decays quickly as inter-molecular separation increases beyond nearest neighbors.

Thermal fluctuations of nuclei from the MD simulations give rise to the time-dependence of exciton energies and couplings in the Frenkel exciton Hamiltonian in Eq. 3.1. A sample trajectory of exciton energy as a function of time is plotted in the inset of Figure 2-4a. We study the temporal correlation in these fluctuations by computing the average time correlation functions of the exciton energies,

$$C_\epsilon(t) = \frac{\langle (\epsilon_i(t) - \bar{\epsilon})(\epsilon_i(0) - \bar{\epsilon}) \rangle}{\langle (\epsilon_i - \bar{\epsilon})^2 \rangle}, \tag{2.3}$$

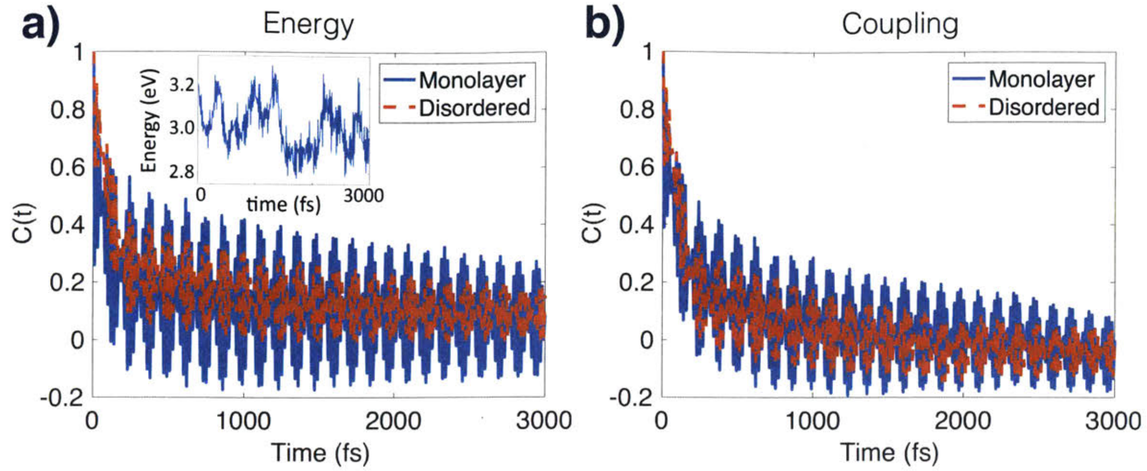

Figure 2-4: a) The average time correlation functions (normalized) of the site energies in T6 monolayer (solid blue) and disordered films (dashed red). b) The average time correlation function (normalized) of the excitonic couplings in T6 monolayer (solid blue) and disordered films (dashed red).

and the intermolecular electronic couplings,

$$C_V(t) = \frac{\langle (V_{ij}(t) - \bar{V})(V_{ij}(0) - \bar{V}) \rangle}{\langle (V_{ij} - \bar{V})^2 \rangle}, \tag{2.4}$$

where $\langle \cdots \rangle$ indicates the ensemble average over initial configurations. The time correlation functions are plotted in Figure 2-4, which show that both energy and coupling time correlations are highly non-monotonic with two important features: 1) An initial fast decay within 100 − 200fs due to the dephasing effect from nuclear ballistic motion. 2) Long lasting oscillations with periods of approximately 20fs and 100fs, resulting from the C-C bond and C-H bond stretching, respectively. The results above demonstrate that these time correlations are distinctly different from those used in many empirical methods which often assume noise with delta or exponential time correlation [43, 44]. Even rigorous open quantum system treatment can fail to capture the details of exciton-phonon couplings because it often assumes spectral densities that are more relevant to crystalline solid state systems (e.g. Lorentzian or Ohmic spectra) [45]. Recently, there have been several works on combining MD and excited state electronic structure calculations to extract realistic bath correlation function/spectral

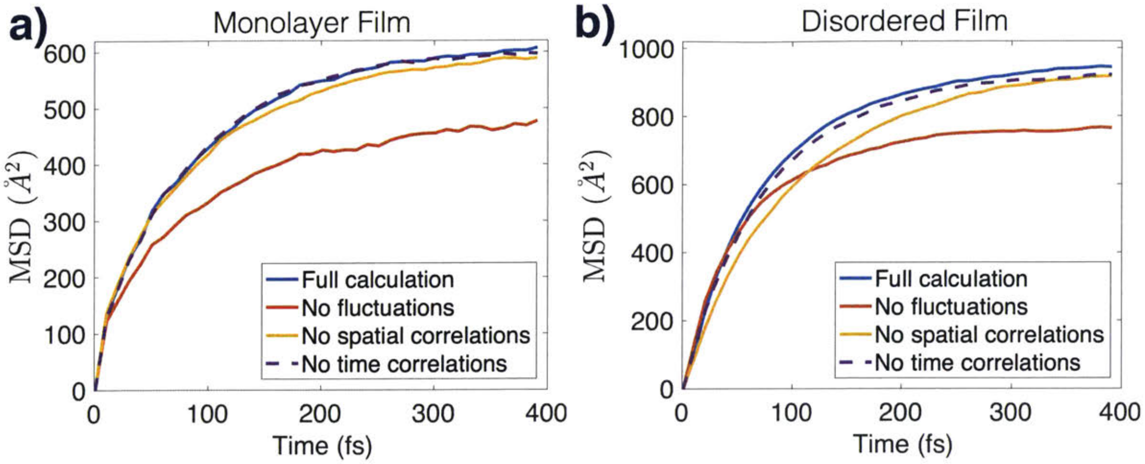

Figure 2-5: Average mean-squared-displacement (MSD) of an initially localized exciton in (a) monolayer and (b) disorder films under different conditions: full molecular calculations generated at the level of QM/MM (solid blue), calculations with no time-dependent fluctuations (solid red), calculations with no spatial correlation in the static disorder (solid orange) and calculations with no time correlation in the time-dependent fluctuations (dashed magenta).

density [46–49], but they are limited to small light harvesting systems due to the computational cost. It is still not unambiguously clear if exciton transport depends on the memory effect (non-Markovianity) of exciton-phonon couplings, the works of Ref. [50, 51] for light harvesting complexes seem to suggest it might be parameter (or system) dependent.

2.3.1 Mean Squared Displacement

To investigate how exciton dynamics depends on the non-Markovianity and other properties of disorder, we solve the time-dependent Schrodinger equation to obtain the exciton wavefunction, $|\psi(t)\rangle = \hat{T}e^{-\frac{i}{\hbar}\int H(t')dt'}|\psi(0)\rangle = \sum_i c_i(t)|i\rangle$, where $\hat{T}$ is the time-ordering operator and $c_i(t)$ is the wavefunction coefficient in the molecular site basis. From the solution of the Schrodinger equation, we can then compute the mean-squared-displacement (MSD) defined as

$$MSD(t) = \langle \sum_i |c_i(t)|^2 \, \vec{r}_i^{\,2}(t) \rangle, \tag{2.5}$$

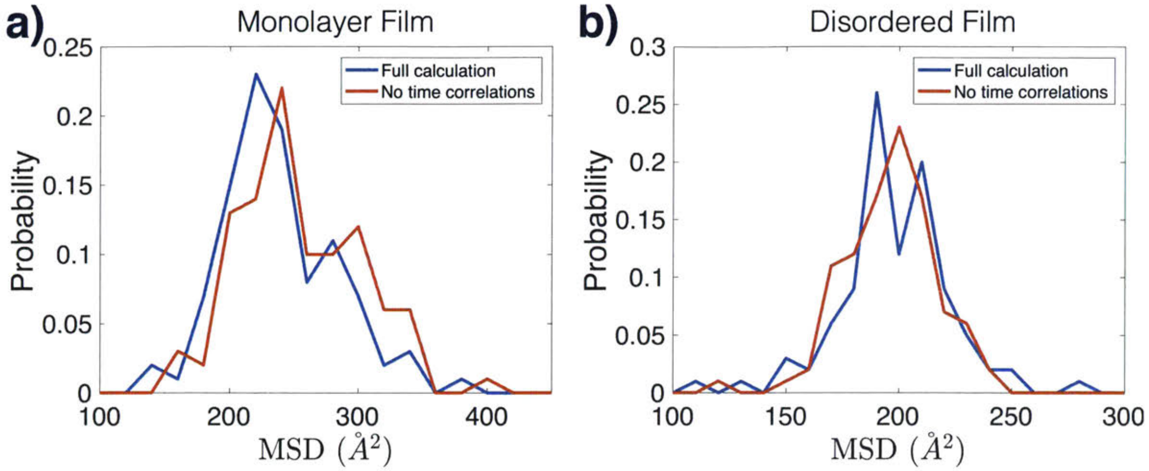

Figure 2-6: Distributions of MSDs at $t = 100$fs from 100 initial configurations in (a) monolayer and (b) disorder films under two different scenarios: full molecular calculations generated at the level of QM/MM (blue), calculations with no time correlation in the time-dependent fluctuations (red).

where $\vec{r}_i(t)$ is the center-of-mass position of the i-th molecule at time t, and $\langle . \rangle$ represents the ensemble average over 100 initial configurations. The origin is conveniently chosen to be the site of the initial localized excitation. In the following we study the effect of disorder on the exciton MSDs, since it is a measurable quantity through spatially resolved photoluminescence experiments [16]. MSDs generated from Hamiltonian in Eq. 3.1 for monolayer and disorder films with initially localized exciton are plotted in Figure 2-5 (solid blue lines). In both systems, the exciton wavefunction diffuses rapidly within the first 100fs before plateauing due to the finite-size effect. The final value of MSD in the disordered film is higher because of its larger system size compared to the monolayer film.

To illustrate the effect of time dependent fluctuations on exciton dynamics, we repeat the calculations generated from the same Hamiltonian but without the time-dependent components, i.e. we set $\delta V_{ij}(t)$ and $\delta \epsilon_i(t)$ to zeros. The resulting MSDs are shown as solid red lines in Figure 2-5. We observed a significantly reduced exciton mobility due to the localization of wavefunction from the interference between scattered waves in disordered energy landscape, a phenomenon commonly known as Anderson localization in condensed matter physics community [52]. The interference

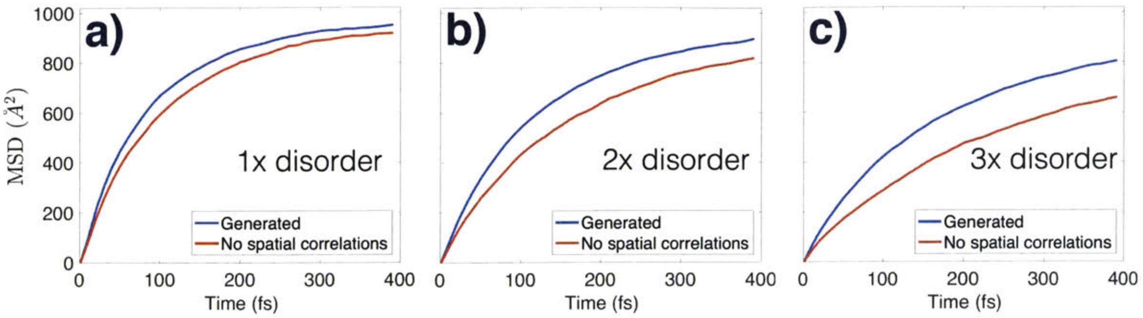

Figure 2-7: Average mean-squared-displacement (MSD) of an initially localized exciton in disordered film generated from full molecular calculations (blue lines) and calculations with no spacial correlations in disorder (red lines). The magnitude of static disorder is artificially increased by (a) no increase, (b) 100% and (c) 200% to demonstrate that the effect of spatial correlation is dependent on the magnitude of static disorder.

pattern is destroyed in the presence of fluctuating noise (i.e. decoherence), thus giving rise to “noise-assisted" exciton transport frequently reported in the light-harvesting systems [53–55].

To investigate the non-Markovian effect on exciton dynamics, we replace the time-dependent components (i.e. $\delta\epsilon_i(t)$ and $\delta V_{ij}(t)$) in the Hamiltonian with Gaussian white noise of the same magnitude, and found that the resulting MSDs (yellow lines in Figure 2-5) are nearly identical to the MSDs generated from full molecular calculations. For more critical assessment, we examine the distribution of MSDs (at t = 100fs) from 100 individual trajectories, shown in Figure 2-6. We again found the MSD distributions generated from molecular simulations and from Hamiltonian with Gaussian white noise to be similar. This suggests that memory-effect in the fluctuations does not play an important role in exciton transport for this class of organic semiconducting materials, similar to the conclusion found in Ref. [51] for B850 light harvesting systems at room temperature though the effect could be significant at lower temperature.

Another often overlooked aspect of disorder in empirical models is the effect of spatial correlation on exciton dynamics. We investigate such dependence by computing the MSD generated from a Hamiltonian generated without spatial correlation in the static disorder (dashed lines in Figure 2-5). The effect of spatial correlation on ex-

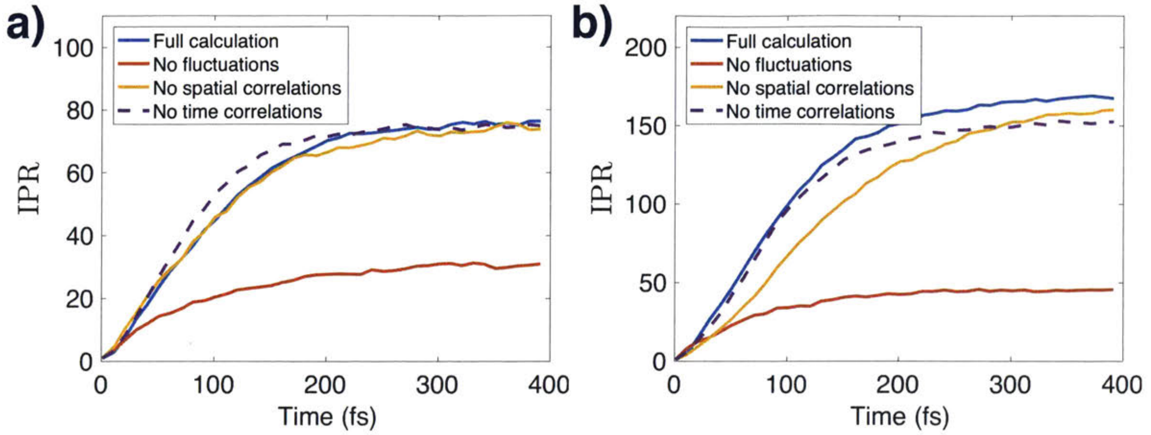

Figure 2-8: Average IPR of an initially localized exciton in (a) monolayer and (b) disorder films under different scenarios: full molecular calculations generated at the level of QM/MM (solid blue), calculations with no time-dependent fluctuations (solid red), calculations with no spatial correlation in the static disorder (solid orange) and calculations with no time correlation in the time-dependent fluctuations (dashed magenta).

citon dynamics is found to be system dependent: it has little effect on the monolayer film, but reduces the exciton mobility in the disordered film. Since the major difference between monolayer and disordered films is the magnitude of static disorder (see Figure 2-3b), this suggests that effect of spatial correlation might be related to how disordered a system is. To test this hypothesis, we artificially increase the amount of static disorder in the disordered film, and the resulting MSDs plotted in Figure 2-7 indeed show that the effect of spatial correlation increases with the magnitude of static disorder. This result suggests that the effect of local energetic correlation is more prominent in highly disordered systems, like those found in solution-processed organic semiconducting thin films.

2.3.2 Inverse Participation Ratio

Another useful measure to characterize exciton dynamics is the time-dependent inverse participation ratio (IPR)

$$\mathrm{IPR} = \frac{1}{\sum_i |c_i(t)|^4}, \tag{2.6}$$

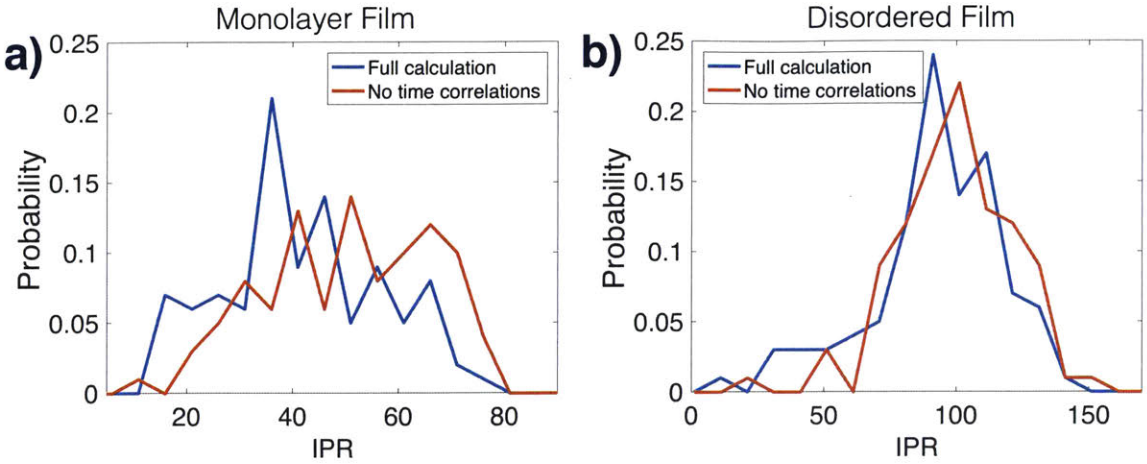

Figure 2-9: Distributions of IPRs at $t = 100$fs from 100 initial configurations in (a) monolayer and (b) disorder films under two different conditions: full molecular calculations generated at the level of QM/MM (blue) and calculations with no time correlation in the time-dependent fluctuations (red).

where $c_i(t)$ is the wavefunction coefficient in the site basis from the solution of the time-dependent Schrodinger equation. IPR represents qualitatively the number of sites/molecules "participates" in the wavefunction and serve as an alternative measure of exciton transport to the MSD. For example, if the exciton wavefunction is localized in just one molecule, the then IPR = 1. On the other hand, if exciton wavefunction is evenly delocalized in a system of N sites/molecules, IPR = N since $c_i = 1/\sqrt{N}$. IPRs generated from the Hamiltonian in Eq. 2.6 in the main text for monolayer and disorder films with initially localized exciton are plotted in Figure 2-8 (solid blue lines). In both systems, IPRs increase rapidly within the first 200fs before plateauing due to the finite-size effect. The final value of IPR in the disordered film is higher because of its larger system size compared to the monolayer film.

We also explore IPRs generated under different conditions in Figure 2-8: calculations with no time-dependent fluctuations (solid red lines), calculations with no spatial correlation in the static disorder (solid orange lines), and calculations with no time correlation in the time-dependent fluctuations (dashed magenta lines). In general, the qualitative behaviors under each condition are very similar to those found in the analysis of MSDs in the previous section. IPRs generated from the same Hamil-

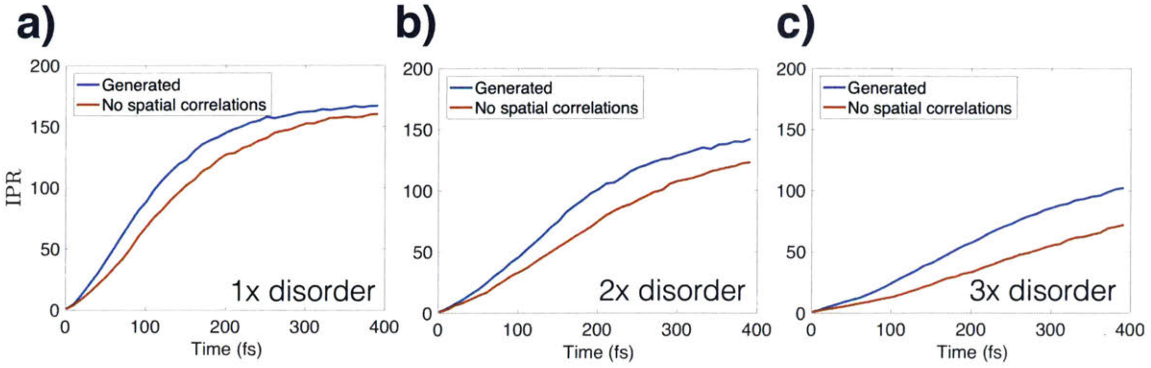

Figure 2-10: Average IPR of an initially localized exciton in disordered film generated from full molecular calculations, but with the magnitude of static disorder is artificially increased by (a) no increase, (b) 2 times and (c) 3 times to demonstrate that the effect of spatial correlation is dependent on the magnitude of static disorder.

tonian but without the time-dependent components (i.e. $\delta V_{ij}(t) = 0$ and $\delta \epsilon_i(t) = 0$) results in a significantly reduced IPR due to the Anderson localization effect. Figure 2-8 also shows that temporal correlation does not play an important role in exciton transport as the IPR generated from the Hamiltonian without temporal correlation (dashed magenta lines) is nearly identical to the IPR generated from the molecular simulations (solid blue lines). The distributions of IPRs at $t = 100fs$ sampled from 100 initial configurations are plotted in Figure 2-9, which again shows that the IPR distributions generated from molecular simulations and from Hamiltonian with white noise to be similar, confirming the minimal effect of temporal correlation. Similar to the findings in MSDs, the effect of spatial correlation on IPRs is system dependent: it has little effect on the monolayer film, but reduces the IPR in the disordered film (dashed lines in Figure 2-8). Figure 2-10 shows the IPR in disordered film with its static disorder artificially increased, and our results demonstrate that the effect of spatial correlation on IPR increases with the magnitude of static disorder.

2.4 Conclusions

In summary, we study the properties of nanoscale disorder in organic thin films of T6 molecules, explicitly generated from atomistic electronic structure calculations over the MD trajectories. We also critically assess the validity of many assumptions used in empirical models regarding the nature of disorder and how they affect exciton transport. We find that disorder in these organic films is both spatially and temporally correlated. The spatial correlation is largely limited to nearest neighbors, whereas the temporal correlation is highly oscillatory and long-lived. It is found that effect of temporal correlation on exciton transport is minimal, but spatial correlation could enhance exciton mobility in highly disordered systems. Our study here constitutes one of the first quantum chemistry based attempts to characterize disorder in extended organic semiconducting materials, and provide important insights into the effects of disorder on exciton transport. Our results could be used to benchmark and improve many widely used phenomenological models.

Chapter 3

Coarse-Grained Modeling of Frenkel Exciton Dynamics

3.1 Introduction

The variations in the nanoscale morphology of organic semiconducting materials could have significant impact on their macroscopic optoelectronic properties. For example, exciton diffusion length of the same material can vary significantly depending on the molecular packing order [56–58]. However the systematic relation between the microscopic morphology and macroscopic electronic properties is not always unambiguously clear and could not be easily revealed through directly experimental measurements. Theoretical or computational inputs are often required for understanding such functional relation and extracting physical insights. The dependence of optoelectronic properties on molecular morphology emerges due to the presence of highly collective molecular excitations that involve the simultaneous participation of many individual molecules. Therefore the system size required to characterize such dependence is typically beyond the computational capability of most first principle methods. Furthermore, unlike its inorganic counterparts, organic semiconductors do not exhibit long range symmetry, this renders many theoretical techniques (i.e. band theory) in solid state physics inapplicable in this class of materials. Thus empirical phenomenological approaches such as site-based hopping or tight-binding models are often used to study the transport properties in organic semiconductors [18–20]. . Phenomenological models are highly computationally efficient and capable of simulating extended systems sufficiently large to extract reliable transport coefficients. However, a major shortcoming of this approach is the lack of chemical specificity which limits its predictive power, though this can be partially mitigated through proper parametrization.

In this chapter, we propose a computational framework to incorporate chemical details into empirical tight-binding model based on the input from atomistic simulations of moderate-sized systems. Specifically, we construct a time-dependent tight-binding Hamiltonian generated from running extensive molecular dynamics (MD) and electronic structure calculations. Since the tight-binding Hamiltonian contains the important chemical information of the molecules, we could in principle parametrize an empirical tight-binding model by constructing a Hamiltonian that has the same statistical properties as the one generated from the atomistic simulations. Indeed, we show that this approach reproduces exciton dynamics that are in good agreement with those from full atomistic simulations, but at a much lower computational cost. More importantly, once enough statistics are gathered, the empirical tight-binding model could be extended to study systems of much larger sizes and different morphologies. In the following we first briefly review the atomistic calculations used in generating the statistics of the tight-binding Hamiltonian. We perform multiple comparisons between the exciton dynamics generated from the atomistic and the empirical tight-binding Hamiltonians, and show that the agreements are satisfactory. We then extend our method to much larger systems that are practically beyond the reach of any first-principle approaches, study the dependence of exciton diffusion coefficients on the properties of disorder and temperature. We show that the results are consistent with available experimental measurements.

3.2 Theory

Similar to the previous chapter, we employ a computational framework that performs extensive semi-empirical Pariser-Parr-Pople (PPP) electronic structure calculations

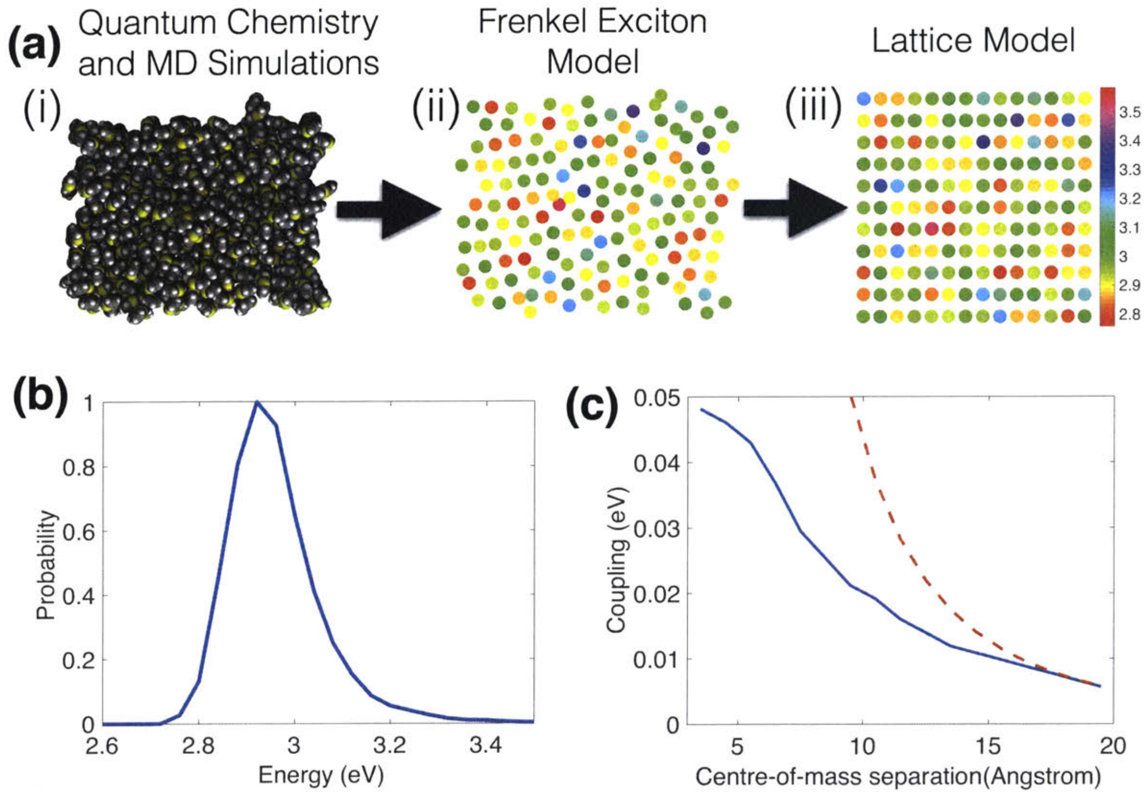

Figure 3-1: (a) (i) Molecular configuration of a monolayer of T6 molecules studied in this chpater. (ii) A snapshot of the individual molecule centre-of-mass positions in the T6 monolayer film. The site energies of the molecules are represented by the color gradient (in eV). (iii) Coarse-grained lattice model that intends to mimic the exciton dynamics of monolayer T6 film. (b) Distributions of exciton site energies sampled from 100 MD configurations of the T6 monolayer film. (c) The average excitonic coupling as a function of center-of-mass separation (solid line). The scaling relation of dipole-diploe coupling (dahsed line) is included for comparison.

on the fly over MD trajectories for a film of conjugated small molecules. Here we first consider a monolayer film of 150 sexithiophene(T6) molecules (shown in Figure 3-1a(i)) generated from MD simulation at $T = 300K$. The disordered nature of the system is illustrated in Figure 3-1a(ii) which shows a snap shot of the random molecular center-of-mass positions, and the excitation energies of molecules are represented by the color gradient. The disorderedness in the energy landscape and molecular positions (structural disorder) shown in Figure 3-1a(ii) is common in organic semiconductors as a result of weak intermolecular bonding. Figure 3-1b shows the distribution of exciton energies sampled from 100 molecular configurations with a standard deviation of 104 meV. The average excitonic couplings between molecules as a function of molecular center-of mass separation is shown in Figure 3-1c (solid line), showing clear deviation from dipole-dipole couplings at small intermolecular separation (dashed line). Despite the efficiency of the quantum-classical method used here (and in the previous chapter), it can only simulate systems consist of up to several hundreds T6 molecules over tens of picoseconds in a medium size computer cluster (several hundred CPU cores). This system size is insufficient to extract reliable material specific transport properties (i.e. diffusion coefficient) due to finite size effect. For studying transport properties in system with long-range interactions like those found in many organic materials, we typically require system size that is at least an order of magnitude larger, i. e. several thousand T6 molecules. Such system size is practically beyond the reach of all quantum chemistry methods, thus phenomenological models are often employed for studying exciton or charge transport in organic semiconductor. While phenomenological models are computationally efficient, they typically lack chemical details of the material and often invoke unjustified approximations regarding the nature of the electronic properties. For example, the site energies are often assumed to be independent Gaussian random variables and the excitonic couplings are limited to nearest neighbors or dipole-dipole couplings.

The form of the tight-binding Hamiltonian is the same as the previous chapter:

$$H(t) = \sum_i \epsilon_i(t)|i\rangle\langle i| + \sum_{ij} V_{ij}(t)|i\rangle\langle j|, \tag{3.1}$$

where $|i\rangle$ represents a Frenkel (singlet) exciton localized on i-th molecule with excitation energy ϵ_i, and V_{ij} is the excitonic coupling between $|i\rangle$ and $|j\rangle$. Both the energies and couplings are time-dependent due to the thermal fluctuations of nuclei. For notational convenience, we separate the time-dependent and time-independent components in the Hamiltonian such that $\epsilon_i(t) = \epsilon_i + \delta\epsilon_i(t)$ and $V_{ij}(t) = V_{ij} + \delta V_{ij}(t)$ where the time average of the time-dependent components is zero, i.e. $\overline{\delta\epsilon_i(t)} = 0$ and $\overline{\delta V_{ij}(t)} = 0$.

In the following, we propose a methodology to incorporate molecular chemical details generated from atomistic simulations into phenomenological models. Specifically, we approximate the T6 film as a two dimensional lattice (Figure 3-1a(iii)) with approximately the same molecular density as systems generated from MD simulations. For the monolayer T6 film in Figure 3-1a (ii), we map the system into a 11 by 14 lattice with a lattice constant of 4.8Å. The static component of the site energies (ϵ_i) are drawn from the distribution in Figure 3-1b. Due to the structural correlation of the molecules, the site energies are locally correlation. We previously found that such spatial correlation can be significant between nearest neighbors but decays rapidly as intermolecular separation increases. In the coarse-grained lattice model, we assume an exponential spatial correlation function, $C(r_{ij}) = \exp(-r_{ij}/r_c)$ where r_{ij} is the center-of-mass separation between molecule i and j, and r_c is the correlation length. We use a correlation length of 4.8Å(one lattice constant). Since the lattice structure of the model does not take into account the structural disorder in the system, we artificially increase the magnitude of the static disorder from 104meV to 260meV (2.5 timer larger) to compensate for the omission of structural disorder. The static disorder scaling factor is the only free parameter in the coarse-grained lattice model, chosen to fit the exciton dynamics from the atomistic model. The static intermolecular excitonic couplings, V_{ij}, are taken from Figure 3-1c.

We approximate the time-dependent components ($\delta\epsilon(t)$ and $\delta V(t)$) of the Hamiltonian as Gaussian white noise. The properties of the white noise can be inferred from the atomistically generated Frenkel Hamiltonian: the variance of the site energy variation can be computed by taking the average variance of $\delta\epsilon_i(t)$ across all molecules, i.e. $\sigma^2_{\delta\epsilon} = \langle\overline{\delta\epsilon_i^2(t)}\rangle$, where $\langle . \rangle$ represents the average over all molecules and overline represents time average. The variance of the off-diagonal fluctuations, $\delta V_{ij}(t)$, is proportional to its static part, $\sigma^2_{V_{ij}} = \left\langle \frac{\overline{\delta V^2_{kl}(t)}}{V^2_{kl}} \right\rangle_{kl} V^2_{ij}$, where $\langle . \rangle_{kl}$ represents average over all molecule pairs. Additionally, it was found in Chapter 2 that both $\delta V_{ij}(t)$ and $\delta\epsilon_i(t)$ are temporally correlated, but our earlier study showed that non-Markovianity does not seem to play an important role in the transport properties in T6 systems, and Gaussian noise is a good approximation of the time-dependent fluctuations.

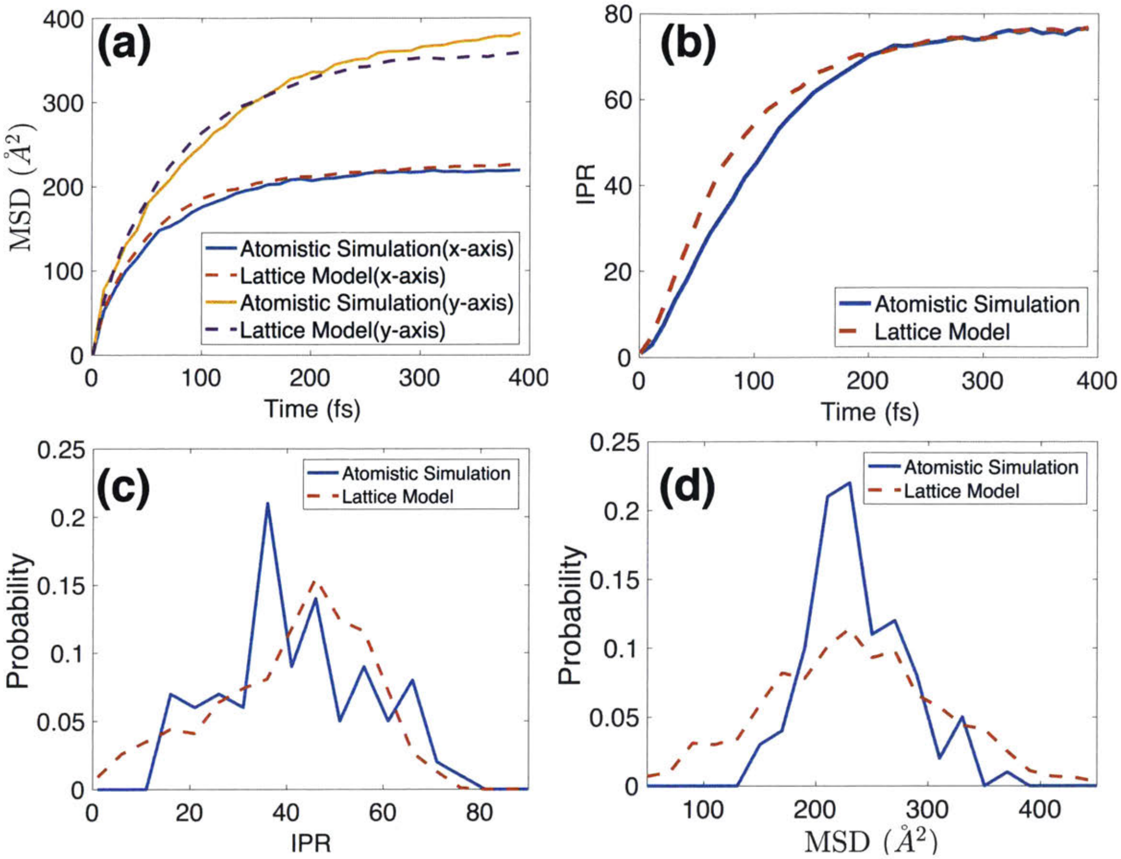

Figure 3-2: Comparisons between atomistic model (solid lines) and coarse-grained lattice model (dashed lines). (a) Average mean-squared-displacement (MSD) of an initially localized exciton. (b) Average time-dependent inverse participation ration (IPR) of an initially localized exciton. (Bottom) Distributions of individual trajectory (c) MSD and (d) IPR at $t = 100$fs sampled from 100 initial configurations.

3.3 Results and Discussions

To access the accuracy of the coarse-grained lattice model, we compare its exciton dynamics with those generated from the atomistic quantum-classical simulations. Similar to Chapter 2, we solve the Schrodinger equation from each model to obtain the time-dependent exciton wavefunction, $|\psi(t)\rangle = \hat{T}\mathrm{e}^{-\frac{i}{\hbar}\int H(t')dt'}|\psi(0)\rangle = \sum_i c_i(t)|i\rangle$, where $\hat{T}$ is the time-ordering operator and $c_i(t)$ is the wavefunction coefficient in the molecular site basis. As in Chapter 2, we then compute the mean-squared-displacement (MSD) from the solution of the Schrodinger equation

$$\mathrm{MSD}(t) = \langle \sum_i |c_i(t)|^2 \, \vec{r}_i^{\,2}(t) \rangle, \tag{3.2}$$

where $\vec{r}_i(t)$ is the center-of-mass position of the i-th molecule at time t, and $\langle . \rangle$ represents the ensemble average over 100 initial configurations. The origin is chosen to be the position of the initially localized exciton. We compare the MSDs (along x and y-axes) generated from the coarse-grained lattice model and the atomistic model in Figure 3-2a, and observe good agreement between the two models. Due to finite size effect, the MSDs starts to plateau after 100fs before reaching the diffusion regime, suggesting larger system size is needed for accurate estimation of diffusion coefficient. We next consider the time-dependent inverse participation ratio (IPR), defined as

$$\mathrm{IPR} = \frac{1}{\sum_i |c_i(t)|^4}. \tag{3.3}$$

IPR is a useful measure to characterize the extent of delocalization of exciton wavefunction and represents qualitatively the number of sites/molecules "participates" in the wavefunction. For example, if the exciton wavefunction is localized in just one molecule, then IPR $= 1$. On the other hand, if exciton wavefunction is evenly delocalized in a system of N sites/molecules, IPR $= N$ since $c_i = 1/\sqrt{N}$. The comparison of IPRs generated from the lattice coarse-grained and atomistic models is shown in Figure 3-2b, and we again observe good agreement. Similar to the MSDs in Figure 3-2a, both models predicts fast initial delocalization within the first 100fs before plateauing due to finite size effect. For more critical assessment, we also compare the distributions of MSDs and IPRs from 100 individual trajectories at $t =$ 100fs, shown in Figure 3-2c and 3-2d, respectively. We again obtain good quantitative agreement between the coarse-grained lattice model and the atomistic model, although the distributions of MSD and IPR from the coarse-grained model are slightly broader, possibly due to the lattice structure of the coarse-grained system.

The agreements from the multiple comparisons above demonstrate that the coarse-

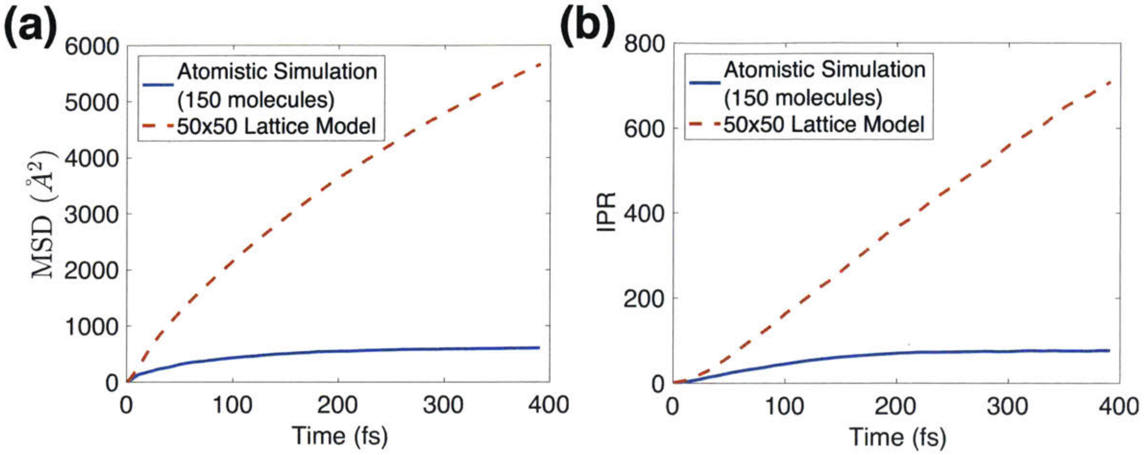

Figure 3-3: (a) Average mean-squared-displacement (MSD) and (b) inverse participation ration (IPR) of an initially localized exciton from a 50 by 50 coarse-grained lattice model (dashed lines). The corresponding MSD and IPR from atomistic simulation of 150 molecules (solid lines) are included to demonstrate the significant finite size effect.

grained lattice model can generates exciton dynamics similar to those from the more costly atomistic simulations. The computational efficiency of the lattice model allows us to study systems of sizes beyond the computational capability of any atomistic models while still retain a certain level of chemical details. For demonstration, we consider a film of 2500 T6 molecules on a 50 by 50 lattice (16 times larger than the system consider in Figure 3-1a), the corresponding MSD and IPR of an exciton initially localized at the center of the film are shown in Figure 3-3 (dashed lines). In contrast to the previous 150-molecule system (solid lines), we do not encounter significant finite-size effect in the 50-by-50 lattice within the simulation time of 400fs. Our results also show that the finite size effect of the smaller system is significant even at short time due to the long range couplings which cause the exciton wavefunction to delocalize rapidly. The one-dimensional (1D) diffusion coefficient in this system is found to be approximately $0.26\text{cm}^2\text{s}^{-1}$. Based on experimentally measured diffusion lengths and lifetime measurements, the experimental exciton diffusion constant of T6 film is estimated to be between 0.09-0.36 cm^2/s [41, 59] and our calculated diffusion constant is in good agreement with the estimated experimental value.

Given that exciton transport is sensitive to the details of molecular morphology

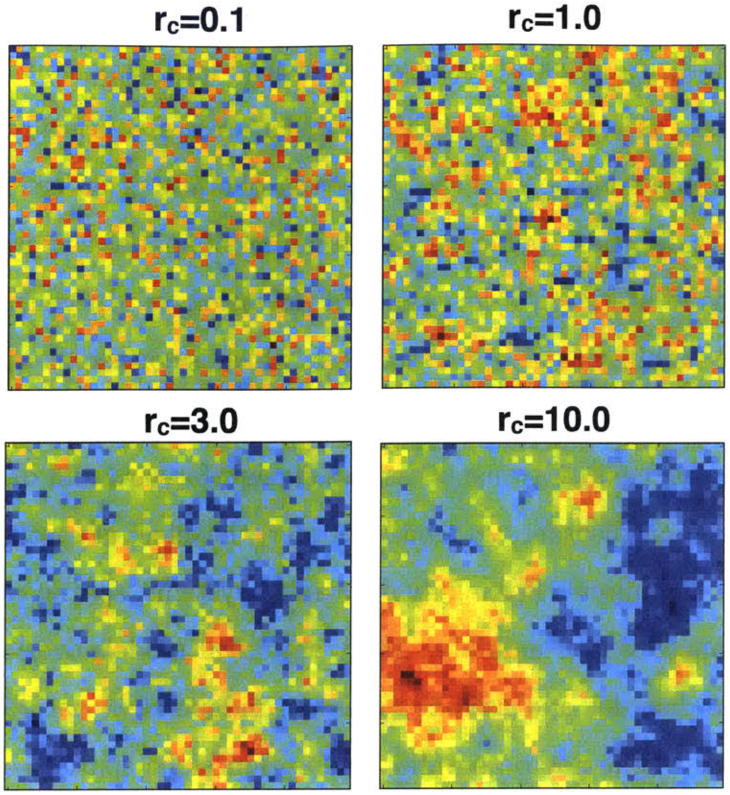

Figure 3-4: Single realizations of random exciton energy landscape in a 50 by 50 lattice at increasing correlation lengths, r_c (in unit of lattice constant).

(static disorder) and fluctuations (dynamic disorder), it is important to characterize such dependence in order to provide reliable theoretical predictions and device design guidance. For example, it is well-known in the condensed physics community that the presence of static disorder can reduce or even halt quantum transport due to the localization of wavefunctions [52]. However, it is found that the localization effect can be lifted with the addition of time-dependent noise [18], indicating finite thermal fluctuations would aid exciton transport. Another important but much less studied aspect of exciton transport is its dependence on the local energy correlation from dense molecular packing. Such local correlation could have important impact on device efficiency. Earlier study has shown that exciton transport efficiency in light harvesting complex is sensitive to to the spatial correlation of the phonon bath [60]. In a separate study, it is found that charge mobility is significantly enhanced by the spatially correlated disorder in organic materials [61].

Figure 3-4 shows single realizations of the site energy landscape at different values of correlation length, r_c, illustrating how the energy landscape could form domains with increasing sizes as r_c increases. In Figure 3-5a, we systematically investigate the dependence of exciton transport on the properties of static disorder in site energy, ϵ_i. by plotting the 1D diffusion coefficient as a function of spatial correlation length, r_c, at different values of static disorder standard deviation, σ. In general we observed decreased exciton mobility as disorder increases, which is consistent with many earlier theoretical and experimental predictions [14–16, 18]. On the other hand, the effect of spatial correlation on exciton transport is less straightforward and dependent on the magnitude of the static disorder. At small disorder, the effect of spatial correlation on exciton transport is minimal. For highly disordered systems, spatial correlation could significantly enhance exciton mobility. Many empirical models overlooks the spatial correlation in the disorder and assume Gaussian independent variables, our results above suggest this might not be a valid assumption since spatial correlation could have important effect on exciton dynamics, especially in highly disordered systems like those found in solution-based organic semiconductors.

3.4 Temperature Dependence

Finally we study the temperature dependence of the exciton dynamics in Figure 3-5b. Treating the time-dependent components of the Hamiltonian as Langevin noise, we can assume the variance of the fluctuations to be proportional to the temperature, i.e. $\sigma_\epsilon^2 \propto k_B T$ and $\sigma_{ij}^2 \propto k_B T$. This relation between fluctuations and temperature allows us to construct the time-dependent Hamiltonian at different temperatures without re-running atomistic simulations. Figure 3-5b shows that exciton diffusion coefficient and temperature are positively correlated, in qualitative agreement with earlier theoretical studies using phenomenological models [18, 20] as well as experimental measurements in small organic molecules and conjugated polymer [62, 63]. Without thermal fluctuations, exciton wavefunction would be localized by the static energy disorder leading to a lack of transport in the long time limit. Thermal fluctuations

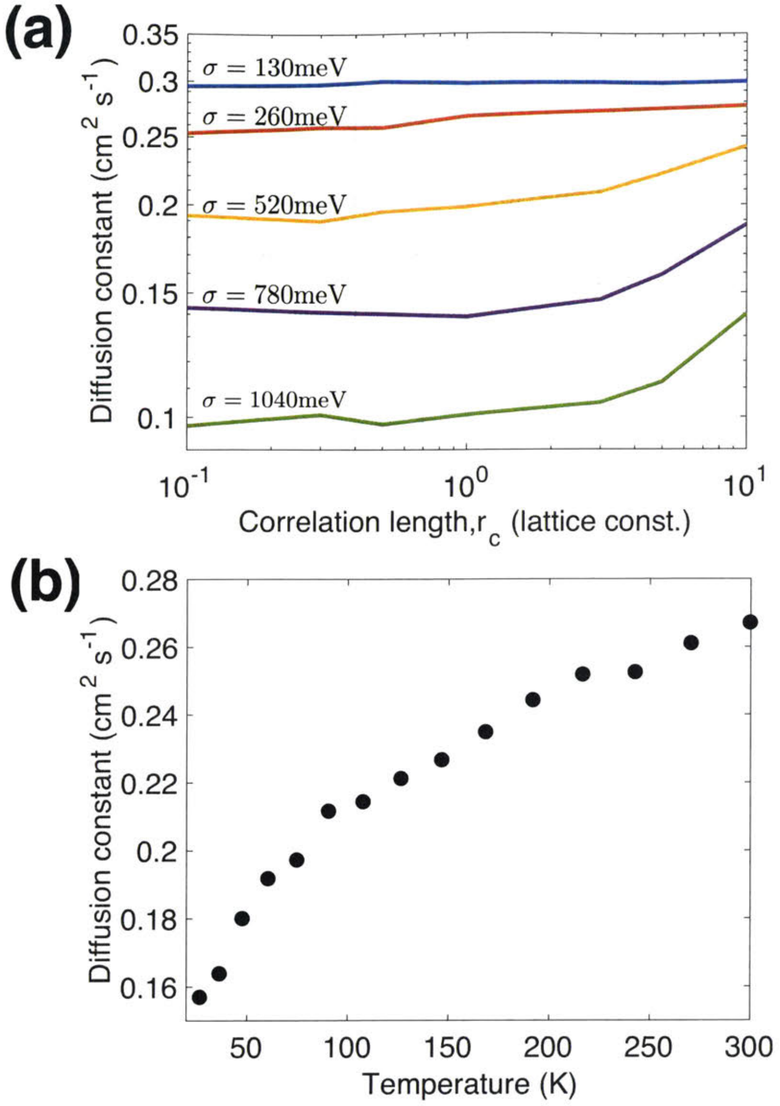

Figure 3-5: Simulation results from a 50 by 50 coarse-grained model. (a) Exciton diffusion constant as a function of r_c at different values of disorder. (b) Exciton diffusion constant as a function of temperature at $r_c = 4.8$Å(one lattice constant) and $\sigma = 260meV$.

overcome the Anderson localization of exciton wavefunction and restore its transport which is proportional to the magnitude of fluctuations. For temperature above $150K$, the exciton diffusion constant is approximately linearly dependent on temperature, a scaling relation consistent with results from fully quantum mechanical treatment of exciton-phonon couplings [64]. The diffusion constant increases by about 20% from $150K$ to $300K$, also in qualitative agreement with experimental measurements of spin-coated conjugated polymer (MDMO-PPV) [62], though some have reported increases as much as $200 - 300\%$ in small organic molecules within the same temperature range [63]. However, experiments also show that the positive correlation between temperature and diffusion coefficient is small for temperature below $150K$, and this low temperature behavior is not captured in our model. Perhaps a more rigorous treatment of the exciton-phonon couplings is required at low temperature when quantum mechanical properties of phonons become important. For example, the exciton-phonon couplings could be treated using open quantum system approach where the phonons are modeled as a bath of quantum harmonic oscillators with spectral density extracted from atomistic simulations.

3.5 Conclusions

To conclude, we develop a computational framework that incorporates the chemical details of molecules into phenomenological tight-binding model. The inclusion of the statistics from electronic structure calculations improves the phenomenological models by injecting the material-specific molecular fingerprint into empirical tight-binding Hamiltonian, partially mitigating the lack of molecular specificity problem in many phenomenological models. Our results with monolayer T6 molecules show that the improved phenomenological model produces exciton dynamics in quantitative agreement with those generated from atomistic simulations, albeit at a much reduced computational cost. We extend this computational framework to study systems of sizes previously unattainable with most quantum chemistry methods, and compare the results with available experimental measurements. The value of the computed 1D diffusion constant is in qualitative agreement with experimental results. Our model predict positive correlation between exciton diffusion constant and temperature which has been observed experimentally in several organic materials. We probe other aspects of the exciton dynamics not directly observable in experiments. Particularly, we show that the spatial correlation in energy disorder can significantly enhance exciton mobility in highly disordered systems, whereas the effect is minimal in systems with small disorder. More importantly, such coarse-graining framework can be easily extended to study other materials and systematically improved by using more sophistical quantum chemistry method in generating the statistics of tight-binding Hamiltonian. Thus our results here could provide a theoretical/computational framework to study exciton dynamics in systems of experimentally relevant sizes and provide guidance in device design.

Chapter 4

A Model of Charge Transfer Exciton: Diffusion, Spin Dynamics and Magnetic Field Effects

4.1 Introduction

Charge transfer (CT) excitons are Coulombically bound electron-hole pairs that are located in spatially separate regions. [65, 66] CT states play a fundamental role in mediating interconversion between bound electronic excitations and free charge carriers in organic electronic materials. For processes that require this interconversion, such as electroluminescence in organic light emitting diodes (OLEDs) and photocurrent generation in organic photovoltaics (OPVs), low-energy (thermalized) CT states are often implicated as a precursor to efficiency loss pathways [65–76]. Despite this, much remains to be understood about the properties of CT states and how they contribute to various energy loss mechanisms. Due to their short lifetime and low optical activity, attempts to interrogate CT states directly have brought limited success. Notably, however, recent experiments that probe CT states indirectly via their response to an applied magnetic field have demonstrated the potential to reveal new information about this elusive class of excited states[77–85]. Unfortunately, extracting this information is challenging because it is encoded by a complex interplay of electronic and nuclear spin dynamics[79, 86, 87]. This interplay is further complicated when the dynamics of the electron-hole spin state (or the specific experimental observable) is coupled to a source of fluctuating microscopic disorder such as charge transport or molecular conformational dynamics[85]. In the following we focus on disentangling this interplay.

The dependence of an experimental observable on an applied magnetic field is generically referred to as the magnetic field effect (MFE). For CT-mediated processes, MFEs require that the observed physical property depends either directly or indirectly on the spin state of the electron-hole pair. For instance, spin selection rules for radiative electron-hole recombination can give rise to a magnetic field-dependent electroluminescence yield [84, 88–90]. To understand specifically how CT state properties are influenced by the presence of a magnetic field it is natural to describe the spin state of the electron-hole pair in a standard basis of singlet and triplet states. If the electron and hole positions are static then MFEs emerge when the Zeeman splitting of the triplet energy levels becomes comparable to or larger than interactions that govern population transfer between the three triplet spin states (i.e., T_-, T_0, and T_+) [85, 86]. Under typical experimental conditions (i.e., applied field strengths $\sim$ 1T) the magnitude of the Zeeman splitting is much smaller than the thermal energy (i.e., $\Delta E_{\text{Zeeman}} \ll k_{\text{B}}T$) and thus it has negligible effect on equilibrium properties. The net result, as illustrated in Figure 4-1a, is that the timescale for spin mixing dynamics is slowed in the presence of a magnetic field.

The microscopic origin of MFEs becomes more complicated if the electron and hole positions are dynamic. This is because variations in electron-hole separation can drive fluctuations in the value of the exchange coupling that determines the energy difference between the singlet and triplet states. This coupling can be large compared to thermal energies but decays exponentially with electron-hole separation. Even subtle changes in CT state configuration can result in significant variations in the equilibrium singlet-triplet ratio. The ability of the CT spin state to respond to these time-dependent variations is mediated by the timescale for spin-mixing dynam-

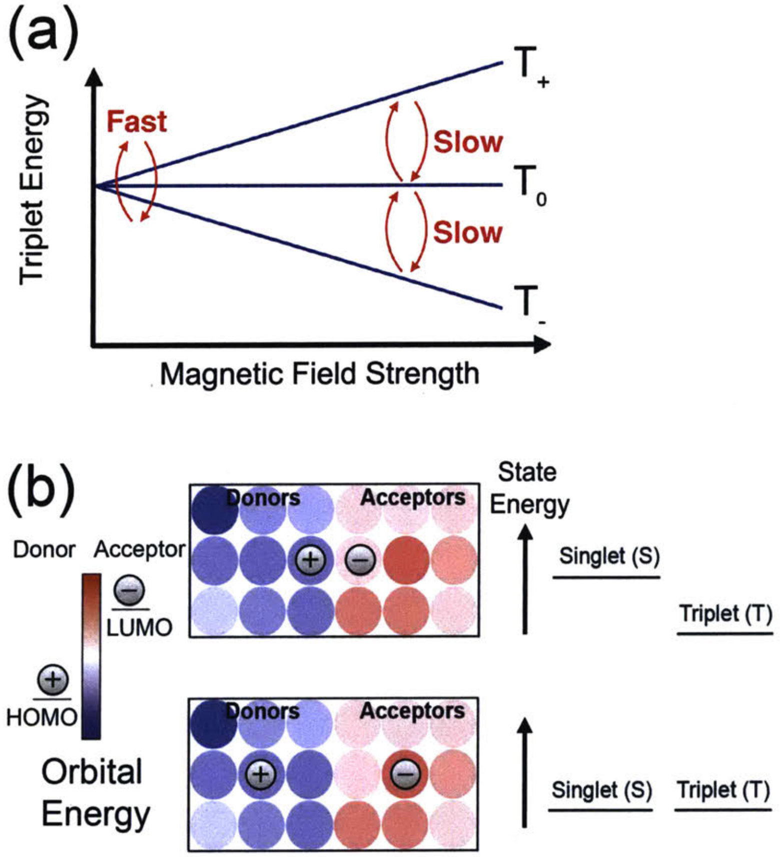
(a)
Triplet Energy
Fast
Slow
Slow
T+
T0
T-
Magnetic Field Strength
(b)
Donor
Acceptor
LUMO
HOMO
Orbital Energy
Donors
Acceptors
State Energy
Singlet (S)
Triplet (T)
Donors
Acceptors
Singlet (S)
Triplet (T)

Figure 4-1: (a) The relative energy of the three, otherwise degenerate, triplet levels are split (Zeeman splitting) by a magnetic field. Consequently, as indicated with red arrows, the timescale for spin mixing dynamics can be varied with an external magnetic field. (b) A schematic depiction of the model system in which donor and acceptor molecules (represented as blue- and red-shaded circles respectively) reside on opposite halves of an ordered lattice. The electron (-) and hole (+) occupy individual molecules whose orbital energies vary as indicated by shading. The relative energy of singlet and triplet states is determined by the exchange splitting, which decays rapidly with electron-hole separation. When the electron and hole occupy neighboring sites (top) this exchange splitting is typically larger than thermal energies. When the electron and hole are separated by one or more molecules (bottom) the exchange splitting is negligible resulting in degenerate singlet and triplet energy levels.

ics, which as described above, can be tuned by the application of an external magnetic field. It is this competition of timescales, between spin and spatial dynamics, that ultimately determines the magnitude of the observed MFEs. Perhaps more importantly though, is that the MFEs encode information that can be used to characterize the microscopic dynamics of the electron-hole pair.

In this chapter we address the challenge of predicting and interpreting the results of magnetic field sensitive experiments by utilizing numerical simulation. We present a model for CT state dynamics that incorporates magnetic field dependent spin dynamics into an efficient coarse-grained description of electron-hole transport. We demonstrate that this model is capable of reproducing experimental results and revealing fundamental aspects of CT state dynamics that are otherwise inaccessible to current experimental techniques. First, however, we describe the general theoretical framework that underlies our model for simulating CT state dynamics in disordered molecular systems.

4.2 Model

In our model a CT state is described as an oppositely charged pair of spin-1/2 particles (i.e., an electron and hole), each localized on separate molecules. We utilize a coarse-grained description of a molecular semiconductor in which individual molecules are represented as discrete sites. Each molecular site is characterized by a position, $\vec{r}_i$, HOMO energy, $E_i^{(\mathrm{HOMO})}$, LUMO energy, $E_i^{(\mathrm{LUMO})}$, and a hyperfine magnetic field, $\vec{B}_i^{(\mathrm{hf})}$, which arises from the interaction of the electronic magnetic moment with the nuclear magnetic moment. CT state properties are determined by combining these parameters, for the electron- and hole-occupied sites, with a description of the electron-hole spin state, which we represent in terms of a two-spin quantum density matrix, ρ. The energy of a CT state configuration in which the electron occupies site i and the hole occupies site j is given by

$$E_{ij}^{(\mathrm{CT})}(\rho) = E_{ij}^{(\mathrm{E})} + E_{ij}^{(\mathrm{S})}(\rho), \tag{4.1}$$

where $E_{ij}^{(\mathrm{E})}$ is the electronic energy and $E_{ij}^{(\mathrm{S})}(\rho)$ is the spin energy. The electronic energy, which depends on the spatial configuration of the electron-hole pair, is given by

$$E_{ij}^{(\mathrm{E})} = E_i^{(\mathrm{LUMO})} - E_j^{(\mathrm{HOMO})} - \frac{e^2}{4\pi\epsilon|\vec{r}_i - \vec{r}_j|}, \tag{4.2}$$

where e is the elementary unit of charge, and ϵ is the dielectric constant. In this expression the first two terms represent the vertical excitation energy (i.e., the HOMO-LUMO gap) of the given CT state and the final term describes the electrostatic electron-hole attraction[91]. The spin energy is given by $E_{ij}^{(\mathrm{S})} = \mathrm{Tr}[H_{ij}^{(\mathrm{S})}\rho]$, where $H_{ij}^{(\mathrm{S})}$ is the spin Hamiltonian,

$$H_{ij}^{(\mathrm{S})} = g\mu_b\Big[(\vec{S}_e + \vec{S}_h)\cdot\vec{B}^{(\mathrm{app})} + \vec{S}_e\cdot\vec{B}_i^{(\mathrm{hf})} + \vec{S}_h\cdot\vec{B}_j^{(\mathrm{hf})}\Big] - J(|\vec{r}_i - \vec{r}_j|)\vec{S}_e\cdot\vec{S}_h, \tag{4.3}$$

where μ_b is the Bohr magneton, and g is the g-factor for the magnetic moment, $\vec{S}_e$ and $\vec{S}_h$ are the spin operators for the electron and hole respectively. The terms in the square brackets describe the interaction of the electron and hole spins with the applied magnetic field and the local hyperfine field, denoted as $\vec{B}^{(\mathrm{app})}$ and $\vec{B}_i^{(\mathrm{hf})}$ respectively. To model the hyperfine interaction with the nuclear spins we adopt the semiclassical approach of Schulten and Wolynes, in which hyperfine interactions are approximated to be static and site dependent, with $\vec{B}_i^{(\mathrm{hf})}$ drawn randomly from the three-dimensional Gaussian distribution[92, 93]. The final term in Eq. 4.3 describes the exchange interaction between the electron and hole spins, where $J(r)$ is the exchange coupling, which depends on the electron-hole separation, $r = |\vec{r}_i - \vec{r}_j|$.

The time evolution of our model is separated into a spatial part, which describes the dynamics of electron and hole positions, and a spin part, which describes the time evolution of the CT spin density matrix. The dynamics of electron and hole positions are determined by a kinetic Monte Carlo (KMC) algorithm [94], whereby the electron and hole migrate via stochastic hops between neighboring molecular sites. We restrict the dynamics to include only single particle hops (i.e., electron or hole) and assign hopping rates following the Miller-Abrahams formula [95]. As such, the rate for an electron to hop from site i to site i' while the hole is fixed at site j is given by

$$k_{ij\to i'j} = \nu_0 \exp\left[-\frac{(\Delta E_{ij\to i'j} + |\Delta E_{ij\to i'j}|)}{2k_{\mathrm{B}}T}\right], \tag{4.4}$$

where ν_0 is the normalized hopping frequency, $k_\mathrm{B}T$ is the Boltzmann constant times temperature, and $\Delta E_{ij\to i'j} = E^{(\mathrm{CT})}_{i'j} - E^{(\mathrm{CT})}_{ij}$. The hole hopping rate $k_{ij\to ij'}$ is given by an analogous formula.

The spin dynamics are modeled with an open quantum systems approach in which the electron-hole spin state, $\rho(t)$, is coupled to a bath of harmonic oscillators and propagated via a secular Redfield equation [96] (details in the next subsection). The spin Hamiltonian in Eq. 4.3 depends on CT state configuration and therefore the stochastic spatial dynamics of the electron-hole pair imparts a time dependence to the spin Hamiltonian. In between charge hopping events, however, the electron and hole positions are assumed to be fixed and thus the Hamiltonian of Eq. 4.3 is static.

We model the exchange coupling as a step function with the form,

$$J(|\vec{r}_i - \vec{r}_j|) = \begin{cases} J_0, & \text{if } i \text{ and } j \text{ are nearest neighbors (i.e., the bound CT state),} \\ 0, & \text{otherwise (i.e., the unbound CT state).} \end{cases} \tag{4.5}$$

We estimate $J_0 = 50\mathrm{meV}$ based on the experimental data [83, 97]. The standard KMC algorithm was modified to include the ability for the electron and hole to radiatively recombine. This recombination can only occur when the electron and hole reside on neighboring interfacial molecules, and the probability of recombination is proportional to the singlet density. Formally, this conditional relaxation pathway can be expressed in terms of a KMC processes with a rate,

$$k^{(\mathrm{PL})}_{ij} = \begin{cases} k_\mathrm{PL}, & \text{if } i \text{ and } j \text{ are nearest neighbors,} \\ 0, & \text{otherwise,} \end{cases} \tag{4.6}$$

where the dependence of the photoluminescence rate on spin state is described by treating k_PL as a stochastic random variable with the properties,

$$k_\mathrm{PL} = \begin{cases} \tau_\mathrm{PL}^{-1}, & \text{with probability } \rho_\mathrm{S}, \\ 0, & \text{with probability } 1 - \rho_\mathrm{S}. \end{cases} \tag{4.7}$$

Here ρ_S represents the singlet projection of the two-spin quantum density matrix, ρ.

The KMC parameters, $\nu_0 = 15\mu\text{s}^{-1}$ and $\tau_{\text{PL}} = 8\mu\text{s}^{-1}$, where chosen based on transient photoluminescence measurements [83].

4.2.1 Open Quantum System Approach to Spin Dynamics

We use the standard open quantum system approach to describe the spin dynamics and relaxation. The total system and bath Hamiltonian is given by

$$H^{(\text{Tot})} = H^{(\text{S})} + H^{(\text{B})} + H^{(\text{SB})}, \tag{4.8}$$

where the three terms represent the Hamiltonians of the system, the bath, and system-bath coupling, respectively. The system Hamiltonian, $H^{(\text{S})}$, is described by the electron (indexed e) and hole (indexed h) spin operators and its explicit form is given in Eq. 4.3. We assume that the electron and hole are independently coupled to its own harmonic bath, thus

$$\begin{aligned} H^{(\text{B})} &= \sum_{\alpha=e,h} \sum_{n} \omega_\alpha^{(n)} b_\alpha^{(n)\dagger} b_\alpha^{(n)}, && (4.9) \\ H^{(\text{SB})} &= \sum_{\alpha=e,h} \sum_{n} g_\alpha^{(n)} S_\alpha^z (b_\alpha^{\dagger(n)} + b_\alpha^{(n)}), && (4.10) \end{aligned}$$

where $\omega_\alpha^{(n)}$ and $b_\alpha^{(n)\dagger}(b_\alpha^{(n)})$ are the frequency and the creation (annihilation) operator of the n-th mode of the harmonic bath coupled to electron or hole with coupling strength $g_\alpha^{(n)}$, respectively. We assume the coupling constants are identical for both the electron and hole, i.e. $g_\alpha^{(n)} = g^{(n)}$. Additionally, we choose a Drude-Lorentz spectral density, $J(\omega) = \frac{\pi}{2}\sum_n \frac{|g^{(n)}|^2}{\omega_n}\delta(\omega - \omega_n) = 2\gamma\omega_c\frac{\omega}{\omega^2+\omega_c^2}$, where γ is the dissipation strength and ω_c is the cut-off frequency.

A perturbation approximation can be applied in terms of the system-bath coupling leading to a standard Redfield quantum master equation of the reduced density matrix [98, 99]:

$$\frac{d\rho_{\mu\nu}(t)}{dt} = -i\,\omega_{\nu\mu}\rho_{\mu\nu}(t) + \sum_{\mu'\nu'} R_{\mu\nu,\mu'\nu'}\rho_{\mu'\nu'}(t), \tag{4.11}$$

where the Markovian approximation has been employed. The Greek indices denote the eigenstates of the system Hamiltonian, i.e. $H^{(\mathrm{s})}|\mu\rangle = E_\mu|\mu\rangle$ and $\omega_{\mu\nu} = (E_\mu - E_\nu)/\hbar$. The Redfield tensor, $R_{\mu\nu,\mu'\nu'}$, describes the spin relaxation and can be expressed as

$$R_{\mu\nu,\mu'\nu'} = \Gamma_{\nu'\nu,\mu\mu'} + \Gamma^*_{\mu'\mu,\nu\nu'} - \delta_{\nu\nu'}\sum_\kappa \Gamma_{\mu\kappa,\kappa\mu'} - \delta_{\mu\mu'}\sum_\kappa \Gamma^*_{\nu\kappa,\kappa\nu'}; \tag{4.12}$$

$$\Gamma_{\mu\nu,\mu'\nu'} = \sum_{\alpha=e,h} \langle\mu|S^z_\alpha|\nu\rangle\langle\mu'|S^z_\alpha|\nu'\rangle K(\omega_{\nu'\mu'})\ , \tag{4.13}$$

where $K(\omega)$ is the half-Fourier transform of the phonon bath correlation function

$$K(\omega) = \int_0^\infty \frac{d\omega}{\pi} J(\omega)\Big[\coth\Big(\hbar\beta\omega/2\Big)\cos(\omega t) - i\sin(\omega t)\Big], \tag{4.14}$$

where $\beta = \frac{1}{k_B T}$ is the inverse thermal energy. Finally, we invoke the secular approximation, dropping the terms in the Redfield tensor, $R_{\mu\nu,\mu'\nu'}$, for which $\omega_{\mu\nu} - \omega_{\mu'\nu'} \neq 0$. Employing the secular approximation ensures the positivity of the reduced density matrix, i.e. the diagonal matrix elements are always positive [96, 100]. In addition to preserving positivity, the secular approximation also guarantees the long-time equilibrium state is given by the Boltzmann state of the system Hamiltonian, $\rho(t \to \infty) = \frac{\mathrm{e}^{-\beta H^{(\mathrm{s})}}}{\mathrm{tr}[\mathrm{e}^{-\beta H^{(\mathrm{s})}}]}$. Here we use $\omega_c = 0.004$meV and $\gamma = 3\times10^{-8}$meV. The hyperfine magnetic field, $\vec{B}^{(\mathrm{hf})}$, is drawn from a 3D Gaussian distribution with a standard deviation of 1mT.

4.2.2 Parametrization of the Model

The empirical model parameters that define the coarse-grained system can be assigned in a variety of ways. For instance they can be inferred through the analysis of experimental data or computed via *ab-initio* molecular simulation. The ability to vary these parameters in order to describe different materials provides the versatility to adapt this model to describe the broad range of systems that exhibit MFEs. We now demonstrate this versatility by applying our model to investigate a recent set of

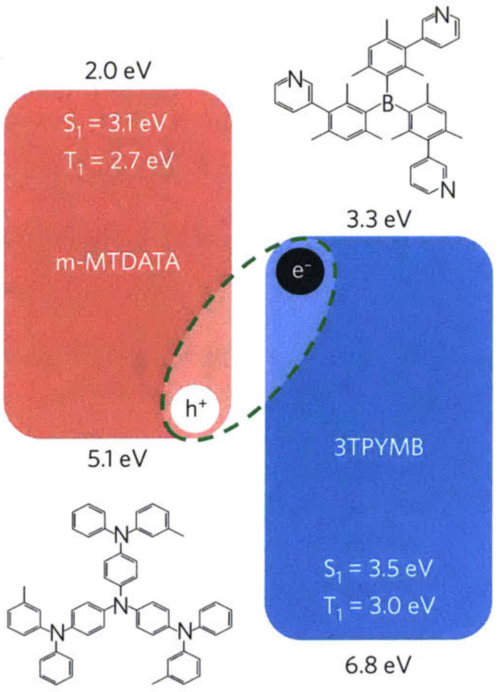

Figure 4-2: Energy diagram and chemical structures of the donor-acceptor material system. The energy levels and the HOMO and LUMO are in eV and are referenced to the vacuum. The energies in eV of the lowest singlet (S_1) and triplet (T_1) excitons of m-MTDATA and 3TPYMB are also indicated. Figure reproduced from Ref. [83]

magnetic field dependent experiments aimed at probing CT-state dynamics.

Recently, Adachi *et al.*[97] and Baldo *et al*[82, 83] have developed a donor-acceptor pair of organic dye molecules, 4,4′,4″-tris[3-methylphenyl(phenyl)amino]-triphenylamine (m-MTDATA) and tris-[3-(3-pyridyl)-mesityl]borane (3TPYMB), which can support electronically excited CT states that can undergo direct singlet radiative recombination (see Figure 4-2). For thin films blends of these molecules this radiative processes is evident in the photoluminescence (PL), which exhibits a long time ($\sim 30\mu$s) decay that has been attributed to reverse intersystem crossing from a long lived population of CT triplets. Focusing on this long time PL signature, time-resolved fluorescence microscopy has revealed that the PL profile undergoes both a transient spatial broadening and a transient redshift[83], indicating that CT states are mobile along the donor-acceptor interface and sensitive to the presence of static energetic disorder. The PL also exhibits pronounced MFEs, indicating that CT state dynamics may involve fluctuations in electron-hole separation. These observations led the authors to hypothesize that CT dynamics proceed through the asynchronous motion of localized electrons and holes[83]. Here we apply our model to this system in order to (*i*) confirm that the hypothesized description of CT state dynamics is consistent with the observed MFEs, and (*ii*) to elaborate on the role of spin dynamics in charge-transfer mediated processes such as photocurrent generation and photoluminescence.

To adapt our model to this system we utilized a parameterization that was based only on experimentally available data. The model system included a regular lattice of molecular sites where the lattice spacing was based on the average excluded volume size of the constituent molecules. As illustrated in Figure 4-1b, the system was divided so that one half of the system contains only donor molecules and the other half contains only acceptor molecules. Our lattice model comprises 300 donor sites and 300 acceptor sites, divided by a linear donor-acceptor interface of 20 interfacial donor-acceptor pairs. The lattice spacing is chosen to be 2.5 nm, roughly approximating the excluded-volume diameter of the molecules in the experiment. We assumed the presence of uncorrelated static energetic disorder, which was represented by assigning values of $E_i^{\text{(LUMO)}}$ and $E_j^{\text{(HOMO)}}$ randomly from a Gaussian distribution with standard deviation inferred from spectroscopy. We use $E_j^{\text{(HOMO)}} = 5.1eV$ and $E_j^{\text{(LUMO)}} = 3.3eV$ for the average HOMO energy of donor molecules and LUMO energy of acceptor molecules, respectively. Both energies are assigned Gaussian disorders with standard deviation of 60meV to describe the inhomogeneous broadening. Experimental data was also used to parameterize the exchange coupling, radiative recombination rate, and the details of spin dynamics.

4.3 Results and Discussions

4.3.1 Comparison with Experiments

To simulate CT state PL we generated trajectories that were initiated in a pure singlet state with the electron and hole on adjacent sites at the donor-acceptor interface. We generated statistics by sampling many trajectories across many realizations of the static disorder. Individual trajectories were carried out for a finite observation time ($\tau_{\text{obs}} = 30\mu s$) which was chosen to be approximately the experimental time window in Ref. [83], however trajectories could also be terminated at earlier times via a radiative recombination event. We modeled radiative recombination as a stochastic event with a rate that was proportional to the singlet population and was only allowed if the electron and hole occupied adjacent interfacial sites.

We simulated transient PL by analyzing the energies and positions of the ensemble of CT states that underwent radiative recombination. We find that our model is capable of reproducing the experimentally obtained transient PL data (i.e., spatial broadening and redshift) with near perfect agreement. In the following we first present direct comparisons of our simulation data to these experimental results in the next paragraph. Then we narrow our discussion to focus on the unique capability of this model to reveal the effect of applied magnetic field on CT state dynamics.

We compute the transient PL decay by counting the number of recombined CT excitons per unit time in the KMC simulations. The comparison with experimental data from Ref. 83, plotted in Figure 4-3a, allows us to estimate the singlet decay rate, k_{PL}. In our simulations, the displacement of a CT exciton is defined as the distance between the initial CT state and the eventual recombination site along the interface. With this definition, the mean squared displacement from the KMC simulations and the experimental data are plotted in Figure 4-3b. The increase in mean squared displacement indicates that the CT excitons can move geminately over distance of several molecules (5-10nm). By computing the averaged energy of the recombined CT excitons, see Eq. 4.1 , our model is capable of reproducing the time dependence of the CT exciton emission wavelength. The comparison between the simulated and experimental CT exciton energy is plotted in Figure 4-3c. The redshift of the emission wavelength indicates the preference of the electron and hole to diffuse to lower-energy interfacial sites, and therefore a manifestation of nanoscale disorder at the interface. The results presented here were generated using a two-dimensional donor-acceptor system, such as illustrated in Figure 4-1. We also explored three-dimensional systems and found results to be similar in both two and three dimensions. The biggest qualitative difference between these two cases appears in the early time relaxation (i.e., the first 5 μs), where transient spatial broadening of the PL data (and the associated transient red shift) exhibits more rapid change in the three- dimensional system. This initial relaxation is particularly sensitive to the number of nearest neighbors (i.e., the coordination number) within the lattice. By comparing simulation data from both two-dimensional and three-dimensional systems, we find that the two-dimensional systems actually result in better quantitative agreement with experiment. This perhaps suggests that the three-dimensional interfacial morphology of the experimental materials features coordination numbers that are more similar to that of our two-dimensional model system.

In the results presented in Ref. [83] MFEs were quantified in terms of the field dependence of the integrated PL and photocurrent. We compute integrated PL by first generating an ensemble of trajectories at a given value of $B = |\vec{B}^{(\mathrm{app})}|$ and then evaluating the fraction of trajectories that terminate due to radiative recombination. Similarly, we relate integrated photocurrent to internal quantum efficiency (IQE) which is evaluated by computing the fraction of trajectories for which the electron-hole separation at $t = \tau_{\mathrm{obs}}$ exceeds the Coulomb radius (i.e., the distance at which the electrostatic electron-hole interaction is equal to the thermal energy, $k_{\mathrm{B}}T$). Since our model does not include non-radiative loss mechanisms we expect our simulated values to be overestimated relative to experiment. We have accounted for these unknown loss mechanisms by scaling our results by a field-independent constant.

Figure 4-3d contains a plot of the percent change in integrated PL and photocurrent as measured experimentally (solid lines) and as predicted from our simulation data (open circles). Experiments yield an increase in PL with the application of a magnetic field that saturates at fields approaching 0.5T. There is a corresponding decrease in the integrated photocurrent (more fluorescing CT states leaves fewer free charge carriers for photocurrent generation). The simulated CT dynamics accurately reproduce the shape of the experimentally measured MFEs in both the integrated PL and the photocurrent. The ability of our model to reproduce both the experimentally

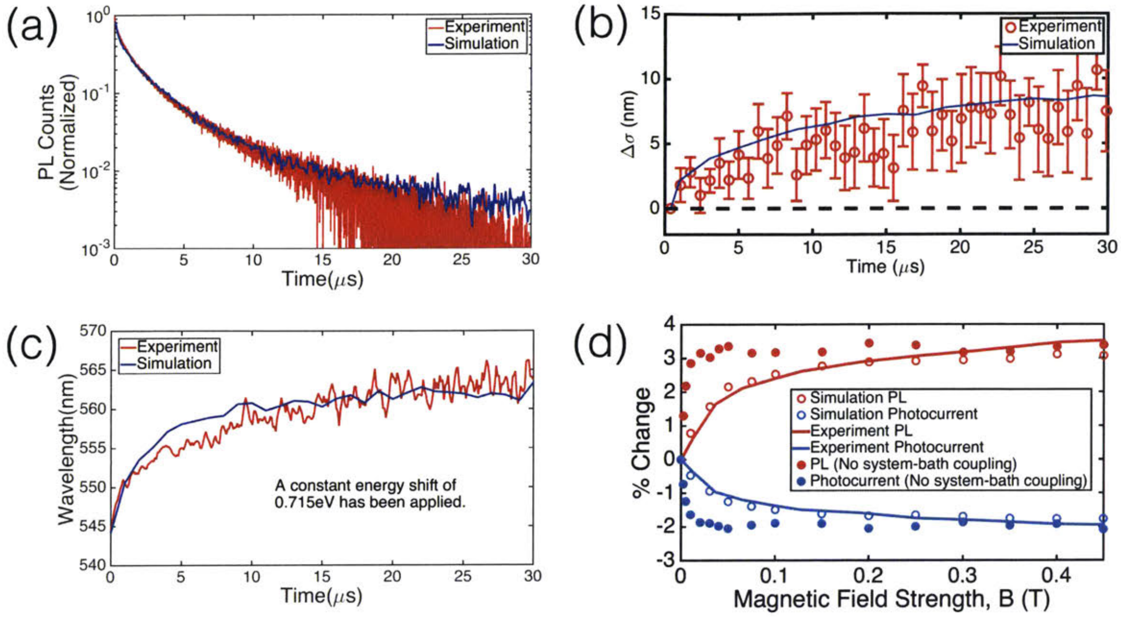

Figure 4-3: (a) The simulated (blue) and experimental (red) transient decay of photoluminescence (normalized). (b) The centroid of the experimental data (red) is compared to the spectral shift predicted by the kinetic Monte Carlo simulation (blue). The transient redshift of the CT exciton emission wavelength indicates the CT excitons travel to lower energy sides. (c) The simulated mean squared displacement of CT excitons (blue). The red circles show the experimental values of the standard deviation of spatial broadening Gaussian function of PL. The error bars indicate the standard error between four independent diffusing imaging measurements [83]. (d) The magnetic field dependence of photoluminescence (PL) and photocurrent as determined experimentally (solid lines) and simulated with our model (unfilled circles). The quantity plotted against the y-axis is the percentage change, measured relative to the case where $B = 0$. Filled circles correspond to simulated results in the absence of system-bath coupling for spin dynamics.

obtained transient PL and MFEs indicates that our theoretical framework accurately captures the basic physics associated with CT state dynamics in this system. Building up on this validation we now turn our attention to the ability of this model to reveal information about CT dynamics that are experimentally unavailable.

4.3.2 Singlet-Triplet Population Transfer Analysis

To begin we consider the physical origins of singlet-triplet population transfer. For CT states in systems composed of light molecules (e.g., in the absence of spin-orbit coupling) it is often assumed that this intersystem crossing is driven only by the hyperfine coupling [80, 81, 92, 101, 102]. However, our simulation results reveal that there are alternative spin relaxation pathways that play a significant role in facilitating spin mixing dynamics. These spin relaxation pathways are described implicitly in our model in terms of a system-bath coupling in the Redfield relaxation tensor. This coupling drives the so-called "spin-flip" transition, mediating population transfer specifically between the singlet and the T_0 triplet state [86]. If we silence this coupling, then the relatively weak hyperfine field ($\sim$ 1mT) is easily overcome by an externally applied field, leading to MFEs that saturate at very small fields. This is illustrated (filled circles) in Figure 4-3d, where the absence of this system-bath coupling results in MFEs that rise sharply and saturate at around $B = 10 - 20$mT, in qualitative disagreement with experimental observations.

Using our model we can explore the microscopic fluctuations that give rise to MFEs. To illustrate this we consider two representative trajectories each generated at different values of B, but exhibiting similar spatial dynamics. As illustrated in Figure 4-4a, the trajectories include three distinct segments: First, in segment A, the electron-hole pair is initiated as singlet state on neighboring sites along the interface. Next, in segment B, the electron hops away from the interface to form an unbound CT state with a concomitant reduction in the exchange coupling. Finally, in segment C, the electron and hole reunite on neighboring interfacial sites prior to undergoing radiative recombination. Although the spatial dynamics of these two trajectories are similar, due to the differing applied magnetic field their spin dynamics differ significantly. In order to appreciate these differences we consider each trajectory separately, starting with the $B = 0$ case (green line in Figure 4-4a).

The trajectory is initialized as a bound CT state with an interfacial exchange splitting of 50meV that lowers the triplet state energy relative to that of the singlet state. This energy difference favors the formation of triplet states, with a Boltzmann-weighted singlet density of $\langle \rho_S \rangle \approx 0.05$. The evolution of the spin state from the initial singlet state is mediated primarily by the system-bath coupling, with a characteristic relaxation timescale of approximately 40ns. Before the spin state can fully

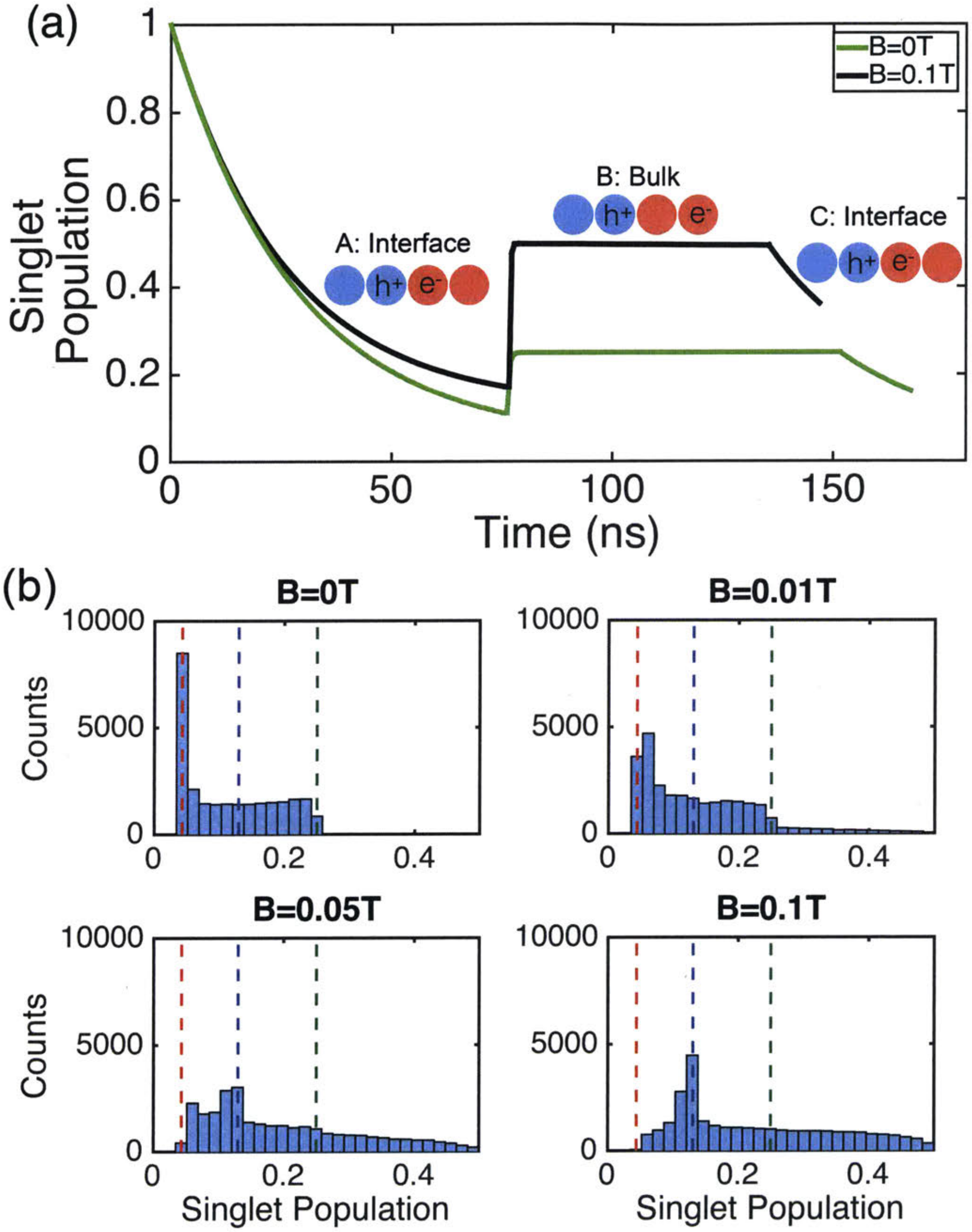

Figure 4-4: (a) The time-dependence of the singlet population for two typical trajectories, selected to exhibit similar spatial dynamics, carried out under different values of $B = |\vec{B}^{\text{app}}|$. The inset illustrates the hopping behavior of these trajectories, which each ends abruptly with a radiative recombination event. (b) The distribution of the values of singlet population, ρ_{S}, at the recombination time for trajectories generated at different values of applied magnetic field. The red- and green-dashed vertical lines represent the equilibrium values for the bound ($\langle \rho_{\text{S}} \rangle = 0.05$) and unbound ($\langle \rho_{\text{S}} \rangle = 0.25$) CT states respectively. The blue-dashed line represents the value of ρ_{S} for the bound CT state in two-state quasi-equilibrium.

relax, however, the system enters segment B by hopping into an unbound CT state configuration. In our model any unbound state is free of exchange coupling and thus the singlet and triplet states are degenerate. The associated equilibrium singlet density for the unbound state is $\langle \rho_S \rangle = 0.25$. The spin relaxation for this degenerate unbound state is ultrafast, as evident in the rapid equilibration of the singlet population in Figure 4-4a. In segment C the CT state re-enters the bound state and proceeds again toward the bound singlet density of $\langle \rho_S \rangle \approx 0.05$. During this equilibration the CT state undergoes a radiative recombination event, signaling the termination of the trajectory.

For the trajectory generated with $B = 0.1\text{T}$ (black line in Figure 4-4a) the effect of CT configuration on the equilibrium $\langle \rho_S \rangle$ is identical. The ability of the spin state to respond to changes in configuration, however, is significantly affected by the presence of the applied magnetic field. At $B = 0.1\text{T}$ the intra-triplet relaxation occurs on timescales much longer than the length of the trajectory. Due to this separation in timescales the spin dynamics of this trajectory can be understood in terms of a quasi-equilibrium between the S and T_0 states. Under this two-state quasi-equilibrium the bound state singlet population approaches $\rho_{\text{S}} = 0.13$ and the unbound state approaches $\rho_{\text{S}} = 0.5$. The field-induced slowing of intra-triplet spin relaxation therefore has the effect of both prolonging the redistribution of initial singlet population and, perhaps more importantly, of amplifying the effect of fluctuations in electron-hole separation on the transient singlet population.

The qualitative insight generated by analyzing individual trajectories can be further supported through the statistical analysis of many trajectories. Figure 4-4b contains histograms that reveal the distribution of singlet density, ρ_{S}, amongst the population of fluorescing CT states. Each of the four histograms depicted in Figure 4-4b was generated under different values of B. For the case of $B = 0$, the distribution is peaked around $\rho_{\text{S}} = 0.05$ (red dashed line) corresponding to the equilibrium $\langle \rho_S \rangle$ for the bound CT state. The distribution also includes a tail that extends to $\rho_{\text{S}} = 0.25$ (green dashed line), reflecting the population of CT states that fluoresce shortly after re-entering the bound state, before fully equilibrating. This shows that even in the

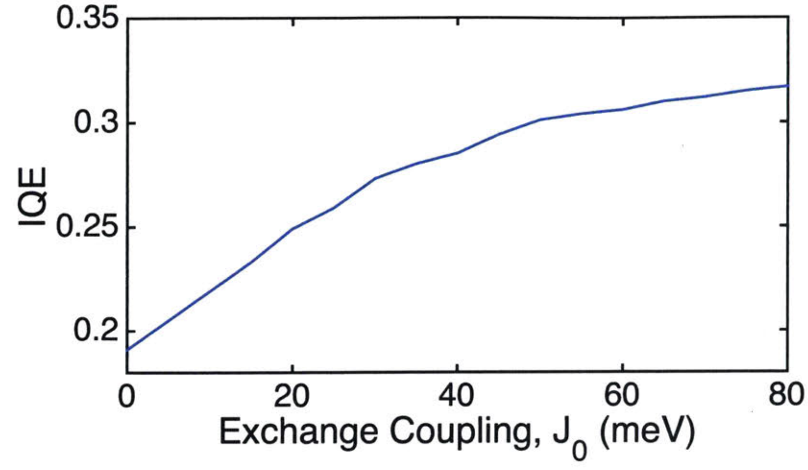

Figure 4-5: The dependence of photovoltaic IQE on the magnitude of the interfacial exchange splitting as predicted from simulations carried out on our model system.

absence of an applied magnetic field a significant portion of luminescent CT excitons exhibit non-equilibrium spin statistics that result directly from fluctuations in electron-hole separation. As B increases the shape of the histograms change to reflect two-state (S and T_0) quasi equilibrium, with peak at $\rho_S = 0.13$ (blue dashed line), that results from field-induced slowing of spin mixing dynamics. The field-dependence of these histograms highlight the microscopic origin of observed MFEs, namely that field-induced non-equilibrium spin statistics serve to enhance the singlet population and thereby the PL yields.

4.3.3 Effect of Exchange Coupling

The analysis described above clearly demonstrates the importance of the time dependent exchange splitting on the spin dynamics. With our model we can evaluate the role of this interfacial exchange splitting, J_0, on predicted device performance. To do this we have carried out a series of simulations each with varying values of J_0. Our findings, shown in Figure 4-5, illustrate that larger J_0 is beneficial for OPV performance. Specifically, as J_0 increases from 0meV to 80meV, the simulated IQE increases by nearly 70%. Qualitatively, this efficiency increase arises because energetically favorable triplet states are spin protected from radiative recombination and thus the electron and hole have more time to diffuse away from each other to generate free charges. By initiating CT states as spin-equilibrated free charges at the simulation boundary our model can be utilized to simulate electroluminescence. Increasing exchange coupling was found to reduce electroluminescence efficiency, which is consistent with experimental observations reported in Ref. [103].

4.4 Conclusions

The model presented here offers an efficient and versatile tool that can be used to relate difficult to interpret magnetic field sensitive experiments to the microscopic fluctuations of excited electron-hole pairs. By applying this model to the donor-acceptor blend described in Ref. [83] we have highlighted how MFEs emerge from the details of spin mixing dynamics. Furthermore, we have illustrated how the interplay between spin and spatial dynamics contribute to CT state dynamics and experimentally observed MFEs. The insight we have drawn highlights the benefit of simple models in guiding our intuition around complex physical systems. This model can be applied in a straightforward manner to describe the optoelectronic properties of other CT-mediated processes, perhaps those that involve more complicated interfacial molecular morphology.

Chapter 5

The Non-equilibrium Effect of Interfacial Charge Transfer Exciton Dissociation

5.1 Introduction

The dissociation of Coulombically bound excited electron-hole pairs – excitons – into free charge carriers is a microscopic process that is fundamental to the performance of photovoltaic systems.[66, 72, 76] This process requires the physical separation of oppositely charged electrons and holes, which are initially held together by an attractive electrostatic force. The energy required to overcome this force and produce independent charge carriers is known as the exciton binding energy. For inorganic-based photovoltaic materials, the binding energy is generally small and easily overcome, however, for organic-based photovoltaics (OPVs) the exciton binding energy can significantly exceed thermal energies. The inability of bound charges to overcome this large binding energy has been implicated as a primary source of efficiency loss in OPVs.[66, 69–72, 76] Many efforts to improve OPV efficiency have thus aimed to extend exciton lifetimes and enhance charge carrier mobilities by eliminating sources of microscopic disorder within the active material.[6, 104, 105] Furthermore, microscopic disorder has been implicated in the reduction of open-circuit voltage due to internal electronic thermalization. [106] It has been revealed, however, that the general strategy of eliminating microscopic disorder can have unintended negative effects on photovoltaic efficiency.[107–111] Here we explore the microscopic origins of this effect and demonstrate that the presence of molecular disorder can enhance exciton dissociation yields by giving rise to dissociation pathways that are downhill in energy and thus mitigate the effects of the exciton binding energy. Using a simple model of exciton dynamics we show that when disorder is present electrons and holes are driven apart along these energetically favorable pathways. We highlight that this effect is driven by the dissipation of excess electronic energy and is therefore determined by the nonequilibrium dynamics of the electron-hole pair. Our results provide new physical insight into the importance of treating nonequilibrium effects in models of charge and energy transport.

In OPV materials exciton dissociation is facilitated by donor-acceptor interfaces, where energetic offsets in the molecular orbital energies of donor and acceptor molecules provide a driving force for exciton dissociation. This driving force favors the formation of partially dissociated charge-transfer (CT) states, where the electron and hole reside on adjacent acceptor and donor molecules respectively. These *bound* CT states are further stabilized by the electrostatic attraction of the oppositely charged electron and hole, which is typically about 0.4 eV ($\sim 10k_{\mathrm{B}}T$ at room temperature), and this strong Coulombic stabilization causes the bound CT state to lie at a minimum of the excited state potential energy surface.[112–114] CT states that reside within this minimum are prone to recombination on timescales that are much shorter those required for the electron-hole pair to diffusively overcome the exciton binding energy. Based on the Onsager model[115] the dissociation probability for a bound CT state at a typical organic donor-acceptor interface is approximately $P_{\mathrm{dis}} \sim 10^{-3}$. [1] Despite this exceedingly small prediction, the highest performing organic solar cells have been observed to operate with the internal quantum efficiency of near 100%,[116] indicating that free change carriers escape this minimum with near unit efficiency. Reconciling the apparent inconsistency between the predicted and observed recombination losses has been a longstanding challenge in the field of organic electronics.

---

[1] At 300K the dissociation probability predicted by the Onsager model is approximately given by $P \approx \exp(-r_{\mathrm{C}}/a)$, where r_{C} is the Coulomb capture radius (taken here to be $r_{\mathrm{C}} \approx 15$nm) and a is the initial electron-hole separation (taken here to be $a \approx 2.5$nm).

Many studies, both experimental and theoretical, have been aimed at investigating how electron-hole pairs escape, or otherwise avoid, the trap-like bound CT state.[73–75, 107, 111, 113, 117–127] Numerous plausible explanations have emerged from these efforts. Experiments show that for some systems successful dissociation pathways avoid the lowest energy CT intermediates by traversing a non-thermalized manifold of high-energy, often delocalized, electronic states.[74, 122] In other systems it has been shown that these so-called hot CT states are not necessary for dissociation and that free carriers can emerge from populations of electronically thermalized low-energy CT states.[75, 118, 123] The microscopic mechanism underlying this *cold* CT exciton dissociation process remains a topic of scientific debate and is the focus of the work presented here.

Previous studies have identified various physical driving forces that may contribute favorably to the process of cold CT exciton dissociation. This includes those arising from entropic effects, the presence of static interfacial electric fields, interfacial gradients in molecular excitation energies, and delocalized free carrier wave functions.[75, 111, 113, 118–121, 123, 124, 126, 127] These contributions, and others, are generally sensitive to the presence of random molecular disorder, which can affect the inter- and intra-molecular electronic structure, leading to spatial variations in the energetic properties of excitons and free charge carriers. Such disorder is common in organic electronic materials, however, its effect on the microscopic dynamics of electrons and holes is yet to be fully appreciated. Recently it has been found that the presence of random energetic disorder can both reduce the free energy barrier and enhance the thermodynamic driving force for exciton dissociation.[110, 111, 119] Here we expand upon this finding by exploring the effect of random energetic disorder on the microscopic dynamics of exciton dissociation. By doing so we reveal that when disorder is present dissociation occurs primarily along nonequilibrium pathways and thus it cannot be properly understood in terms of thermodynamics alone.

Spatial variations in the energy landscape influence the dynamics of excitons and free charge carriers by biasing their motion along energetic gradients toward regions that permit the population of lower energy excited states. In time-resolved fluorescence microscopy this effect manifests as a concerted red-shift and spatial broadening of the photoluminescence profile.[83, 128] In some cases spatial energetic variations can stabilize states that would be unfavorable within a perfectly ordered system. For instance, at a donor-acceptor interface this effect can stabilize the formation of CT states with increased electron-hole separation, thereby facilitating the nascent stages of exciton dissociation. As we demonstrate, this stabilization has a positive effect on the dissociation process that increases with disorder but also competes with a concomitant decrease in charge carrier mobility. These competing effects combine to predict exciton dissociation yields that are maximized with a moderate amount of molecular disorder.

In the following section we describe the details of our model system. Then, in Sections 5.3 through 5.6 we present the results of our investigation, highlighting disorder's influence on both the equilibrium (*i.e.*, thermodynamic) and nonequilibrium driving forces. In Section 5.7 we demonstrate that the nonequilibrium effects of disorder on dissociation dynamics can be captured in the context of a simple kinetic model. Finally, in Section 5.8, we discuss the implications of our finding for modern organic electronics.

5.2 A Coarse-Grained Model of Charge-Transfer Exciton Dynamics

To simulate the effect of nanoscale disorder on exciton dissociation requires system sizes and time scales that are well beyond the capability of modern quantum chemistry. Fortunately, our recent work has revealed that dynamics of CT excitations can be accurately described using a simple and efficient coarse-grained model of incoherent charge carrier dynamics.[83] Our investigation utilizes this theoretical framework to

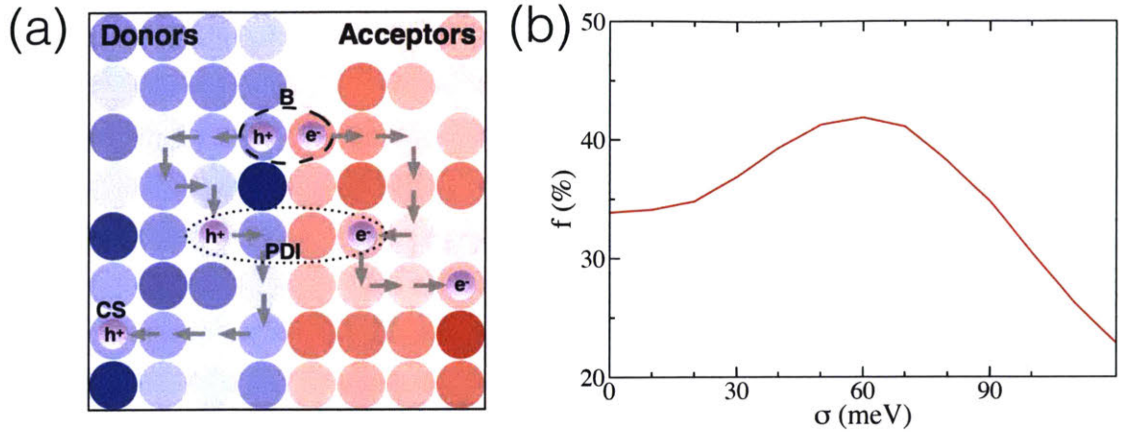

Figure 5-1: (a) A schematic of our model for simulating the dynamics of interfacial CT excitons. The color shadings of the blue and red circles represent the varying HOMO energies of donor molecules and LUMO energies of acceptor molecules, respectively. The circles with h^+ and e^- are the hole and electron in the CT exciton, respectively. A representative trajectory is shown as grey arrows, where the electron and hole break apart gradually from the bound CT state (B), to the partially dissociated intermediate state (PDI), and finally to the fully dissociated state (CS). The definitions of the B, PDI, and CS states are given in the main text. (b) The dependence of the CT exciton dissociation yield, f, on the energetic disorder, σ.

reveal the fundamental relationship between static molecular disorder and the dissociation of CT excitons. Our model does not include any specific atomistic-level detail, nor does it include high-level information about the electronic structure. Nonetheless, as we have previously demonstrated,[83, 129] when this model is parameterized appropriately it exhibits the remarkable ability to reproduce, with near quantitative accuracy, multiple experimental observations related to the dynamics of CT excitons, including transient photoluminescence data, transient spatial broadening and spectral red-shift from time-resolved fluorescence microscopy on an organic donor-acceptor blend.[83]

As illustrated in Figure 5-1(a), our model describes the system as a collection of individual molecules arranged on a two-dimensional square lattice and separated into a donor phase and an acceptor phase. We describe the presence of molecular disorder by assigning each molecule a HOMO or LUMO energy, denoted ϵ_{HOMO} or ϵ_{LUMO} respectively, drawn randomly from a Gaussian distribution, $P(\epsilon) = (2\pi\sigma^2)^{-1/2}\exp[-(\epsilon - \epsilon^{(0)})^2/2\sigma^2]$. Here $\epsilon^{(0)}$ denotes the average orbital energy and σ defines the width of the site energetic distribution. We control the amount of disorder within the system by varying the width of the Gaussian distribution, indicated in terms of σ. This approximate treatment of static disorder has been widely adopted by others,[108, 109, 111, 120] and the resulting charge transport model is sometimes called Gaussian disorder model, proposed originally by Bässler and his co-workers.[130] Charge transfer excitations are modeled as point particles of opposite charge (*i.e.*, electron and hole) that are localized on separate donor and acceptor molecules. The potential energy of a given CT state is given by $E = E^{(\mathrm{Coul})} + E^{(\mathrm{vert})}$, where $E^{(\mathrm{Coul})}$ denotes the electrostatic interaction of the electron and hole and $E^{(\mathrm{vert})}$ is the HOMO-LUMO gap of the specific donor-acceptor pair that is occupied, (i.e., $E^{(\mathrm{vert})}$ is given by the difference between the values of ϵ_{LUMO} of the electron's site and ϵ_{HOMO} of the hole's site). The approximate expression for the CT state energy in our model provides a lower bound estimate of the CT state energy,[91] and its parameters were derived from experimental spectroscopic data.[97]

The time evolution of the CT state is determined by a kinetic Monte Carlo (KMC) algorithm that simulates the asynchronous hopping of electrons and holes. The KMC algorithm also includes a ground state recombination process, which can only occur if the electron and hole reside on adjacent molecules. This recombination process results in the termination of the trajectory. At each KMC step, we allow either the electron or the hole, but not both, to hop to its nearest-neighboring sites stochastically, and the possible new electron-hole configuration has the energy of E'. The hopping rate of the electron-hole pair then is determined by the Miller-Abrahams formula,[95] widely used for single charge migration:

$$k_{\mathrm{MA}} = \nu \exp\left[-\beta(E' - E + |E' - E|)/2\right], \tag{5.1}$$

where ν is the normalized hopping frequency, and $\beta = 1/k_{\mathrm{B}}T$. When the electron and hole are on the adjacent sites at the interface, namely the electron-hole pair being the interfacial CT exciton, they may recombine with a decay rate of k_c. The values of parameters, $T = 300K, k_c = 0.3\mu s^{-1}$, $\nu = 15.0\mu s^{-1}$, $a = 2.5$ nm, and $\varepsilon = 3.5$, were identical to those in Ref. [83], which along with $\sigma = 60$ meV generated excellent agreements with multiple experimental observations (*e.g.*, spatial broadening and spectral red shift of the transient photoluminescence signal) on a donor-acceptor blend of organic semiconductors, 4,4',4"-tris[3-methylphenyl(phenyl)amino]-triphenylamine and tris-[3-(3-pyridyl)-mesityl]borane. The charge recombination rate and the charge hopping rates can be determined based on a combination of experimental inputs and theoretical models, as described in the previous chapter. We assume excitons are fully dissociated when the electron and hole are separated by a distance that is greater than the Coulomb radius, which we define as the distance for which $E^{(\mathrm{Coul})} = k_{\mathrm{B}}T$. Since this assumption neglects many contributions to trapping and recombination, our computed dissociation yields represent an upper limit of the actual process. Notably, however, if such loss mechanisms are independent of disorder, then the relative dissociation yields we compute are expected to be more accurate than their absolute values.

KMC simluations for individual trajectories were carried out for 100 μs (about three times of the observation time window in the experiment) unless we terminated the KMC trajectories earlier due to the radiative recombination. The electron and hole were initiated adjacently at the interface (*i.e.*, starting as an interfacial CT exciton), and 100000 KMC trajectories were harvested for each energetic disorder, σ, to compute the CT exciton dissociation yield, estimated from the fraction of trajectories for which $r > r_c$ at the termination of KMC simulations. The convergence of the results with respect to the lattice size, the KMC simulation time (within a reasonable time window), and the number of realizations of disordered lattice configurations has been verified. It is worthwhile to mention that our simulation attempts with the three-dimensional lattice gave similar results, but led to faster relaxation in transient spatial broadening of the photoluminescence signal compared to the two-dimensional lattice, making the agreement with experiment less satisfactory.

In the results presented below we have utilized the same model parameterization as in the previous chapter.[83] Although this parameterization has been optimized to describe the dynamics of a specific donor-acceptor blend, we take it to be representative of a generic small-molecule organic heterojunction. We generate trajectories by randomly initializing electrons and holes on adjacent molecules along the donor-acceptor interface. We do this to mimic the process of photoexcitation, which we assume yields a population distributed uniformly within the energetic density of states. We neglect contributions from electronically hot CT states, meaning that CT states in our model are uniquely specified by the electron and hole positions. For a given value of σ we generate ensembles of trajectories by sampling the dynamics of many CT states over many different realizations of the random energetic disorder. The analysis and interpretation of these trajectories are presented in the sections below.

5.3 Dependence of Dissociation Yield on Disorder

To study the effect of disorder on exciton dissociation we analyze ensembles of trajectories generated at various values of σ. For a given value of σ we determine the dissociation yield, f, by computing the fraction of trajectories that avoid recombination and escape the Coulomb capture radius (about 16 nm in this system). The plot in Figure 5-1b illustrates that the dissociation yield depends non-monotonically on the amount of disorder in the system. In other words, exciton dissociation is maximized in systems that include a finite amount of energetic disorder. This finding is not without precedent. Disorder-induced increases in exciton dissociation yields have been demonstrated previously in experiment [107] and in simulation studies.[108–111] At the same time, it is well known that high levels of disorder lead to efficiency loss due to reduction in charge transport properties.[130] Taken together, these competing effects suggest the existence of a maximum in f at some optimal level of energetic disorder. Despite this, the microscopic origins of these effects, and how their interplay mediates exciton dissociation, remains uncharacterized. Our model study addresses this problem by identifying the nonequilibrium effects that are responsible for a disorder-induced enhancement in the CT dissociation process.

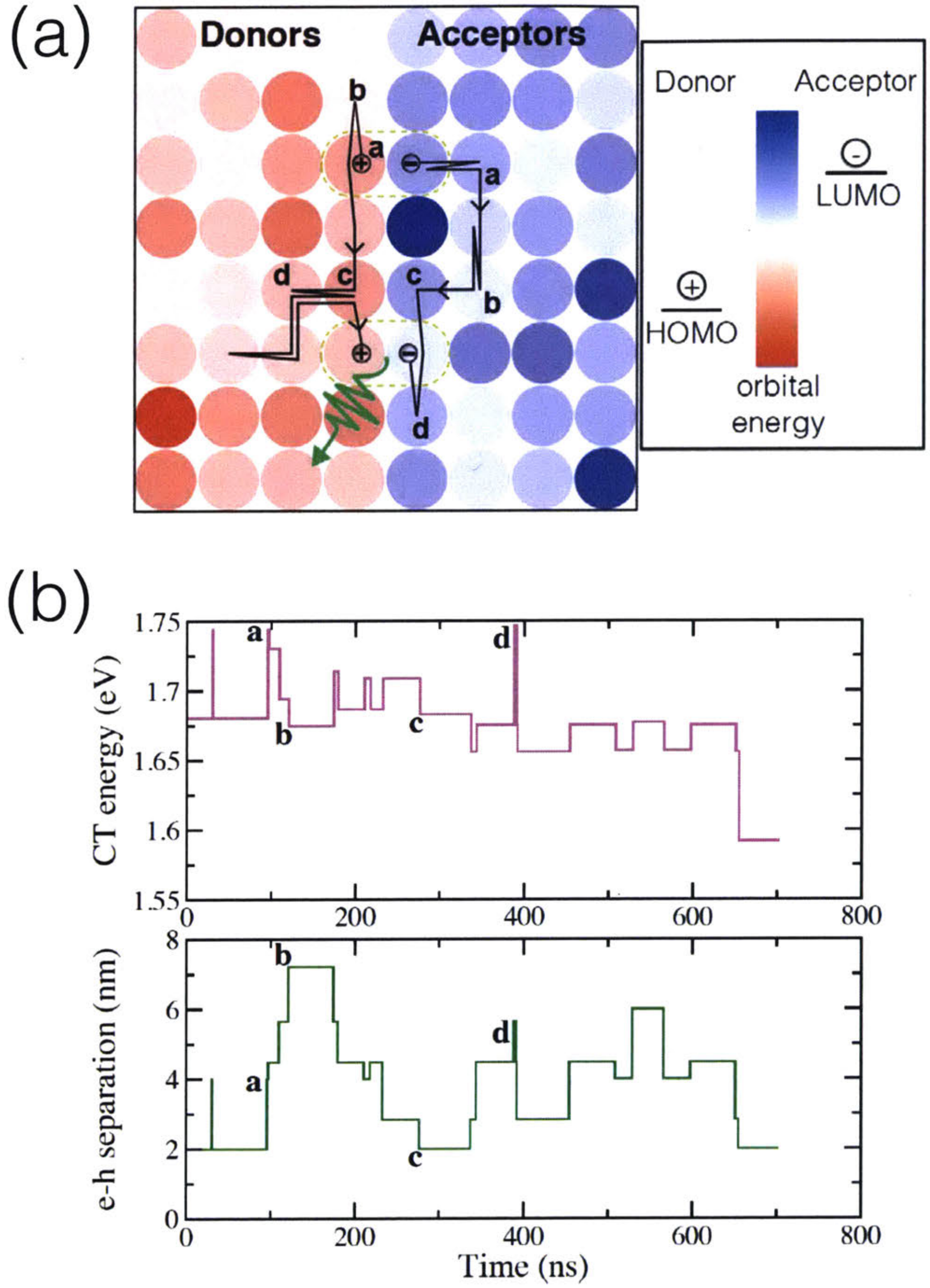

Figure 5-2: (a) A schematic of a representative trajectory from KMC simulations. Red and blues circles are the donor and acceptor molecules on the square lattice, respectively. The color gradient represents the distributions of the HOMO energy of the donors and the LUMO energy of the acceptors, as illustrated in the color scale. The labels (a-d) indicate some instants in the trajectory. (b) The time evolution of the CT exciton energy (top, magenta line) and the electron-hole separation (bottom, dark green line). The labels correspond to the same instants in panel (a).

5.4 A Sample Kinetic Monte Carlo Trajectory

To obtain insights into how disorder could enhance CT exciton dissociation process, we study a representative KMC trajectory shown in Figure 5-2, along with the time evolution of the CT state energy and the electron-hole separation shown in panel (b). The labels (a-d) highlight some instants in the trajectory. There are several interesting observations about this particular trajectory: 1) the electron avoids the high-energy site (from the initial point to point c) in its migration; 2) at instant b, the electron and hole reach their largest separation, forming the stretched CT state; 3) at instant c, the electron and hole reconvene at the interface, but they separate again after a brief stay; 4) soon after instant d, the electron arrives at its final destination, but the hole has not yet settled down and is still wandering around under the electric field of the electron at the interface. Because of this Coulombic attraction, the hole is not able to escape even though there are available lower-energy sites nearby; 5) finally, the electron and hole recombine and emit a photon at the sites 7.5 nm away from their initial sites. Moreover, the final resident sites are 90 meV lower in energy than the initials sites, manifesting the thermodynamic driving force for the CT state diffusion.

5.5 The Effect of Disorder on the Thermodynamics of Exciton Dissociation

Prior to a discussion of the nonequilibrium dissociation dynamics it is useful to consider how energetic disorder affects the equilibrium properties of CT excitons. Here we use the term *equilibrium* in reference to the ensemble of electronically excited states, specifically omitting the manifold of electronic ground states. Recently, Hood and Kassal used a similar model to compute the free energy associated with varying the electron-hole separation and found that an increase in the amplitude of disorder can result in a decrease in the free energy barrier for exciton dissociation dynamics.[111] Our model also exhibits this behavior, as illustrated in the bottom panel of Figure 5-3, which contains a plot of the CT dissociation free energy, $F(d)$, computed for various values of σ. We define the dissociation free energy as,

$$F(d) = -k_{\mathrm{B}}T\langle \ln Q(d)\rangle, \tag{5.2}$$

where the angle brackets represent an average over realizations of the random energetic disorder and $Q(d)$ is the constrained partition function for the ensemble of states with an electron-hole separation equal to d. Specifically,

$$Q(d) = \sum_{\mathbf{x}} \delta_{d,d_{\mathbf{x}}} e^{-\beta E_{\mathbf{x}}}, \tag{5.3}$$

where the summation is taken over all possible configurations of the electron and hole position, $E_{\mathbf{x}} = E_{\mathbf{x}}^{(\mathrm{Coul})} + E_{\mathbf{x}}^{(\mathrm{vert})}$, is the energy of configuration $\mathbf{x}$, $d_{\mathbf{x}}$ is the electron-hole separation for configuration $\mathbf{x}$, and $\delta_{d,d_{\mathbf{x}}}$ is the Kronecker delta function, which is equal to 1 if $d = d_{\mathbf{x}}$ and equal to 0 otherwise. Like Hood and Kassal,[111] we find that the shape of the dissociation free energy depends on σ and that the height of the free energy barrier for dissociation decreases with increasing disorder.

To better understand the origins of this dependence we decompose the function $F(d)$ into its energetic and entropic components. We denote the energetic contribution as,

$$U(d) = k_{\mathrm{B}}T\left\langle \sum_{\mathbf{x}} \delta_{d,d_{\mathbf{x}}} E_{\mathbf{x}} P_{\mathbf{x}} \right\rangle, \tag{5.4}$$

where $P_{\mathbf{x}}$ is the equilibrium probability to observe configuration $\mathbf{x}$, given by

$$P_{\mathbf{x}} = e^{-\beta E_{\mathbf{x}}} \delta_{d,d_{\mathbf{x}}} / Q(d), \tag{5.5}$$

and we denote the entropic contribution as,

$$S(d) = -k_{\mathrm{B}}\left\langle \sum_{\mathbf{x}} \delta_{d,d_{\mathbf{x}}} P_{\mathbf{x}} \ln P_{\mathbf{x}} \right\rangle. \tag{5.6}$$

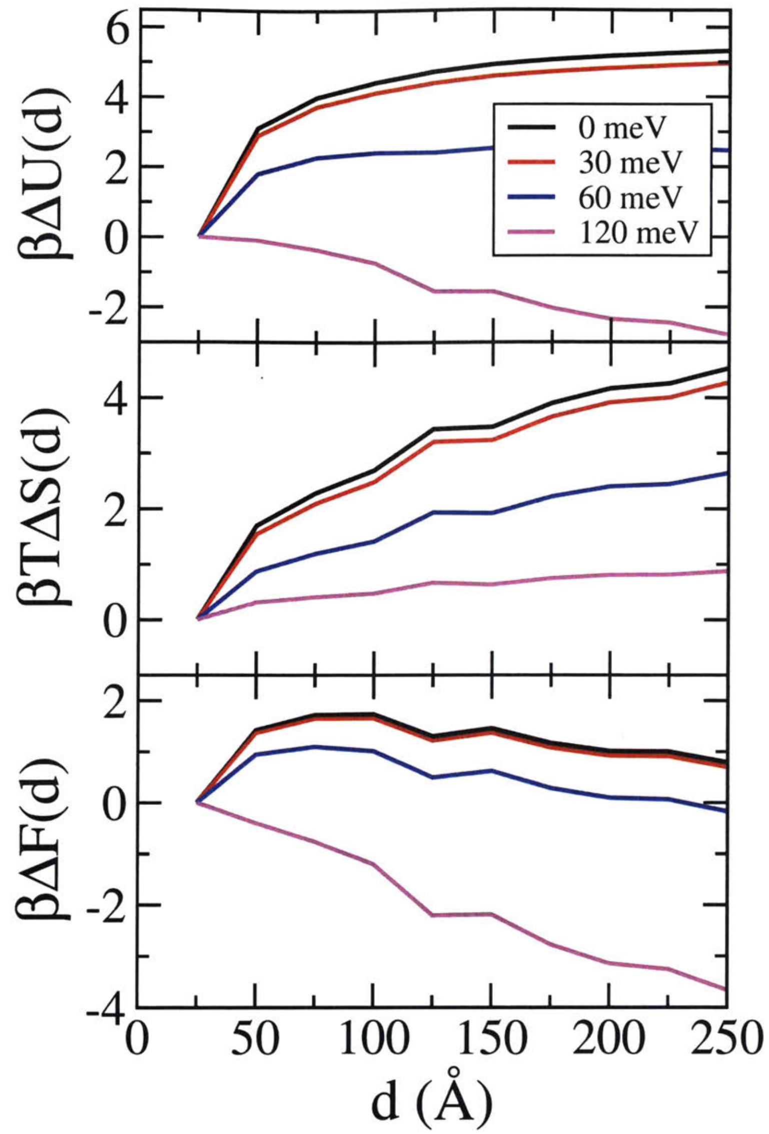

Figure 5-3: The internal energy (top), entropy (middle), and Helmholtz free energy (bottom) profiles as functions of electron-hole separation, d, as evaluated using Eq. (5.2) - (5.6). All the thermodynamic quantities are plotted in units of the thermal energy, $k_{\mathrm{B}}T = 1/\beta$. Four different values of energetic disorder σ are considered: $\sigma = 0$ (black), 30 meV (red), 60 meV (blue), and 120 meV (magenta).

These contributions, which are related via

$$F(d) = U(d) - TS(d) \tag{5.7}$$

, are plotted in Figure 5-3. In the absence of energetic disorder, *i.e.*, when $\sigma = 0$, the shape of $F(d)$ represents a straightforward competition between a Coulombic attraction, reflected in $U(d)_{\sigma=0}$, and an entropic repulsion, reflected by $S(d)_{\sigma=0}$. This competition is known to yield a free energy barrier, which is about $2k_{\mathrm{B}}T$ in our model.

The presence of disorder affects $S(d)$ and $U(d)$ differently. Disorder causes $S(d)$ to shift in a manner that results in a decrease in the entropic driving force for electron-hole separation. This decrease can be understood by considering the effect of energetic disorder on the equilibrium distribution of CT states. The Boltzmann weighted equilibrium distribution is centered at lower energies than that of the overall density of states. As energetic disorder increases, the equilibrium distribution shifts further into the low energy tails of the overall distribution, which results in an effective reduction of phase space and a corresponding entropy decrease.

Disorder causes $U(d)$ to shift in such a way as to reduce, and eventually eliminate, the attractive influence of the Coulomb interaction. This shift (1) increases with disorder and (2) is more pronounced at larger electron-hole separations. These two effects can be understood separately by considering the vertical excitation energy relative to that computed within a perfectly ordered system (*i.e.*, $\sigma = 0$),

$$\Delta E^{(\mathrm{vert})} = E^{(\mathrm{vert})} - E^{(\mathrm{vert})}_{\sigma=0}, \tag{5.8}$$

and its thermodynamic mean,

$$\Delta \bar{E}^{(\mathrm{vert})} = \sum_{\mathbf{x}} \Delta E^{(\mathrm{vert})}_{\mathbf{x}} P_{\mathbf{x}}. \tag{5.9}$$

We quantify the statistics of $\Delta \bar{E}^{(\mathrm{vert})}$ that depend on d and σ in terms of its probability distribution, $P(\Delta \bar{E}^{(\mathrm{vert})})$.

In our finite sized model system, differences in the randomly assigned site energies lead to variations in $\bar{E}^{(\mathrm{vert})}$. These variations are reflected in the line shape of $P(\Delta \bar{E}^{(\mathrm{vert})})$, which would narrow to a delta function in the limit of an infinitely large system. Figure 5-4(a) illustrates that for states with fixed electron-hole separation, increasing σ causes $P(\Delta \bar{E}^{(\mathrm{vert})})$ to shift to lower energies. Figure 5-4(b) illustrates that at fixed σ, increasing d results in a shift of $P(\Delta \bar{E}^{(\mathrm{vert})})$ to lower energies. This

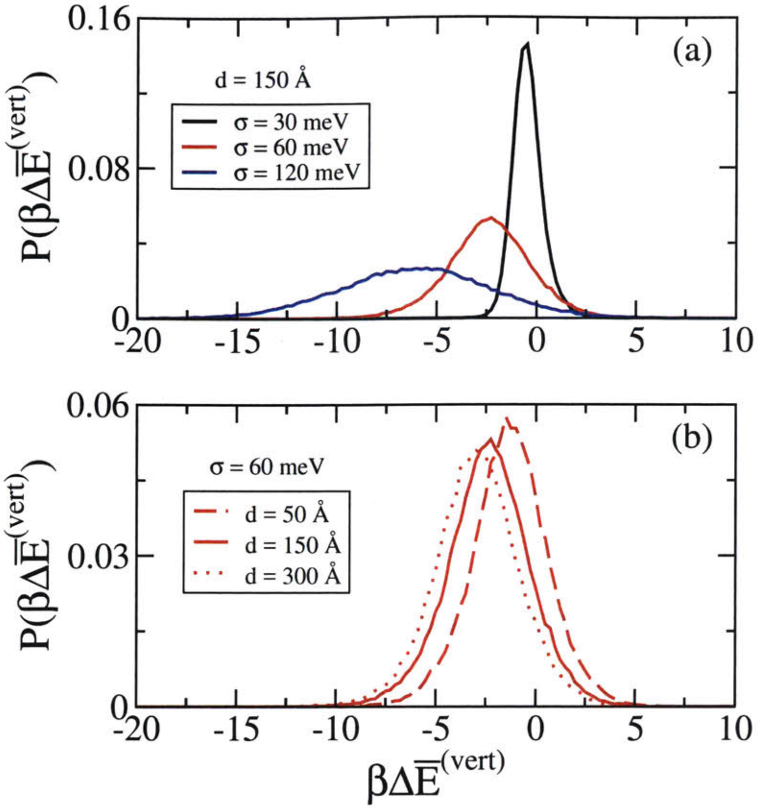

Figure 5-4: The probability distribution of the average value of the vertical energy gap relative to that computed within a perfectly ordered system, $\Delta\bar{E}^{(\mathrm{vert})}$, evaluated from Eq. (5.8) and (5.9): (a) the distributions for $d = 150$ at $\sigma = 30$ meV, 60 meV, and 120 meV; (b) the distributions for three different values of d at fixed σ =60 meV.

shift reflects the fact that pairs of sites with especially low energy are simply more plentiful at larger values of d. These low energy states are dilute within the density of states, but they are weighted heavily in the equilibrium ensemble.

5.6 Nonequilibrium Dissociation Dynamics

Photoexcitation generally creates populations of excitons with energetic distributions that are blue-shifted relative to that of equilibrium. Excitons then equilibrate by relaxing within the local manifold of electronic states, which occurs on ultrafast timescales (*i.e.* ~ 100 fs), and by redistributing in response to spatial energetic variations, which occurs on time scales that are determined by the exciton mobility. During this spatial redistribution the dynamical properties of CT excitons can devi-

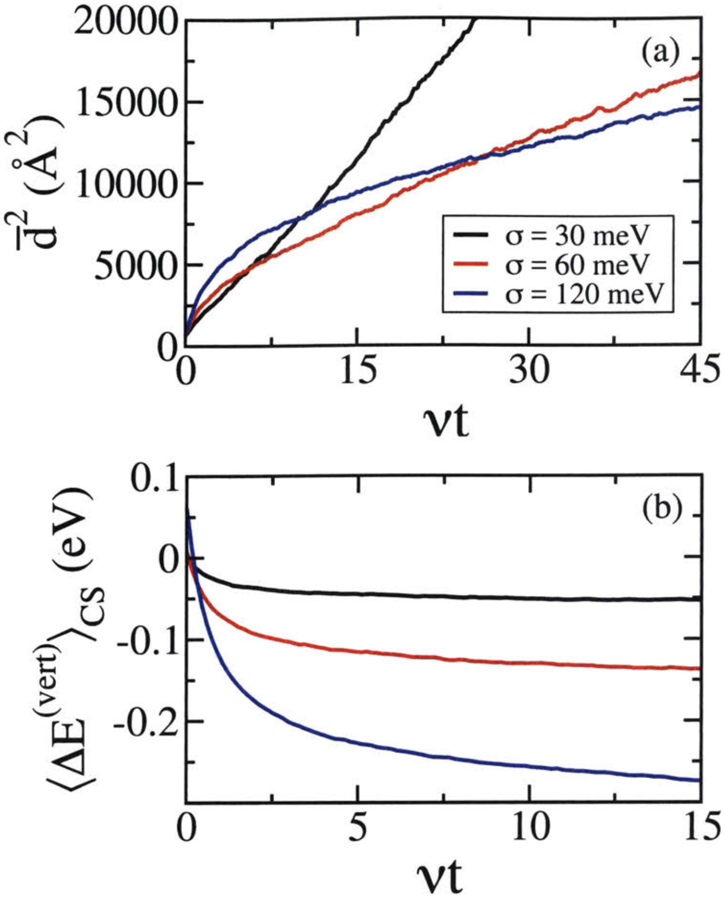

Figure 5-5: (a) A plot of the mean squared electron-hole separation, $\bar{d}^2$, as a function of time expressed in units of the intrinsic hopping rate, ν for trajectories under differing levels of energetic disorder. (b) A plot of the average exciton vertical energetic disorder, denoted as $\langle \Delta E^{(\mathrm{vert})} \rangle_{\mathrm{CS}}$ for charge-separated trajectories under differing levels of energetic disorder.

ate from that of equilibrium. This is illustrated in Figure 5-5(a), which contains a plot of the mean squared electron-hole separation, $\bar{d}^2(t)$, averaged over trajectories initiated in the bound state at $t = 0$. This plot highlights that the effective diffusivity associated with changes in electron-hole separation, as given by the slope of $\bar{d}^2(t)$, is time dependent with more rapid separation dynamics occurring at short times than at long times. In addition, we observe that the intensity of this effect, *i.e.*, the difference in slope between the short time and long time characteristics of $\bar{d}^2(t)$, grows with increasing σ. In this way, disorder tunes a tradeoff between enhanced short time dynamics, which prevent direct charge recombination, and reduced steady state mobility, which controls charge collection efficiency.

The early-time enhancement in charge separation dynamics increases with disorder, in contrast to the well known tendency of energetic disorder to decrease diffusivity.[130] This unusual early-time trend is a nonequilibrium effect that arises due to the increased availability of state-to-state transitions that are downhill in energy.[128, 131] Since these downhill transitions occur more rapidly than their uphill counterparts, due to detailed balance, they tend to dominate the early-time dynamics. This effect diminishes as excitons relocate to lower energy sites with fewer available downhill transitions, resulting in a transient red-shift in the excited state energies,[83] as illustrated in Figure 5-5(b). For some bound CT states these downhill transitions lead to an increase in electron-hole separation. This happens under the condition that the electrostatic cost to separate charge is compensated by a favorable change in vertical excitation energy. This condition is more easily satisfied when σ is large, which is why the initial slope of $\bar{d}^2$ grows with σ.

The dissipation-induced acceleration of the charge separation dynamics is short lived, decaying over a characteristic timescale of approximately $\tau = 30\nu^{-1}$, where ν is the intrinsic charge hopping rate of our model. This implies that the accelerated charge separation dynamics are only significant during the first few intermolecular charge transfer events. This effect alone is therefore insufficient to drive either complete energetic equilibration or complete exciton dissociation (*i.e.*, to separate the charges beyond the Coulomb capture radius). Instead, this process leads to the formation of partially dissociated CT excitons that occupy local minima on the potential energy surface. These partially dissociated states then continue to evolve out of energetic equilibrium but under less strongly driven conditions. It is in the regime that the negative effects of disorder on charge mobility are reflected in the charge separation dynamics.

For the values of σ that we have considered, which are representative of experimental observations in organic heterojunctions, the energetic equilibration time is much larger than CT exciton lifetimes. That is, CT states tend to either recombine or completely dissociate prior to reaching thermal equilibrium. As a consequence, partially dissociated CT states navigate phase space along trajectories that deviate significantly from the minimum free energy path. This is illustrated in Figure 5-6, in which the contour map represents the dissociation free energy resolved as a function of d and $\Delta E^{(\mathrm{vert})}$. The points plotted in Figure 5-6(a)-(c) correspond to those visited by a random set of trajectories that were initialized in the bound CT state. Points plotted in magenta (*i.e.*, the 'x's) represent those visited for times $t < \tau$, *i.e.*, during the time of enhanced charge separation dynamics. We observe that the spread of these initial (magenta) points along the d-axis exhibits a non-monotonic trend with σ that is analogous to that seen in Figure 5-1b. This correlation suggests that the early-time nonequilibrium dynamics play an important role in facilitating CT dissociation.

Figure 5-6**a-c** highlights that in the presence of energetic disorder the dissociation of bound CT states occur out of energetic equilibrium. Therefore, the driving forces that govern the dissociation dynamics are not necessarily determined by the gradient of the equilibrium free energy surface, $F(d)$. Because the dynamics are nonequilibrium, insights and predictions derived from equilibrium analysis can be unreliable and potentially misleading because the actual nonequilibrium driving forces can differ significantly from that of equilibrium. We illustrate this by considering the nonequilibrium analog of the separation energy, $U(d)$ (from Figure 5-3). That is, we compute $U_{\mathrm{neq}}(d)$, the CT state energy along the average nonequilibrium dissociation pathway, defined as

$$U_{\mathrm{neq}}(d) = \left\langle \sum_{\mathbf{x}} \delta_{d,d_{\mathbf{x}}} E_{\mathbf{x}} \right\rangle \tag{5.10}$$

where the averaging is taken over KMC trajectories. The gradient of $U_{\mathrm{neq}}(d)$ is thus one possible measure of the nonequilibrium energetic driving force acting on dissociating CT states. As illustrated in Figure 5-6**d**, $U_{\mathrm{neq}}(d)$ can differ significantly from $U(d)$ in a manner that depends on thc value of σ. Modeling the explicit nonequilibrium dynamics thus allows that these important differences are properly accounted for.

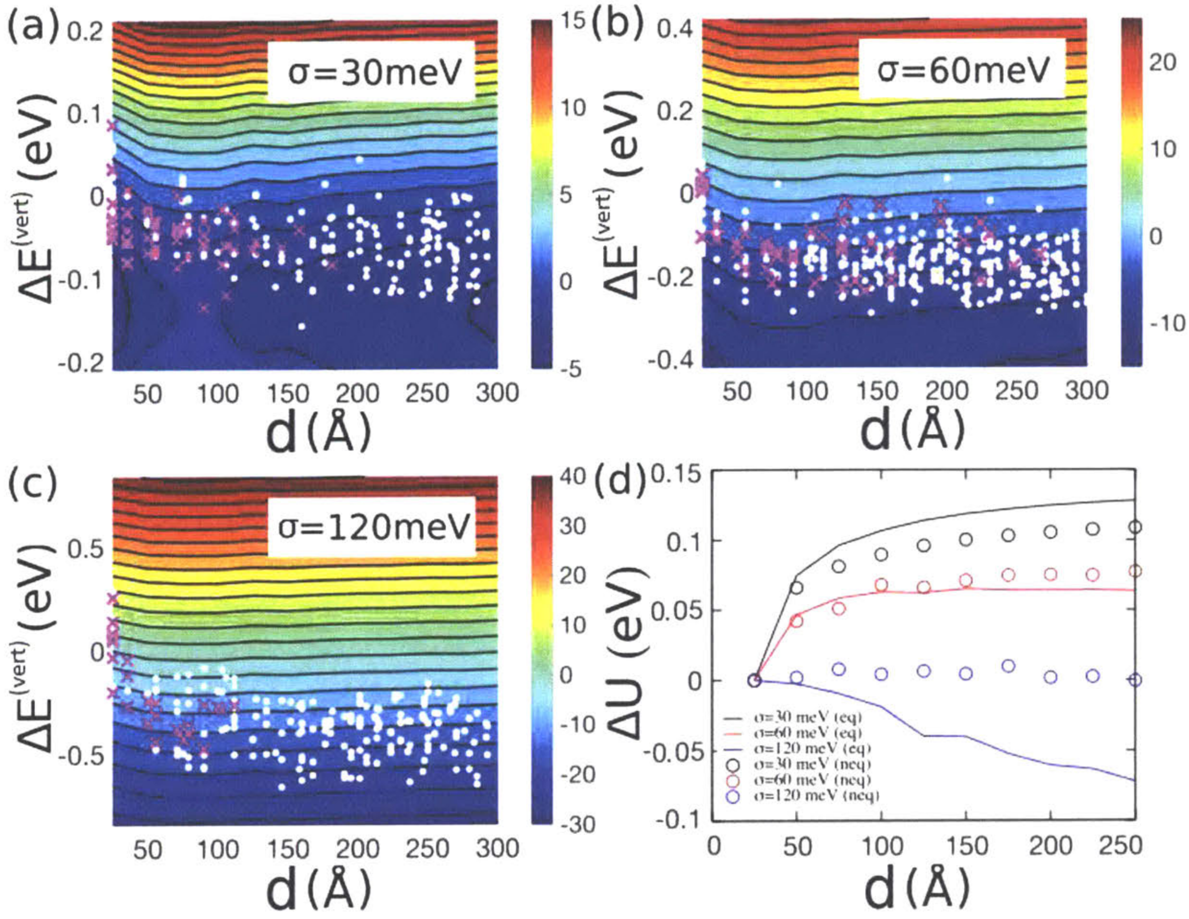

Figure 5-6: (a)-(c): the 2D Helmholtz free energy profiles as a function of electron-hole separation, d in , and relative vertical energy gap, $\Delta E^{(\text{vert})}$ in eV defined by Eq. (5.8) for $\sigma = 30$ meV (panel (a)), 60 meV (panel (b)), and 120 meV (panel (c)); The contour scale is in the unit of k_BT, the magenta crosses and the white dots are from selected KMC trajectories with random initial conditions (see the main text for details). (d) The equilibrium internal energy profiles (lines) and its nonequilibrium analogs (circles), defined by Eq. (5.10), as functions of d, for varying amounts of energetic disorder.

5.7 A Kinetic Model for Nonequilibrium CT State Dissociation

Traditional kinetic models of CT dissociation, as exemplified by the pioneering work of Braun,[132] describe the transition between bound and dissociated state as an activated first-order process.[133] These models predict dissociation yields that decrease monotonically with disorder, [2] which is in clear disagreement with the non-monotonic results of our simulation study (see Figure 5-1). We hypothesize that the origin of this disagreement is that (1) these two-state models fail to capture the fundamental role played by partially dissociated intermediates in the dissociation process and (2) these models are not parameterized to include the important effects of disorder-induced nonequilibrium electron-hole dynamics. Here we demonstrate that models that account for these two effects can exhibit dissociation yields that vary non-monotonically with disorder. This demonstration further highlights the fundamental role of nonequilibrium effects in the dynamics of photo-generated CT states.

Our simulation results have shown that a primary effect of nonequilibrium dynamics is a significant increase in the rate of formation of partially dissociated intermediate states (PDIs). A minimal model of CT dissociation should include the effect of these states, which generally exhibit increased lifetimes and weakened electrostatic attractions, and thus play an important role in facilitating CT dissociation. The properties of these PDIs, such as the rate at which they are formed, their lifetime, and their mobility, depend on the amount of disorder in the system, and this dependence, in turn, can contribute significantly to the dissociation kinetics. We illustrate this by considering how the time spent by trajectories in the bound or partially dissociated states is affected by disorder. In particular, we compute the mean residence time, t_{res}, for trajectories in the bound or partially dissociated states. We identify bound state (B) configurations as those for which the electron and hole reside on adjacent molecules and PDI configurations as those that are not bound and have an electron-hole separation that is less than the Coulomb capture radius (approximately 16 nm in our model).

Figure 5-7 shows t_{res} for bound and partially dissociated states, averaged an ensemble of trajectories initialized in the bound state. This figure illustrates two significant kinetic consequences that arise due to disorder: First, the tendency for disorder to

---

[2] In some traditional kinetic models, including the Braun model, the dissociation yield only depends on the intrinsic recombination rate and the dissociation rate. As the (thermalized) dissociation rate decreases with energetic disorder, the dissociation yield predicted by these models also decreases monotonically with disorder.

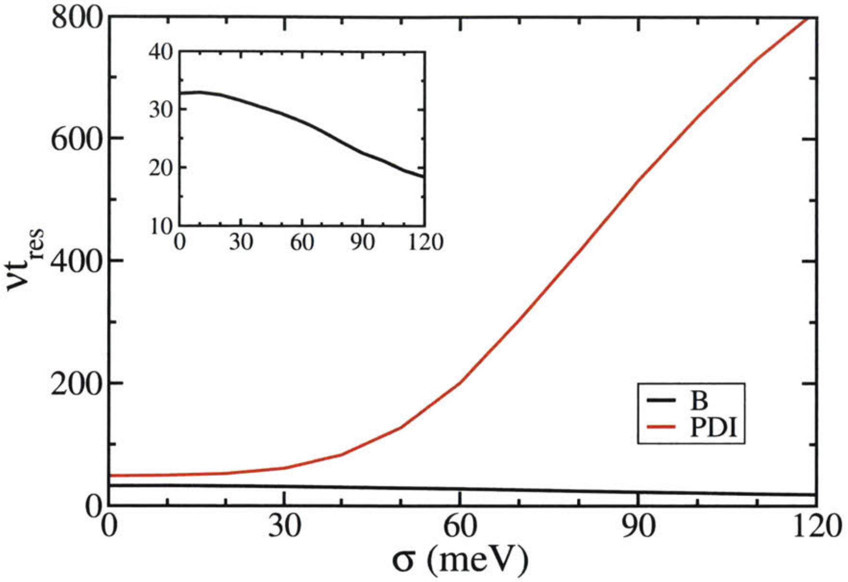

Figure 5-7: Average residence time of the electron and hole in the bound (black line) or partially dissociated (red line) states plotted as a function of σ. Residence times are expressed in units of the intrinsic charge hopping time, $1/\nu$. The bound state (black line) is also shown in the inset for a better view.

drive the formation of partially dissociated states leads to a decrease in t_{res} for the bound CT states. Second, the tendency of disorder to decease charge mobility leads to an increase in t_{res} for the partially dissociated states. This latter effect is subtle when disorder is small but it is dramatic for $\sigma \gtrsim 50$meV (about twice the thermal energy). We attribute this to the increasing role of disorder (most specifically trap states) in limiting CT mobility.[134] The balance of these two effects can be effective captured within the framework of a simple kinetic model.

We represent the dynamics of CT dissociation in terms of the following four-state kinetic model:

$$\text{G} \xleftarrow{k_c} \text{B} \underset{k_{21}}{\overset{k_{12}}{\rightleftharpoons}} \text{PDI} \xrightarrow{k_{23}} \text{CS} \tag{5.11}$$

In this model the dissociation process involves the transition of a bound CT state (B) to a fully dissociated state (CS) via a partially dissociated intermediate state (PDI). The model also includes a competing process for the irreversible recombination to the ground state (G), which can occur only from the bound state. The transition rates, k_{12}, k_{21}, and k_{23}, are computed based on the Miller-Abrahams framework of our KMC model. Specifically, we compute the transition rate k_{ij} as,

$$k_{ij} = \int_{-\infty}^{\infty} dE_i \int_{-\infty}^{\infty} dE_j \; P(E_i, E_j) k_{\mathrm{MA}}(E_j - E_i), \tag{5.12}$$

where $P(E_i, E_j)$ is the probability that a state-to-state transition will have an energy change from E_i to E_j, and $k_{\mathrm{MA}}(E_j - E_i)$ is the Miller-Abrahams rate[95] to perform such a transition, which only depends on the energy difference, $E_j - E_i$. Explicitly, $P(E_i, E_j)$ can be expressed as

$$P(E_i, E_j) = f(E_i) g(E_i) f(E_j), \tag{5.13}$$

where $f(E)$ is the Gaussian distribution function of $E = E^{(\mathrm{vert})} + E^{(\mathrm{Coul})}$ with a standard deviation of $\sqrt{2}\sigma$ due to the Gaussian distributed vertical energy gap, and $g(E)$ is a thermal population function defined by

$$g(E) = A e^{-B\beta E}, \tag{5.14}$$

where $\beta = 1/k_B T$, B is a tuning parameter, and A is a normalization factor to ensure $\int_{-\infty}^{\infty} f(E) g(E) dE = 1$. It is evident that with $B = 1$, $g(E)$ is the equilibrium Boltzman distribution, whereas with $B = 0$, $g(E)$ is a uniform distribution, meaning that there is no thermalization at all. With the Miller-Abrahams formula in Eq. (5.1) and some algebraic manipulations, the average transition rate is given by

$$\begin{aligned} k_{ij} &= \frac{1}{2} e^{2\beta^2\sigma^2 - \beta(\Delta E_{ij}^{(\mathrm{Coul})} + 2B\beta\sigma^2)} \mathrm{erfc}\left(\frac{4\beta\sigma^2 - \Delta E_{ij}^{(\mathrm{Coul})} - 2B\beta\sigma^2}{2\sqrt{2}\sigma} \right) \\ &+ \frac{1}{2} \mathrm{erfc}\left(\frac{\Delta E_{ij}^{(\mathrm{Coul})} + 2B\beta\sigma^2}{2\sqrt{2}\sigma} \right), \end{aligned} \tag{5.15}$$

where $\Delta E_{ij}^{(\mathrm{Coul})}$ denotes the Coulomb energy change associated with hopping transitions between the corresponding state types. In our model calculations, for k_{12}, we use $\Delta E_{ij}^{(\mathrm{Coul})} = 60$ meV, which roughly corresponds to the average Coulomb energy change when the electron or hole in the CT state makes one hop in our model. For

k_{21}, $\Delta E_{ij}^{(\mathrm{Coul})} = -60$ meV as the transition is the reverse to that with k_{12}. For k_{23}, we use $\Delta E_{ij}^{(\mathrm{Coul})} = 5$ meV, which roughly corresponds to the Coulomb energy change when the electron or hole makes its final hop to escape the Coulomb capture radius to be considered as free electron or hole. It is worthwhile to point out that though the values of $\Delta E_{ij}^{(\mathrm{Coul})}$ is system-dependent and in principle can be estimated from simulations or experiment, the qualitative behaviors of k_{ij} as a function of σ is expected to be similar to those discussed in this work provided that reasonable values of $\Delta E_{ij}^{(\mathrm{Coul})}$ are used.

We incorporate nonequilibrium effects into this kinetic model by varying the conditions for which $P(E_i, E_j)$ is computed. For instance, in a fully thermalized model k_{12} is computed by assuming that $P(E_i, E_j)$ reflects the Boltzmann weighted density of states for both the bound and partially dissociated states. Rates for the thermalized model, and how they depend on σ are plotted in Figure 5-8a. A model with a nonequilibrium value of k_{12} can be generated by assuming that the bound states are not thermalized (*i.e.*, sampled directly from Gaussian disorder) but that the manifold of partially dissociated states are fully thermalized. The dependence of k_{12} on σ for this nonequilibrium case is also plotted in Figure 5-8a. We observe that for the thermalized model all rates decrease with increasing disorder, however, when nonequilibrium effects are included increasing disorder can enhance state-to-state transition rates. The transition rate k_{12} (Eq. 5.16) can be tuned with the parameter B between a fully thermalized model, by setting $B = 1$, to the nonequilibrium model described in the paragraph above, by setting $B = 0$. Intermediate values of B thus correspond to models in which the bound state distribution is only partially thermalized. Here we explore a family of these four-state kinetic models for which k_{12} is assumed to be a nonequilibrium rate while k_{21} and k_{23} are assumed to reflect a fully thermalized system. This is akin to assuming that bound states begin out of equilibrium but thermalize rapidly upon transition to the PDI state. These rates can be computed analytically, as described in the Supporting Information.

The dissociation yield for this four-state kinetic model is given by,

$$f = \frac{k_{12}k_{23}}{k_{12}k_{23} + k_c(k_{21} + k_{23})}. \tag{5.16}$$

As illustrated in Figure 5-8**b**, we observe that for the fully thermalized model (B=1), dissociation yields decrease monotonically with increasing disorder, just as in the case of the Braun model. We find that when nonequilibrium effects are included in the model, specifically in the rate k_{12}, that the model predicts nonmonotonic dissociation yields, in qualitative agreement with the results of our simulation study. Furthermore, the details of this nonmonotonic dependence, such as the value of σ that maximizes f, depend on the degree to which nonequilibrium effects are included. The largest notable difference between the framework of this kinetic model and the behavior of our simulation system is that in the kinetic model the rates k_{12}, k_{21}, and k_{23}, are assumed to be time independent. That is, the kinetic model does not explicitly reflect variations that result from transient relaxation behavior. Therefore, by more precisely accounting for the effect of transient relaxation on the time-dependence of k_{12}, k_{21}, and k_{23}, the quantitative accuracy of this model can be systematically improved.

5.8 Implications for modern organic electronics

The macroscopic properties of organic electronic materials depend on the microscopic arrangements of the molecule that comprise them. This dependence has the potential to enable the development of new materials with unique and tunable electronic properties. This tunability requires the need for precise molecular-scale control over microscopic material structure. This level of control is usually achieved by creating highly ordered materials such as molecular crystals.[6, 104, 105] The electronic properties of these ordered materials are typically affected negatively by the presence of disorder. This has led to the notion that disorder is generally undesirable in organic electronic materials.

The results presented here reveal that the presence of microscopic disorder can

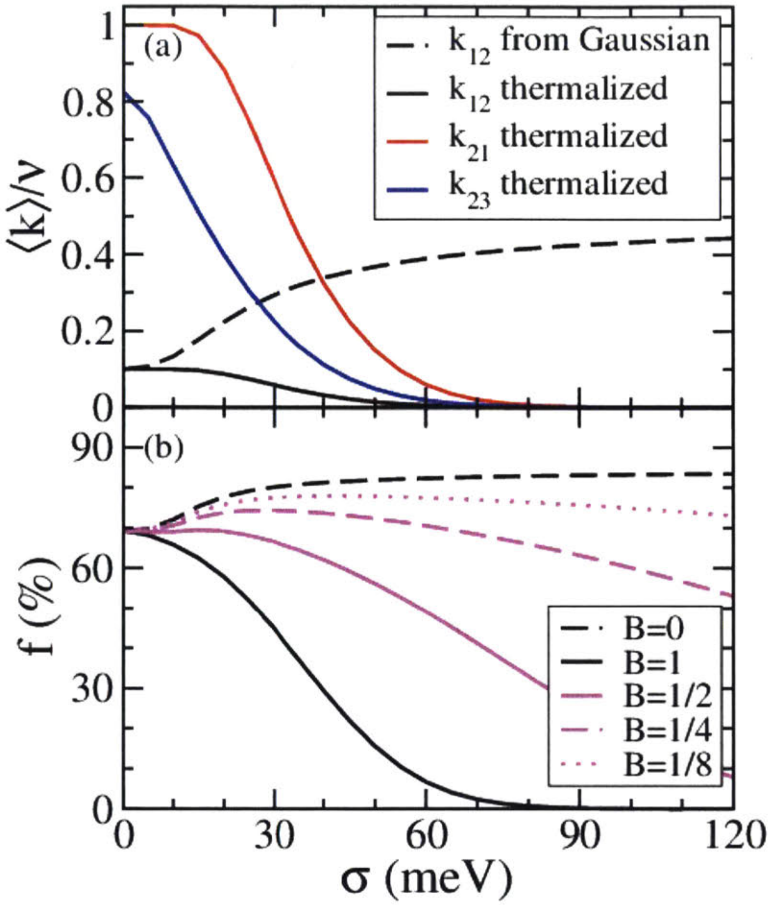

Figure 5-8: (a) The representative rates for the transitions in the kinetic model in Eq. 5.11, as a function of σ, computed from Eq. 5.12. The three solid lines are for the transition rates assuming that the initial states are fully thermalized ($B = 1$), and the black dashed line is for k_{12} assuming that the bound CT states are not thermalized ($B = 0$); (b) The dissociate yield, f, as a function of σ, computed from Eq. 5.16 with the k_{12} rates using varying values of B, a measure of the thermalization level of the bound CT states.

be beneficial for some fundamental electronic processes. For the dissociation of CT excitons this beneficial effect is mediated by nonequilibrium dynamics and is therefore not apparent in thermodynamic analysis. The quantitative details of the results we have presented above, such as the specific value of σ for which CT dissociation is optimized, depend on the model parameterization. Nonetheless, we expect that the primary conclusions presented here, namely that CT dissociation is enhanced when some disorder is present and that the origins of this enhancement are due to nonequilibrium dynamics, apply more generally. This demonstration raises the possibility that disorder may be beneficial to other microscopic electronic processes. In this regard further investigation is needed, but, as we have highlighted here, future approaches must incorporate the important effect of nonequilibrium dynamics along with other factors that are not included in our current model, such as non-geminate recombination, dynamic disorder, and electronic delocalization.

The effect we have presented here can be incorporated into material design principles. The disorder-induced enhancement of CT dissociation can be further enhanced by controlling the spatial distribution of the molecular disorder. For example, by creating systems where the disorder is localized at the interface and have more ordered bulk phase environments. One expects this type of morphology to arise naturally at the boundary between two distinct crystal phases, where lattice mismatches lead to disordered interfaces. Notably, the presence of this general morphology may help explain the unexpectedly high internal quantum efficiencies that have been observed in some organic photovoltaic materials.[116, 135]

Chapter 6

Conclusions

In conclusion, we investigated two important processes that are central to the performance of organic semiconductors: transport of Frenkel exciton and dissociation of charge-transfer exciton. The first half of the thesis (Chapters 2 and 3) is devoted to the simulations of Frenkel exciton dynamics in oligothiophene-based molecular semiconductors. In Chapter 2, we model the dependence of transport properties Frenkel exciton on excited energy fluctuations in extended sexithiophene systems by performing extensive semi-empirical electronic structure and molecular dynamics simulations. We show that the excited energy fluctuations are temporally and spatially correlated. We further demonstrate that exciton transport in these materials can be very sensitive to the presence of the spatial correlations, and that this sensitivity depends on the width of the distribution of molecular excitation energies. In Chapter 3, we propose to incorporate the statistics from atomistic MD-electronic structure calculations into a coarse-grained tight binding model and demonstrate that the improved coarse-grained model is capable of reproducing results from atomistic simulations at a much lower computational costs without sacrificing the molecular details of the materials. This computationally efficient model allows us to study system size of experimental relevance (up to 10,000s of molecules) and our results are in good agreement with many available theoretical predictions and experimental measurements.

In the second half of the thesis (Chapters 4 and 5) we focus on the dissociation dynamics of charge-transfer (CT) exciton. In Chapter 4, we introduce a 2-dimensional stochastic hopping model to describe the electron and hole dynamics in a CT exciton. In contrast to the atomistic approach in the first half of the thesis, the CT exciton model is parametrized using experimental data for a particular donor-acceptor pair (m-MTDATA and 3TPYMB). We demonstrate that simulations carried out on our model are capable of reproducing many sets of experimental results as well as generating theoretical predictions related to the efficiency of organic electronic materials. In Chapter 5, using the same CT exciton model, we consider the effect of spatial variations in electronic energy levels, such as those that arise in disordered molecular systems, on dissociation yield and demonstrate that it is maximized with a finite amount of disorder. We demonstrate that this is a non-equilibrium effect that is mediated by the dissipation driven formation of partially dissociated intermediate states that are long-lived because they cannot easily recombine.

Bibliography

[1] Prabakaran Kumaresan, Sureshraju Vegiraju, Yamuna Ezhumalai, Shueh Lin Yau, Choongik Kim, Wen-Hsi Lee, and Ming-Chou Chen. Fused-thiophene based materials for organic photovoltaics and dye-sensitized solar cells. *Polymers*, 6(10):2645–2669, 2014.

[2] Chao-Ping Hsu. The electronic couplings in electron transfer and excitation energy transfer. *Accounts of Chemical Research*, 42(4):509–518, 2009.

[3] Juan Aragó and Alessandro Troisi. Dynamics of the excitonic coupling in organic crystals. *Physical Review Letters*, 114(2):026402, 2015.

[4] Liang Shi and Adam P Willard. Modeling the effects of molecular disorder on the properties of frenkel excitons in organic molecular semiconductors. *The Journal of Chemical Physics*, 149(9):094110, 2018.

[5] PB Deotare, W Chang, E Hontz, DN Congreve, L Shi, PD Reusswig, B Modtland, ME Bahlke, CK Lee, AP Willard, V Bulović, T Van Voorhis, and MA Baldo. Nanoscale transport of charge-transfer states in organic donor-acceptor blends. *Nature Materials*, 14(11):1130–1134, sep 2015.

[6] JH Burroughes, DDC Bradley, AR Brown, RN Marks, K Mackay, RH Friend, PL Burns, and AB Holmes. Light-emitting diodes based on conjugated polymers. *Nature*, 347(6293):539, 1990.

[7] Lay-Lay Chua, Jana Zaumseil, Jui-Fen Chang, Eric C-W Ou, Peter K-H Ho, Henning Sirringhaus, and Richard H Friend. General observation of n-type field-effect behaviour in organic semiconductors. *Nature*, 434(7030):194, 2005.

[8] Anna Köhler and Heinz Bässler. *Electronic processes in organic semiconductors: An introduction*. John Wiley & Sons, 2015.

[9] Lingxian Meng, Yamin Zhang, Xiangjian Wan, Chenxi Li, Xin Zhang, Yanbo Wang, Xin Ke, Zuo Xiao, Liming Ding, Ruoxi Xia, et al. Organic and solution-processed tandem solar cells with 17.3% efficiency. *Science*, page eaat2612, 2018.

[10] Alexander W. Hains, Ziqi Liang, Michael A. Woodhouse, and Brian A. Gregg. Molecular semiconductors in organic photovoltaic cells. *Chemical Reviews*, 110(11):6689–6735, 2010.

[11] Oksana Ostroverkhova. Organic optoelectronic materials: mechanisms and applications. *Chemical Reviews*, 116(22):13279–13412, 2016.

[12] Jason D Myers and Jiangeng Xue. Organic semiconductors and their applications in photovoltaic devices. *Polymer Reviews*, 52(1):1–37, 2012.

[13] Kjell Cnops, German Zango, Jan Genoe, Paul Heremans, M Victoria Martinez-Diaz, Tomas Torres, and David Cheyns. Energy level tuning of non-fullerene acceptors in organic solar cells. *Journal of the American Chemical Society*, 137(28):8991–8997, 2015.

[14] Julia A Schneider, Afshin Dadvand, Wen Wen, and Dmitrii F Perepichka. Tuning the electronic properties of poly (thienothiophene vinylene) s via alkylsulfanyl and alkylsulfonyl substituents. *Macromolecules*, 46(23):9231–9239, 2013.

[15] Huan Wang, Youjun He, Yongfang Li, and Hongmei Su. Photophysical and electronic properties of five PCBM-like C60 derivatives: spectral and quantum chemical view. *The Journal of Physical Chemistry A*, 116(1):255–262, 2012.

[16] Patrick C Tapping, Scott N Clafton, Kyra N Schwarz, Tak W Kee, and David M Huang. Molecular-level details of morphology-dependent exciton migration in poly (3-hexylthiophene) nanostructures. *The Journal of Physical Chemistry C*, 119(13):7047–7059, 2015.

[17] S Riera-Galindo, A Tamayo, and M Mas-Torrent. Role of polymorphism and thin-film morphology in organic semiconductors processed by solution shearing. *ACS omega*, 3(2):2329–2339, 2018.

[18] Raphael Pfattner, Stefan T Bromley, Concepció Rovira, and Marta Mas-Torrent. Tuning crystal ordering, electronic structure, and morphology in organic semiconductors: Tetrathiafulvalenes as a model case. *Advanced Functional Materials*, 26(14):2256–2275, 2016.

[19] Anna M Hiszpanski, Robin M Baur, Bumjung Kim, Noah J Tremblay, Colin Nuckolls, Arthur R Woll, and Yueh-Lin Loo. Tuning polymorphism and orientation in organic semiconductor thin films via post-deposition processing. *Journal of the American Chemical Society*, 136(44):15749–15756, 2014.

[20] Gleb M Akselrod, Parag B Deotare, Nicholas J Thompson, Jiye Lee, William A Tisdale, Marc A Baldo, Vinod M Menon, and Vladimir Bulović. Visualization of exciton transport in ordered and disordered molecular solids. *Nature Communications*, 5:3646, 2014.

[21] S Matthew Menke and Russell J Holmes. Evaluating the role of energetic disorder and thermal activation in exciton transport. *Journal of Materials Chemistry C*, 4(16):3437–3442, 2016.

[22] Chee Kong Lee, Jeremy Moix, and Jianshu Cao. Coherent quantum transport in disordered systems: A unified polaron treatment of hopping and band-like transport. *The Journal of Chemical Physics*, 142(16):164103, 2015.

[23] Chern Chuang, Chee Kong Lee, Jeremy M Moix, Jasper Knoester, and Jianshu Cao. Quantum diffusion on molecular tubes: Universal scaling of the 1d to 2d transition. *Physical Review Letters*, 116(19):196803, 2016.

[24] Jeremy M Moix, Michael Khasin, and Jianshu Cao. Coherent quantum transport in disordered systems: I. the influence of dephasing on the transport properties and absorption spectra on one-dimensional systems. *New Journal of Physics*, 15(8):085010, 2013.

[25] J Frenkel. On the transformation of light into heat in solids. i. *Physical Review*, 37(1):17, 1931.

[26] Aleksandr Sergeevich Davydov. The theory of molecular excitons. *Physics-Uspekhi*, 7(2):145–178, 1964.

[27] Aaron Sisto, David R Glowacki, and Todd J Martinez. Ab initio nonadiabatic dynamics of multichromophore complexes: A scalable graphical-processing-unit-accelerated exciton framework. *Accounts of chemical research*, 47(9):2857–2866, 2014.

[28] Eric R Bittner. Frenkel exciton model of ultrafast excited state dynamics in at dna double helices. *Journal of Photochemistry and Photobiology A: Chemistry*, 190(2-3):328–334, 2007.

[29] Adrian F Morrison and John M Herbert. Low-scaling quantum chemistry approach to excited-state properties via an ab initio exciton model: Application to excitation energy transfer in a self-assembled nanotube. *The Journal of Physical Chemistry Letters*, 6(21):4390–4396, 2015.

[30] Frank C Spano. Excitons in conjugated oligomer aggregates, films, and crystals. *Annu. Rev. Phys. Chem.*, 57:217–243, 2006.

[31] Aleksey A Kocherzhenko, Xochitl A Sosa Vazquez, Joel M Milanese, and Christine M Isborn. Absorption spectra for disordered aggregates of chromophores using the exciton model. *Journal of chemical theory and computation*, 13(8):3787–3801, 2017.

[32] D Oelkrug, H-J Egelhaaf, and J Haiber. Electronic spectra of self-organized oligothiophene films with ‘standing’ and ‘lying’ molecular units. *Thin Solid Films*, 284:267–270, 1996.

[33] Denis Fichou. *Handbook of oligo-and polythiophenes.* John Wiley & Sons, 2008.

[34] Igor F Perepichka and Dmitrii F Perepichka. *Handbook of Thiophene-Based Materials: Applications in Organic Electronics and Photonics, 2 Volume Set.* John Wiley & Sons, 2009.

[35] Rudolph Pariser and Robert G Parr. A semi-empirical theory of the electronic spectra and electronic structure of complex unsaturated molecules. i. *The Journal of Chemical Physics*, 21(3):466–471, 1953.

[36] Rudolph Pariser and Robert G Parr. A semi-empirical theory of the electronic spectra and electronic structure of complex unsaturated molecules. ii. *The Journal of Chemical Physics*, 21(5):767–776, 1953.

[37] John A Pople. Electron interaction in unsaturated hydrocarbons. *Transactions of the Faraday Society*, 49:1375–1385, 1953.

[38] James B Foresman, Martin Head-Gordon, John A Pople, and Michael J Frisch. Toward a systematic molecular orbital theory for excited states. *The Journal of Physical Chemistry*, 96(1):135–149, 1992.

[39] Jay L Banks, Hege S Beard, Yixiang Cao, Art E Cho, Wolfgang Damm, Ramy Farid, Anthony K Felts, Thomas A Halgren, Daniel T Mainz, Jon R Maple, et al. Integrated modeling program, applied chemical theory (impact). *Journal of Computational Chemistry*, 26(16):1752–1780, 2005.

[40] Kevin J Bowers, David E Chow, Huafeng Xu, Ron O Dror, Michael P Eastwood, Brent A Gregersen, John L Klepeis, Istvan Kolossvary, Mark A Moraes, Federico D Sacerdoti, et al. Scalable algorithms for molecular dynamics simulations on commodity clusters. In *SC 2006 conference, proceedings of the ACM/IEEE*, pages 43–43. IEEE, 2006.

[41] Maria Antonietta Loi, Enrico Da Como, Franco Dinelli, Mauro Murgia, Roberto Zamboni, Fabio Biscarini, and Michele Muccini. Supramolecular organization in ultra-thin films of α-sexithiophene on silicon dioxide. *Nature materials*, 4(1):81, 2005.

[42] Enrico Da Como, Maria Antonietta Loi, Mauro Murgia, Roberto Zamboni, and Michele Muccini. J-aggregation in α-sexithiophene submonolayer films on silicon dioxide. *Journal of the American Chemical Society*, 128(13):4277–4281, 2006.

[43] P Lang, R Hajlaoui, F Garnier, B Desbat, T Buffeteau, G Horowitz, and A Yassar. Ir spectroscopy evidence for a substrate-dependent organization of sexithiophene thin films vacuum evaporated onto sih/si and sio2/si. *The Journal of Physical Chemistry*, 99(15):5492–5499, 1995.

[44] H Haken and P Reineker. The coupled coherent and incoherent motion of excitons and its influence on the line shape of optical absorption. *Zeitschrift für Physik*, 249(3):253–268, 1972.

[45] H Haken and G Strobl. An exactly solvable model for coherent and incoherent exciton motion. *Zeitschrift für Physik A Hadrons and nuclei*, 262(2):135–148, 1973.

[46] Anthony J Leggett, Sudip Chakravarty, Alan T Dorsey, Matthew PA Fisher, Anupam Garg, and Wilhelm Zwerger. Dynamics of the dissipative two-state system. *Reviews of Modern Physics*, 59(1):1, 1987.

[47] Mortaza Aghtar, Johan StruĭĹmpfer, Carsten Olbrich, Klaus Schulten, and Ulrich KleinekathoĭĹfer. The fmo complex in a glycerol–water mixture. *The Journal of Physical Chemistry B*, 117(24):7157–7163, 2013.

[48] Stěphanie Valleau, Alexander Eisfeld, and Alán Aspuru-Guzik. On the alternatives for bath correlators and spectral densities from mixed quantum-classical simulations. *The Journal of Chemical Physics*, 137(22):224103, 2012.

[49] Carsten Olbrich, Johan StruĭĹmpfer, Klaus Schulten, and Ulrich KleinekathoĭĹfer. Theory and simulation of the environmental effects on fmo electronic transitions. *The Journal of Physical Chemistry Letters*, 2(14):1771–1776, 2011.

[50] Alan Aspuru-Guzik, Sangwoo Shim, Patrick Rebentrost, and Stephanie Valleau. Atomistic study of the long-lived quantum coherences in the fenna-matthews-olson complex. 2011.

[51] Patrick Rebentrost, Rupak Chakraborty, and Alán Aspuru-Guzik. Non-markovian quantum jumps in excitonic energy transfer. *The Journal of Chemical Physics*, 131(18):11B605, 2009.

[52] Seogjoo Jang, Stephan Hoyer, Graham Fleming, and K Birgitta Whaley. Generalized master equation with non-markovian multichromophoric förster resonance energy transfer for modular exciton densities. *Physical Review Letters*, 113(18):188102, 2014.

[53] Philip W Anderson. Absence of diffusion in certain random lattices. *Physical Review*, 109(5):1492, 1958.

[54] Masoud Mohseni, Patrick Rebentrost, Seth Lloyd, and Alan Aspuru-Guzik. Environment-assisted quantum walks in photosynthetic energy transfer. *The Journal of Chemical Physics*, 129(17):11B603, 2008.

[55] Patrick Rebentrost, Masoud Mohseni, Ivan Kassal, Seth Lloyd, and Alán Aspuru-Guzik. Environment-assisted quantum transport. *New Journal of Physics*, 11(3):033003, 2009.

[56] Martin B Plenio and Susana F Huelga. Dephasing-assisted transport: quantum networks and biomolecules. *New Journal of Physics*, 10(11):113019, 2008.

[57] Seung-Bum Rim, Reinhold F Fink, Jan C Schöneboom, Peter Erk, and Peter Peumans. Effect of molecular packing on the exciton diffusion length in organic solar cells. *Applied Physics Letters*, 91(17):173504, 2007.

[58] Yuhki Terao, Hiroyuki Sasabe, and Chihaya Adachi. Correlation of hole mobility, exciton diffusion length, and solar cell characteristics in phthalocyanine/fullerene organic solar cells. *Applied Physics Letters*, 90(10):103515, 2007.

[59] Richard R Lunt, Jay B Benziger, and Stephen R Forrest. Relationship between crystalline order and exciton diffusion length in molecular organic semiconductors. *Advanced Materials*, 22(11):1233–1236, 2010.

[60] Anahita Mani, Joop Schoonman, and Albert Goossens. Photoluminescence study of sexithiophene thin films. *The Journal of Physical Chemistry B*, 109(11):4829–4836, 2005.

[61] Kenley M Pelzer, Andrew F Fidler, Graham B Griffin, Stephen K Gray, and Gregory S Engel. The dependence of exciton transport efficiency on spatial patterns of correlation within the spectral bath. *New Journal of Physics*, 15(9):095019, 2013.

[62] Andrea Massé, Pascal Friederich, Franz Symalla, Feilong Liu, Velimir Meded, Reinder Coehoorn, Wolfgang Wenzel, and Peter A Bobbert. Effects of energy correlations and superexchange on charge transport and exciton formation in amorphous molecular semiconductors: An ab initio study. *Physical Review B*, 95(11):115204, 2017.

[63] O. V. Mikhnenko, F. Cordella, A. B. Sieval, J. C. Hummelen, P. W. M. Blom, and M. A. Loi. Temperature dependence of exciton diffusion in conjugated polymers. *The Journal of Physical Chemistry B*, 112(37):11601–11604, 2008. PMID: 18729397.

[64] Jason DA Lin, Oleksandr V Mikhnenko, Thomas S van der Poll, Guillermo C Bazan, and Thuc-Quyen Nguyen. Temperature dependence of exciton diffusion in a small-molecule organic semiconductor processed with and without additive. *Advanced Materials*, 27(15):2528–2532, 2015.

[65] Xinxin Zhong, Yi Zhao, and Jianshu Cao. Coherent quantum transport in disordered systems: Ii. temperature dependence of carrier diffusion coefficients from the time-dependent wavepacket diffusion method. *New Journal of Physics*, 16(4):045009, 2014.

[66] X-Y Zhu, Q Yang, and M Muntwiler. Charge-transfer excitons at organic semiconductor surfaces and interfaces. *Acc. Chem. Res.*, 42(11):1779–1787, 2009.

[67] Carsten Deibel, Thomas Strobel, and Vladimir Dyakonov. Role of the Charge Transfer State in Organic Donor-Acceptor Solar Cells. *Adv. Mater.*, 22(37):4097–4111, 2010.

[68] M Segal, M Singh, K Rivoire, S Difley, T Van Voorhis, and MA Baldo. Extrafluorescent electroluminescence in organic light-emitting devices. *Nat. Mater.*, 6(5):374–378, 2007.

[69] Seth Difley, David Beljonne, and Troy Van Voorhis. On the singlet-triplet splitting of geminate electron-hole pairs in organic semiconductors. *J. Am. Chem. Soc.*, 130(11):3420–3427, 2008.

[70] Jean-Luc Brédas, Joseph E Norton, Jérôme Cornil, and Veaceslav Coropceanu. Molecular understanding of organic solar cells: the challenges. *Acc. Chem. Res.*, 42(11):1691–1699, 2009.

[71] Koen Vandewal, Kristofer Tvingstedt, Abay Gadisa, Olle Inganäs, and Jean V Manca. On the origin of the open-circuit voltage of polymer-fullerene solar cells. *Nat. Mater.*, 8(11):904–909, 2009.

[72] Dirk Veldman, Stefan C J Meskers, and René AJ Janssen. The energy of charge-transfer states in electron donor-acceptor blends: insight into the energy losses in organic solar cells. *Adv. Funct. Mater.*, 19(12):1939–1948, 2009.

[73] Tracey M. Clarke and James R. Durrant. Charge Photogeneration in Organic Solar Cells. *Chem. Rev.*, 110(11):6736–6767, nov 2010.

[74] Artem A Bakulin, Akshay Rao, Vlad G Pavelyev, Paul HM van Loosdrecht, Maxim S Pshenichnikov, Dorota Niedzialek, Jérôme Cornil, David Beljonne, and Richard H Friend. The role of driving energy and delocalized states for charge separation in organic semiconductors. *Science*, 335(6074):1340–1344, 2012.

[75] Askat E Jailaubekov, Adam P Willard, John R Tritsch, Wai-Lun Chan, Na Sai, Raluca Gearba, Loren G Kaake, Kenrick J Williams, Kevin Leung, Peter J Rossky, and X-Y Zhu. Hot charge-transfer excitons set the time limit for charge separation at donor/acceptor interfaces in organic photovoltaics. *Nat. Mater.*, 12(1):66–73, 2013.

[76] S. Gelinas, Akshay Rao, Abhishek Kumar, Samuel L Smith, Alex W Chin, Jenny Clark, T. S. van der Poll, Guillermo C Bazan, and Richard H Friend. Ultrafast Long-Range Charge Separation in Organic Semiconductor Photovoltaic Diodes. *Science*, 343(6170):512–516, jan 2014.

[77] Xiaoyang Zhu, Nicholas R Monahan, Zizhou Gong, Haiming Zhu, Kristopher W. Williams, and Cory A Nelson. Charge Transfer Excitons at van der Waals Interfaces. *J. Am. Chem. Soc.*, 137(26):8313–8320, 2015.

[78] Bin Hu and Yue Wu. Tuning magnetoresistance between positive and negative values in organic semiconductors. *Nat. Mater.*, 6(12):985–991, 2007.

[79] FJ Wang, Heinz Bässler, and Z Valy Vardeny. Magnetic field effects in π-conjugated polymer-fullerene blends: Evidence for multiple components. *Phys. Rev. Lett.*, 101(23):236805, 2008.

[80] Bin Hu, Liang Yan, and Ming Shao. Magnetic-field effects in organic semiconducting materials and devices. *Adv. Mater.*, 21(14-15):1500–1516, 2009.

[81] SP Kersten, AJ Schellekens, Bert Koopmans, and PA Bobbert. Magnetic-field dependence of the electroluminescence of organic light-emitting diodes: A competition between exciton formation and spin mixing. *Phys. Rev. Lett.*, 106(19):197402, 2011.

[82] SP Kersten, AJ Schellekens, Bert Koopmans, and PA Bobbert. Effect of hyperfine interactions on exciton formation in organic semiconductors. *Synth. Met.*, 161(7):613–616, 2011.

[83] Wendi Chang, Daniel N. Congreve, Eric Hontz, Matthias E. Bahlke, David P. McMahon, Sebastian Reineke, Tony C. Wu, Vladimir Bulović, Troy Van Voorhis, and Marc A. Baldo. Spin-dependent charge transfer state design rules in organic photovoltaics. *Nature Communications*, 6:6415, 2015.

[84] Yifei Wang, Kevser Sahin-Tiras, Nicholas J. Harmon, Markus Wohlgenannt, and Michael E. Flatté. Immense magnetic response of exciplex light emission due to correlated spin-charge dynamics. *Phys. Rev. X*, 6:011011, Feb 2016.

[85] Eric Hontz, Wendi Chang, Daniel N Congreve, Vladimir Bulovic, Marc A Baldo, and Troy Van Voorhis. The role of electron–hole separation in thermally activated delayed fluorescence in donor–acceptor blends. *J. Phys. Chem. C*, 119(45):25591–25597, 2015.

[86] Ulrich E. Steiner and Thomas Ulrich. Magnetic field effects in chemical kinetics and related phenomena. *Chem. Rev.*, 89:51–147, 1989.

[87] E. L. Frankevich, A. A. Lymarev, and I. A. Sokolik. CT-excitons and magnetic field effect in polydiacetylene crystals. *Chem. Phys.*, 162(1):1–6, 1992.

[88] P Desai, P Shakya, T Kreouzis, and WP Gillin. Magnetoresistance in organic light-emitting diode structures under illumination. *Phys. Rev. B*, 76(23):235202, 2007.

[89] Ferran Macià, Fujian Wang, Nicholas J Harmon, Andrew D Kent, Markus Wohlgenannt, and Michael E Flatté. Organic magnetoelectroluminescence for room temperature transduction between magnetic and optical information. *Nat. Commun.*, 5:3609, 2014.

[90] SA Crooker, F Liu, MR Kelley, NJD Martinez, W Nie, A Mohite, IH Nayyar, S Tretiak, DL Smith, and PP Ruden. Spectrally resolved hyperfine interactions between polaron and nuclear spins in organic light emitting diodes: Magneto-electroluminescence studies. *Appl. Phys. Lett.*, 105(15):153304, 2014.

[91] a. Dreuw and M. Head-Gordon. Failure of Time-Dependent Density Functional Theory for Long-Range Charge-Transfer Excited States: The Zincbacteriochlorin - Bacteriochlorin and Bacteriochlorophyll - Spheroidene Complexes. *J. Am. Chem. Soc.*, 126(5):4007–4016, 2004.

[92] Klaus Schulten and Peter G. Wolynes. Semiclassical description of electron spin motion in radicals including the effect of electron hopping. *J. Chem. Phys.*, 68(7):3292, 1978.

[93] NJ Harmon and ME Flatté. Semiclassical theory of magnetoresistance in positionally disordered organic semiconductors. *Phys. Rev. B*, 85(7):075204, 2012.

[94] Arthur F Voter. *Introduction to the Kinetic Monte Carlo Method, NATO Science Series.* Springer, Dordrecht, 2007.

[95] Allen Miller and Elihu Abrahams. Impurity conduction at low concentrations. *Phys. Rev.*, 120(3):745–755, 1960.

[96] Karl Blum. *Density Matrix Theory and Applications*, volume 64. Springer Science & Business Media, 2012.

[97] Kenichi Goushi, Kou Yoshida, Keigo Sato, and Chihaya Adachi. Organic light-emitting diodes employing efficient reverse intersystem crossing for triplet-to-singlet state conversion. *Nat. Photonics*, 6(4):253–258, 2012.

[98] AG Redfield. The theory of relaxation processes. In *Advances in Magnetic and Optical Resonance*, volume 1, pages 1–32. Elsevier, 1965.

[99] A. Nitzan. *Chemical Dynamics in Condensed Phases: Relaxation, Transfer and Reactions in Condensed Molecular Systems.* Oxford Graduate Texts. OUP Oxford, 2006.

[100] H.P. Breuer and F. Petruccione. *The Theory of Open Quantum Systems.* OUP Oxford, 2007.

[101] D. E. Manolopoulos and P. J. Hore. An improved semiclassical theory of radical pair recombination reactions. *J. Chem. Phys.*, 139(12):124106, 2013.

[102] Alan M. Lewis, David E. Manolopoulos, and P. J. Hore. Asymmetric recombination and electron spin relaxation in the semiclassical theory of radical pair reactions. *J. Chem. Phys.*, 141(4):044111, 2014.

[103] Tianyou Zhang, Bei Chu, Wenlian Li, Zisheng Su, Qi Ming Peng, Bo Zhao, Yongshi Luo, Fangming Jin, Xingwu Yan, Yuan Gao, Hairuo Wu, Feng Zhang, Di Fan, and Junbo Wang. Efficient triplet application in exciplex delayed-fluorescence oleds using a reverse intersystem crossing mechanism based on a δe_{S-T} of around zero. *ACS Appl. Mater. Interfaces*, 6:11907–11914, 2014.

[104] Mariano Campoy-Quiles, Toby Ferenczi, Tiziano Agostinelli, Pablo G. Etchegoin, Youngkyoo Kim, Thomas D. Anthopoulos, Paul N. Stavrinou, Donal D. C. Bradley, and Jenny Nelson. Morphology evolution via self-organization and lateral and vertical diffusion in polymer:fullerene solar cell blends. *Nature Materials*, 7(2):158–164, 2008.

[105] Adam J. Moulé and Klaus Meerholz. Controlling morphology in polymer-fullerene mixtures. *Adv. Mater.*, 20(2):240–245, 2008.

[106] Timothy M. Burke, Sean Sweetnam, Koen Vandewal, and Michael D. McGehee. Beyond Langevin Recombination: How Equilibrium Between Free Carriers and Charge Transfer States Determines the Open-Circuit Voltage of Organic Solar Cells. *Adv. Energy Mater.*, 5(11):1500123, June 2015.

[107] S Barth, D Hertel, Y.-H. Tak, H. Bässler, and H.H. Hörhold. Geminate pair dissociation in random organic systems. *Chemical Physics Letters*, 274(1-3):165–170, aug 1997.

[108] Uwe Albrecht and Heinz Bässler. Yield of geminate pair dissociation in an energetically random hopping system. *Chemical Physics Letters*, 235(3-4):389–393, 1995.

[109] Ton Offermans, S. C J Meskers, and R. A J Janssen. Monte-Carlo simulations of geminate electron-hole pair dissociation in a molecular heterojunction: A two-step dissociation mechanism. *Chem. Phys.*, 308(1-2):125–133, 2005.

[110] J.A. Govatski, M.G.E. da Luz, and M. Koehler. Anomalous maximum and minimum for the dissociation of a geminate pair in energetically disordered media. *Chem. Phys. Lett.*, 620:123–128, jan 2015.

[111] Samantha N. Hood and Ivan Kassal. Entropy and Disorder Enable Charge Separation in Organic Solar Cells. *J. Phys. Chem. Lett.*, 7:4495–4500, oct 2016.

[112] X-Y Zhu, Q Yang, and M Muntwiler. Charge-transfer excitons at organic semiconductor surfaces and interfaces. *Acc. Chem. Res.*, 42(11):1779–1787, 2009.

[113] Nicholas R Monahan, Kristopher W Williams, Bharat Kumar, Colin Nuckolls, and X.-Y. Zhu. Direct Observation of Entropy-Driven Electron-Hole Pair Separation at an Organic Semiconductor Interface. *Phys. Rev. Lett.*, 114(24):247003, jun 2015.

[114] Matthias Muntwiler, Qingxin Yang, William A. Tisdale, and X. Y. Zhu. Coulomb barrier for charge separation at an organic semiconductor interface. *Phys. Rev. Lett.*, 101(19):1–4, 2008.

[115] L. Onsager. Initial recombination of ions. *Phys. Rev.*, 54(8):554–557, 1938.

[116] Sung Heum Park, Anshuman Roy, Serge Beaupr||[eacute]||, Shinuk Cho, Nelson Coates, Ji Sun Moon, Daniel Moses, Mario Leclerc, Kwanghee Lee, and Alan J. Heeger. Bulk heterojunction solar cells with internal quantum efficiency approaching 100%. *Nat. Photonics*, 3(5):297–302, 2009.

[117] O. Rubel, S. D. Baranovskii, W. Stolz, and F. Gebhard. Exact Solution for Hopping Dissociation of Geminate Electron-Hole Pairs in a Disordered Chain. *Phys. Rev. Lett.*, 100(19):196602, may 2008.

[118] Jiye Lee, Koen Vandewal, Shane R Yost, Matthias E Bahlke, Ludwig Goris, Marc A Baldo, Jean V Manca, and Troy Van Voorhis. Charge Transfer State Versus Hot Exciton Dissociation in PolymerâĹŠFullerene Blended Solar Cells. *J. Am. Chem. Soc.*, 132(34):11878–11880, sep 2010.

[119] Brian A Gregg. Entropy of Charge Separation in Organic Photovoltaic Cells: The Benefit of Higher Dimensionality. *J. Phys. Chem. Lett.*, 2(24):3013–3015, dec 2011.

[120] Harm van Eersel, René A J Janssen, and Martijn Kemerink. Mechanism for Efficient Photoinduced Charge Separation at Disordered Organic Heterointerfaces. *Adv. Funct. Mater.*, 22(13):2700–2708, jul 2012.

[121] Shane R Yost and Troy Van Voorhis. Electrostatic Effects at Organic Semiconductor Interfaces: A Mechanism for 'Cold' Exciton Breakup. *J. Phys. Chem. C*, 117(11):5617–5625, mar 2013.

[122] G Grancini, M Maiuri, D Fazzi, a Petrozza, H-J Egelhaaf, D Brida, G Cerullo, and G Lanzani. Hot exciton dissociation in polymer solar cells. *Nature Materials*, 12(1):29–33, 2013.

[123] Steffen Tscheuschner, Heinz Bässler, Katja Huber, and Anna Köhler. A Combined Theoretical and Experimental Study of Dissociation of Charge Transfer States at the Donor-Acceptor Interface of Organic Solar Cells. *J. Phys. Chem. B*, 119(32):10359–10371, aug 2015.

[124] Aleksey A. Kocherzhenko, Donghyun Lee, Michael Aziz Forsuelo, and Katharine Birgitta Whaley. Coherent and Incoherent Contributions to Charge Separation in Multi-Chromophore Systems. *J. Phys. Chem. C*, 119:7590–7603, 2015.

[125] Martin Stolterfoht, Ardalan Armin, Safa Shoaee, Ivan Kassal, Paul Burn, and Paul Meredith. Slower carriers limit charge generation in organic semiconductor light-harvesting systems. *Nat. Commun.s*, 7(May):11944, jun 2016.

[126] Gabriele D'Avino, Luca Muccioli, Yoann Olivier, and David Beljonne. Charge Separation and Recombination at PolymerâĂŞFullerene Heterojunctions: Delocalization and Hybridization Effects. *J. Phys. Chem. Lett.*, 7(3):536–540, feb 2016.

[127] Stavros Athanasopoulos, Steffen Tscheuschner, Heinz Bässler, and Anna Köhler. Efficient Charge Separation of Cold Charge-Transfer States in Organic Solar Cells Through Incoherent Hopping. *The Journal of Physical Chemistry Letters*, 8:2093–2098, 2017.

[128] Gleb M Akselrod, Ferry Prins, Lisa V Poulikakos, Elizabeth M Y Lee, Mark C Weidman, a Jolene Mork, Adam P Willard, Vladimir Bulović, and William a Tisdale. Subdiffusive Exciton Transport in Quantum Dot Solids. *Nano Letters*, 14(6):3556–3562, jun 2014.

[129] Chee Kong Lee, Liang Shi, and Adam P. Willard. A Model of Charge Transfer Excitons: Diffusion, Spin Dynamics, and Magnetic Field Effects. *J. Phys. Chem. Lett.*, 7:2246–2251, 2016.

[130] H. Bässler. Charge Transport in Disordered Organic Photoconductors a Monte Carlo Simulation Study. *Phys. Status Solidi B*, 175(1):15–56, jan 1993.

[131] Elizabeth M. Y. Lee, William A. Tisdale, and Adam P. Willard. Can Disorder Enhance Incoherent Exciton Diffusion? *J. Phys. Chem. B*, 119(30):9501–9509, jul 2015.

[132] Charles L Braun. Electric field assisted dissociation of charge transfer states as a mechanism of photocarrier production. *Journal of Chemical Physics*, 80(9):4157, 1984.

[133] Mariusz Wojcik and M. Tachiya. Accuracies of the empirical theories of the escape probability based on Eigen model and Braun model compared with the exact extension of Onsager theory. *The Journal of Chemical Physics*, 130(10):104107, mar 2009.

[134] Andreas P. Arndt, Marina Gerhard, Aina Quintilla, Ian A. Howard, Martin Koch, and Uli Lemmer. Time-Resolved Charge-Transfer State Emission in Organic Solar Cells: Temperature and Blend Composition Dependences of Interfacial Traps. *The Journal of Physical Chemistry C*, 119(24):13516–13523, jun 2015.

[135] L. H. Slooff, S. C. Veenstra, J. M. Kroon, D. J D Moet, J. Sweelssen, and M. M. Koetse. Determining the internal quantum efficiency of highly efficient polymer solar cells through optical modeling. *Appl. Phys. Lett.*, 90(14):143506, apr 2007.